**Development & Experimental Validation of Finite Element Simulation of Sound Transmission in Lungs & Torso**

By

YING PENG
B.S., Beijing Technology and Business University, 2006
M.S., University of Illinois at Chicago, Chicago, 2009

THESIS

Submitted as partial fulfillment of the requirements
for the degree of Doctor of Philosophy in Mechanical Engineering
in the Graduate College of the
University of Illinois at Chicago, 2015

Chicago, Illinois

Defense Committee:

Thomas J. Royston, Chair and Advisor
Dieter Klatt, Bioengineering
Hansen A. Mansy, University of Central Florida
Michael J. Scott, Mechanical & Industrial Engineering
Richard L. Magin, Bioengineering

# DEDICATION

To my parents Weilian Peng and Xingying Chen for their endless love, support and encouragement.


To my wife who has supported me with her unwavering love and patience throughout the process.


To my lovely daughter Xuanzhi Peng.

# ACKNOWLEDGEMENTS

**TABLE OF CONTENTS**

**CHAPTER**                                                                    **PAGE**

# CONTRIBUTION OF AUTHORS

Chapter 1 is an introduction of the background and motivation of my dissertation. In addition, current and previous studies and achievements related to my research are also discussed in following a literature review.

Chapter 2 represents a published manuscript [75] for which I was the primary author and major driver of the research. Dr. Zoujun Dai and Dr. Hansen Mansy helped me in the experiments shown Sec. 2.2.2. My advisor Dr. Thomas Royston, co-advisor Dr. Hansen Mansy, Dr. Richard Sandler, and Dr. Robert Balk contributed to the writing revision of the manuscript.

Chapter 3 combines the achievements from three manuscripts [16, 35, 75] for which I was the one of primary author.  Dr. Zoujun Dai and Dr. Hansen Mansy worked together with me in the experiments shown Sec. 3.3. I generated all of the figures except Figure 3.3 to 3.5 which were generated by Brian Henry and Dr. Zoujun Dai. For the contributions, my work was critical to the results and conclusions of this manuscript because I played a large role in deriving theory, creating simulations, and  writing of the manuscripts along with the anther primary author Zoujun Dai [16] and co-author Brian Henry [35]. My advisor Dr. Thomas Royston, co-advisor Dr. Hansen Mansy, Dr. Richard Sandler, and Dr. Robert Balk contributed to the writing revision of the manuscript.

Chapter 4 represents a series of my own unpublished results with another approach for my research. The results will be considered as one of the corner stones for the future study in the lab. In Chapter 5 represents my conclusion of the research presented in this dissertation. The future directions of this field and this research question are discussed.

## LIST OF TABLES

## LIST OF FIGURES

# LIST OF FIGURES (Continued)

**FIGURE**                                                                  **PAGE**

**FIGURE**                                                                                                    **PAGE**

**FIGURE**                                                                                    **PAGE**

**SUMMARY**

Measuring sound transmission in the torso and lungs may be of value if altered transmission patterns correlate with pathology in ways that can be detected and used to provide a reliable and quantitative diagnosis of disease or injury. The aims of this dissertation research are to develop accurate subject-specific computational models, including human and porcine subjects, for simulating sound propagation in the lungs and torso. Models are validated by comparing with experimental studies on the lungs and torso. The developed computational simulation models may be of use in assessing the performance of acoustic approaches in the diagnosis of injuries and diseases. This work is significant to the long-term goal of the "Audible Human Project (AHP)", which aims to develop a computational acoustic model that would accurately simulate generation, transmission and noninvasive measurement of sound and vibration throughout the body caused by both internal and external sources. The outcome of it may also be useful in the development of a more effective educational tool for teaching stethoscopic skills in the future. In order to achieve these goals, the specific aims to be undertaken are as follows:

1)     Develop and improve organ-detailing geometries of human and porcine subjects for vibroacoustic computational simulations.

2)     Improve lung airway computational models for sound transmission modeling.

3)     Develop and improve two external vibroacoustic excitation techniques that may be valuable for researching lung disease.

4)      Validate developed computational models with experimental studies.

5)      Develop computational models for lung pathological conditions.

In this dissertation, experimental studies will be undertaken by applying two external vibroacoustic stimuli to human and porcine models. Computational models representing human and porcine upper torsos and capable of representing healthy and specific pathological conditions will be developed. These models will be used to simulate wave transmission and measurement of acoustic pressure and motion caused by the externally driven source. Poroviscoelastic properties of the lung tissue calculated from Biot theory will be applied to the lung region in the simulation and the lung airway structure following the Horsefield model will be investigated and developed for the simulation. The results of the simulation will be compared with experimental measurements for validation. Pathologies of the pulmonary system, such as pneumothorax, fibrosis, localized mass, etc., will be studied and generated in the computational models. Finally, the developed and validated human computational models will play a significant role and be used for the long term goals of the AHP project, which ultimately will simulate the vibroacoustic environment of virtual patients with different pathologies.

The proposed research will develop experimentally validated computational models for simulations of the propagation of sound and vibration introduced from outside the body. These computer simulations using conventional numerical methods or augmented haptic virtual reality environments with sight, sound and tactile feedback could be a tool for advanced acoustic medical device design with decreased need for animal testing.

Furthermore, the developed model may aid in the interpretation of measurements obtained using elastography methods, such as magnetic resonance elastography (MRE), which has been recently applied to the lungs. This technique seeks to provide a map of the viscoelastic properties within the region of interest that will affect the shear wave motion that MRE measures. The developed simulation will provide a better understanding of mechanical wave motion in the lungs which would aid in the interpretation of the wave images that are acquired using elastographic techniques. From an educational perspective, recent studies have emphasized the continued importance of skilled auscultation in medicine and the fact that this skill is in decline among younger physicians. The AHP could help provide a more effective educational experience.

**CHAPTER 1**

(Previously published as Peng Y, Dai Z, Mansy HA, Sandler RH, Balk RA, and Royston TJ (2014) Sound transmission in the chest under surface excitation: an experimental and computational study with diagnostic applications. Med Biol Eng Comput 52:695–706.)

## 1. INTRODUCTION

### 1.1 Background and Motivation

Like no other anatomical region in the body, the lungs are a unique, multiphase porous structure that has defied conventional noninvasive medical imaging methods and our ability to contrast and quantify changes in its macroscopic properties that can be indicative of disease and which may be fundamentally linked to functional and structural changes at the microscopic scale. Patients suffering from a wide range of pulmonary ailments that result in significant changes, locally or diffusely, to the stiffness or density in the lungs, with symptoms that include inflammation, fibrosis, edema, consolidation or a mass (tumor), often are not easily diagnosed via noninvasive means due to the unique morphology of the lungs that renders them inaccessible to most conventional imaging modalities.

Conventional ultrasound imaging is generally limited to the periphery of the lung due to the acoustic impedance mismatch between the air in the lungs and soft tissue. X-ray computed tomography (CT) and magnetic resonance imaging (MRI), while continuing to improve in their ability to macroscopically image lung anatomy, have struggled to provide meaningful information and contrast changes associated with structure and function; CT also has the negative aspect of ionizing radiation. Spirometry, the

measurement of the volume of inhaled or exhaled air as a function of time, provides a global measure of lung and airway properties and is relatively insensitive to changes in small-airway structure and function. Moreover, it is suggested that Radio frequency (RF) tagging techniques of MRI can be used to access regional mechanical properties of the tissue [18, 66]; However,  this approach is limited duo to the changes in lung volume among the respiratory cycles.

Also recently, the phase contrast-based technique known as magnetic resonance elastography (MRE) has been applied to the lungs in pilot studies with some success [28, 60]. MRE seeks to provide a map of the viscoelastic properties within the region of interest that will affect the shear wave motion that MRE measures.  Previously, MRE has been successfully applied to the study of the mechanical properties of a variety of other organs and soft tissue regions in vivo, including the breast, brain, kidney, prostate, liver and muscle. Application to the lungs has proven more challenging, given the poor signal-to-noise available in imaging due to much lower presence of hydrogen in air than in soft tissue (water), and the complex nature of vibratory wave propagation found in the lungs. A better understanding of mechanical wave motion in the lungs would aid in the interpretation of the wave images that are acquired using MRE to reconstruct a quantitative map of variation in mechanical properties that correlate with injury, the progression of disease and/or the response to therapy. Moreover, the work is relevant to the goals of the AHP which aims to provide a complete vibroacoustic model of the human and how it is altered by disease and injury.

## 1.2    Literature Review on Related Topics

***Percussive sound transmission study:*** In clinical examinations, the conventional percussion method has been long known and is conducted by tapping different areas of the human body either with finger tips or a percussion hammer. By listening to the percussion sound, a skilled physician is sometimes able to qualitatively identify differences in the underlying body organs that arise from pathology. In 1980, Guarino [30] reported an improved technique in which the stethoscope was used for sound licensing. Although the sound was classified into three type "tympanic", "resonant" and "dull" [72, 107], these two methods are still highly limited by certain shortcomings, including limitations of the human ear and the subjectivity of the administrator, that lead to overall low sensitivity [11]. Mansy et al. [56, 58] showed that low-frequency vibro-acoustic property changes caused by pneumoperitoneum were detectable using broad-band acoustic excitation applied at the abdominal surface. However, there have been limited studies of applying percussive sound with wide frequency content on the chest and lung. These traditional techniques are able to detect lung pathologies [99] but are limited by the spatial and spectral content of the excitation, and by the interpretation of the measurements based solely on listening to them or studying a graphical display of their temporal or spectral content without the aid of a computational model to help interpret the measurements. The potential benefit of coupling an array measurement on the surface with an improved computational model of sound propagation within the torso was demonstrated fundamentally in [70].

***Poroviscoelasticity modeling of lung.*** An improved theoretical understanding of lung tissue poroviscoelasticity will enhance the advancement of studies on multiple physiological phenomena in the lung, including gas and blood exchange, respiration

and breath sound transmission. This will also improve current research on biomechanics, acoustics, mass and fluid transport of the lung. There have already been numerous studies on poroelastic and poroviscoelastic modeling of soft tissues and their implementation by the finite element method. Simon et al [87, 88] proposed multiphase poroelastic finite element models for soft tissue structures and extended the model including transport and swelling in the tissue. Suh et al [90] studied the biphasic poroviscoelastic behavior of hydrated biological soft tissue. Setton et al [84] studied the biphasic poroviscoelastic behavior of articular cartilage. Yang et al [104] developed a FE model of a poroelastic biological tissue, which incorporated the viscoelastic material behaviour, finite deformation and inertial effect. Biot theory [5], which predicts the existence of two types of compression waves in fluid saturated porous media, has been widely used in many geophysical applications. The lung can also be modeled an air saturated porous media. Siklosi et al [86] modeled the lung parenchyma as a porous solid with air-filled pores by Biot theory as a model for its acoustic properties. The Biot model yielded a frequency dependence of the speed of sound that was in qualitative agreement with the measurements. Currently, there have been limited studies on poroviscoelaticity modeling of lung acoustics.

***Geometry construction and models of lung airway:*** Finite element analysis (FEA) study usually requires actual geometries. For instance, FEA of pulmonary acoustics requires a lung geometry including the airway tree. The most direct way is to generate the airways manually using image processing software which is based on the CT or MRI images [13, 16, 93]. However, the segments of many tiny airways could not be viewed and generated by this approach due to the resolution of CT or MRI images. Horsfield et

al. [36, 38] proposed an approximate but comprehensive model for the geometries of the lung airways based on detailed lung castings for both human and canine subjects. The Horsfield model is self-consistent in the sense that, for a particular airway order, n, the bifurcated airway types (or daughter airways) are the same throughout the lung. Another approach is using a deterministic algorithm developed by Kitaoka [44] and others merged with our adaptation of a constrained constructive optimization (CCO) algorithm for growing realistic airways trees that extend from the trachea all the way down to the alveolar sacs. In order to get a subject specific lung airway trees, manually generating airways from the CT or MRI images is one method, but time consuming. A semi-automated lung airway segment method based on CT images has been reported by Hu et al. [39].

***Acoustic measurements of sound transmission through the pulmonary system and torso.*** Mechanical compression waves (sound) travel in the lung much more slowly than in the air and soft tissue of which it is comprised; sound speed in the human lung [4, 47, 54, 71] and animal lung  [40, 41, 77, 106] have been studied by several groups. In human studies, sound was usually introduced into the mouth; but, the sound speed range from each group has been very different. In animal studies, sound was usually applied to the lung surface. Sound speed ranges from all groups were consistent even though the measurements were taken on different animals. Also, all these animal studies concluded that the sound speed depended on the lung volume as the lung volume change (throughout the respiratory cycle) leads to the change of air volume fraction in the lung, thus affecting the sound speed. This is consistent with theoretical models. Studies have also been carried out to estimate the attenuation associated with

sound propagation through the parenchyma. Wodicka et al. [101] modeled the parenchymal mixture as air bubbles (alveoli) in water (lung tissue) at low audible frequencies and proposed that the magnitude of thermal losses are theoretically much larger than those associated with scattering or viscous effects. The predicted power spectra of acceleration and the experimental measurements at the tracheal and chest wall agreed somewhat. More sophisticated theoretical methods containing the small airways effects have also been used to predict the frequency dependence of the sound velocity and other properties in a wide frequency range [15]. In order to acquire the response of the thorax, some previous investigations focused on the transmission of sound introduced from the mouth then to measurements on the chest surface. For the circumstance, properties of the system which are in either static or even dynamic conditions are able to be measured and compared by the model predictions and other hypotheses. The amplitude and phase delay of transmission can be found by the FRF of the chest surface response and a reference. The reference can be measurement of the extrathoracic trachea or other measurable approaches. Amplitude of frequency-dependent matches the substance of the accounting parenchymal losses of the thorax model [96, 101]. Kraman et al. [47, 49] proposed an approach for measuring sound transmission from the mouth to the chest wall and the approach was also studied by Wodicka et al [103] and Pasterkamp et al. [74]. The reports from their study indicated that the amplitude at the right lung site was significantly greater than the one at the left lung site in the low frequency range. In addition, the findings also suggested that the changes in lung structure caused by disease were able to affect the amplitude and speed of the sound transmitted from the airways then propagated to the chest surface.

Böhme et al [9] reported that a decrease of transmitted amplitude at low frequencies In patients with emphysema and Mansy et al. confirmed the similar finding in dogs with pneumothorax [57] later in the study. Differently, it was reported [20] that cardiogenic pulmonary edema could cause  increasing amplitude of sound transmitted to the chest wall in dog and the consolidated lung.

***Three dimensional modeling and computational simulation.*** In the last two decades, computer aided engineering (CAE) has been applied to a number of research fields.  For example, computational modeling and simulation for realistic human and animal subjects significantly helps researchers with more capabilities to explore many different pathological conditions and their response to treatment for the biomedical investigation. Especially, in the early 1990s, the "Visible Human Project (VHP)" [109] which has been made available through the U.S. National Library of Medicine, created a digital database of cross-sectional images of the human body acquired via multiple modalities.  This project gave researchers capabilities of utilized the database to create virtual reality (VR) for medical surgeries, such as the hepatic surgery [59], arthroscopic surgery [34] and virtual surgical training for liver, brain and heart [19].  Further, more and more computational simulations are being applied in other research directions, such as mechanics [67, 68],  chemistry [23], electromagnetics [83], pathology [16, 73]  and so on.

## 1.3    Dissertation Research Objectives

The aims of this dissertation research are to develop accurate subject-specific computational models, including human and porcine subjects, for simulating sound propagation in the pulmonary system and torso.  Models are validated by comparing

with experimental studies on the lungs and torso of porcine and human subjects. The developed computational simulation models may be of use in assessing the performance of acoustic approaches in the diagnosis of injuries and diseases. This work is significant to the long-term goal of the "Audible Human Project (AHP)", which aims to develop a comprehensive computational acoustic model that would accurately simulate generation, transmission and noninvasive measurement of sound and vibration throughout the body caused by both internal and external sources. The outcome of AHP may also be useful in the development of a more effective educational tool for teaching stethoscopic skills in the future. In order to achieve these goals, the specific aims to be undertaken are as follows:

1) Develop and improve organ-detailing geometries of human and porcine subjects for vibroacoustic computational simulations.

2) Improve lung airway computational models for sound transmission modeling.

3) Develop and improve two external vibroacoustic excitation techniques that may be valuable for researching lung disease.

4) Validate developed computational models with experimental studies.

5) Develop computational models for lung pathological conditions.

With the proposed research and its results, the AHP will be able to achieve experimentally-validated computational models for sound propagation in the subglottal airways and lungs that can be used to predict acoustic impedance of the airways and that can be integrated within a computational model of the torso to predict sound transmission throughout the torso and its measurement at the skin surface. Moreover, the computational models will be also useful to predict the effects of the interior and

exterior acoustic properties changes which are affected by the specific pathologies, such as pneumothorax (PTX), fibrosis, cancer and so on.

## 1.4    Dissertation Outline

**Chapter 1** - The background, motivation and research objectives of this dissertation are presented.

**Chapter 2** - An improved auscultatory percussion technique is proposed. The experimental results of animals and humans are used to validate a computational model of sound transmission and the validated model is then used to predict effects caused by one pathological condition.

**Chapter 3** - A comprehensive computation model of sound transmission through a porcine lung is validated by proposed experiments. The effect of diffuse lung fibrosis and a local tumor on the lung acoustic response is predicted by their simulations by using the computational models.

**Chapter 4** - A three dimensional computation model with sophisticated airway geometry of porcine and human is developed to simulate the sound transmission in lungs and torso. The corresponding experiment is proposed and results are used to validate the computational models.

**Chapter 5** - The accomplishments of this dissertation and topics for future research are summarized and discussed.

**CHAPTER 2**

## 2. SOUND TRANSMISSION IN THE CHEST UNDER SURFACE EXCITATION

(Previously published as (1) Peng Y, Dai Z, Mansy HA, Sandler RH, Balk RA, and Royston TJ (2014) Sound transmission in the chest under surface excitation: an experimental and computational study with diagnostic applications. Med Biol Eng Comput 52:695–706. (2) Dai Z, Peng Y, Henry B, Mansy HA, Sandler RH, Royston TJ (2014) A Comprehensive Computational Model of Sound Transmission through the Porcine Lung. J. Acoust. Soc. Am.)

### 2.1    Introduction

### 2.1.1   Clinical use of percussion

Percussion is a common component of the clinical chest physical examination, where the objective is often to determine if the area under consideration is air-, fluid- or solid-filled [97].  Such determination can aid in diagnosing pulmonary conditions including pneumothorax, pleural effusion, consolidation and lung masses.  During percussion, acoustic energy is introduced at the skin surface and the resulting sound changes are detected.  In "conventional percussion" (CP) this is typically accomplished by the clinician placing the middle finger of the non-dominant hand against the chest wall in the area of interest, followed by a rapid wrist flexion of the dominant wrist.  The rotational energy of this movement is directed through the middle finger of the moving hand against the outstretched middle finger of the stationary hand while listening for a change in the acoustic chest wall response [65].  An alternative method is auscultatory percussion (AP), which is implemented by tapping on the chest while listening to the posterior chest with a stethoscope [29, 30].  In either case, the clinician listens to the

produced sounds, subjectively noting amplitude and pitch (frequency) changes [97]. For example, tympanic "bright" sounds are indicative of air, or "dull" percussive sounds are suggestive of fluid filled or consolidated structures.

Manual implementation of percussion is qualitative, subjective, and skill dependent. This limits the reliability of the method, which may explain the varied levels of clinical utility reported in the literature. For example, a controlled blind study [33] found that AP had 86% sensitivity and 84% specificity and CP had 76% sensitivity and 100% specificity. On the other hand, another study [11] investigated the sensitivity of detecting abnormality in the chest between CP and AP and concluded that the sensitivities of both CP and AP are too low to present acceptable positive predictive values for clinical examinations. The validation of these two techniques was questioned by Bohadana *et al.* [7] and found that the lung characteristics do not cause significant changes to the transmitted sounds when the AP technique was applied at the sternum. They also suggested that the sound generated by percussion at the sternum propagated to the posterior chest mainly through the chest cage structures [8].

### 2.1.2 Other methods of pulmonary diagnosis

Diagnostic methods used to evaluate pulmonary conditions include several imaging modalities such as X-ray, computed tomography (CT), and magnetic resonance imaging (MRI). Imaging methods have continued to improve in their ability to macroscopically image lung anatomy and aid in indirectly assessing lung functional changes. CT and X-ray, however, have the undesirable aspect of ionizing radiation. Ultrasound has limited utility in imaging lung structures due to the acoustic impedance mismatch between the chest wall and air within the lungs. This causes strong reflection of sound waves at the

lung interface making it practically infeasible to image areas inside the lungs. Diagnostic methods also include spirometry (the measurement of the volume of inhaled or exhaled air as a function of time), which provides a global measure of lung and airway properties but is patient effort dependent and relatively insensitive to changes in small-airway structure and function. Sputum monitoring and respiratory tests before and after the administration of bronchodilators to assess changes in airway plasticity impose similar constraints by providing global and, at best, indirect information on spatial extent of lung conditions. In addition, MRI using Radio frequency (RF) tagging techniques has been suggested as a method for assessing the regional mechanical properties of the parenchyma [17, 66]; but, this approach is limited to assessing changes in lung volume throughout the respiratory cycle. Finally other pulmonary diagnostic modalities include video bronchoscopy, interventional radiological biopsy, and video assisted or open thoracotomy.

### 2.1.3  Use of MR elastography

Recently, the phase contrast-based technique known as magnetic resonance elastography (MRE) has been applied to the lungs in pilot studies with some success [28, 60]. MRE seeks to provide a map of the viscoelastic properties within the region of interest (ROI) [105]. These maps may correlate with injury, the progression of disease, and/or the response to therapy. To obtain the MRE images, shear waves are introduced into to ROI by, for example, a transversely vibrating driver with frequencies in the range of 50 to 200 Hz [60]. Wave motion is then measured and a map of the viscoelastic properties is constructed. Goss *et al.* applied a longitudinal vibration to the chest wall and hypothesized that the generated compression wave would pass through

the chest wall into the lung and the shear wave would be excited due to mode conversion [28]. Since 1995, MRE has been successfully applied in vivo to study of the mechanical properties of a variety of organs including the breast [76], brain [50], kidney [98], prostate [43], liver [95] and muscle [55]. Application to the lungs has proven more challenging because of the poor signal-to-noise available in imaging due to a much lower presence of hydrogen in air than in soft tissue (water), and the complex nature of vibratory wave propagation found in the lungs. Better understanding of mechanical wave motion in the lungs using computational models may aid in the interpretation of the wave images that are acquired using MRE.

### 2.1.4 Existing Challenges and Objectives of the Present Study

The main objective of this study is to develop and validate a computational model of sound transmission that can be used to predict chest response to surface excitations (e.g., percussive sounds). The model is validated using experimental measurements in animals and humans. This computer simulation is then used to predict changes in acoustic transmission caused by pneumothorax (PTX) which is an abnormal collection of air or gas in the pleural space separating the lung from the chest wall [56, 57].

Computational models may be also used in future studies to improve our ability to localize sound sources in the chest when acoustic surface measurements are available [1, 70, 78]. There are potential benefits of coupling a multi-point array measurement with an improved computational model of sound propagation to locate acoustic sources in the torso. For example, it was reported that this coupling was significantly superior in identifying the sound source location compared to a simple "ray acoustics" description

of sound transmission that neglects the more complex nature of sound transmission in a finite and complex dimensioned structure [76].

In previous studies, most of the acoustic energy of typical chest percussion was limited to frequencies below 200Hz with peak frequencies below 100 Hz [8]. In the present study the frequency range is widened to cover 50-400 Hz in order to further assess the utility of surface excitation in an expanded frequency range. To cover this broader range, a special vibratory excitation was implemented. Sec. 2.2 describes the computational and experimental methods, while Sec. 2.3 summarizes the results. Discussion of the results is provided in Sec. 2.4, followed by the Conclusions in Sec. 2.5.

## 2.2    Materials and Methods

### 2.2.1  Numerical simulations: Porcine normal, human normal and collapsed lung cases

To develop a realistic computational model, the three dimensional (3D) geometrical details of the porcine and human torso structures are needed. Dimensions of representative porcine chest structures were determined from computed tomography (CT) of a pig with similar size to those studied in the acoustic experiments. CT scans used 1 mm slice steps and pixel matrix size 512x512 (Brilliance 64, Philips Electronics). To build the 3D geometry of the human subject chest structures, the CT image sets available on line from the Visible Human Male (VHM) [109] were used. The dimensions of the human torso model were rescaled to match the size of the human subjects who participated in the study. To generate the 3D geometries for the computer model of

both human and porcine studies, the CT image sets were imported and processed using Mimics V14 (Materialise, Plymouth, MI), which is an image processing software for 3D design and modeling.

The experimental process of vibrating the sternum of all subjects was modeled in a finite element (FE) environment COMSOL® 4.3 (Comsol Inc, Burlington, MA) using the harmonic analysis acoustic-solid interaction module for frequency domain analysis. To run the FE analysis, the material properties of each organ need to be supplied to the model. Properties of the lung parenchyma have been discussed in the literature. For example, one recent study [17] showed that Biot theory of wave propagation in poroviscoelastic media and the effective medium theory has been used to model sound transmission in the lung parenchyma. Furthermore, measurements of compression wave speed and attenuation in freshly excised pig lung matched theoretical predictions based on Biot theory much more closely than the effective medium theory. The shear wave propagation in the lung is also well predicted by the Biot theory. The following set of coupled differential equations (written in the frequency domain neglecting initial conditions, and denoting a derivative with respect to time as multiplication by jω) [17] can be used to describe the steady-state dynamic oscillatory displacement $u$ of the lung parenchyma and dynamic pressure $p$ of the air in the lung:

$$\mu u_{i,jj} + \left(K_b + \frac{\mu}{3}\right)u_{j,ij} - (\alpha - \beta)p_{,i} + F_i = -\omega^2\left(\rho - \beta\rho_f\right)u_i$$

(2.1a)

$$\beta p_{,ii} + \frac{\phi^2}{R}\rho_f\omega^2 p + \rho_f j\omega a = -\rho_f\omega^2(\alpha - \beta)u_{i,i}$$

(2.1b)

Here, $\mu$ is the shear modulus of the lung tissue, $K_b$ is the bulk modulus of the lung tissue when it is inflated. $\rho$ is the lung density, $\rho_f$ is the air density, $\phi$ is the air volume fraction in the lung, $\alpha$ , $\beta$ and $R$ are the coupling parameters between the lung parenchyma and the air. Suppose that the dilatation $u_{i,i}$ is zero and neglecting external excitations, Eq. (2.1a) reduces to the following equation, which governs shear wave behavior:

$$\mu u_{i,jj} = -(\rho - \beta\rho_f)\omega^2 u_i$$

(2.1c)

From Eq. (1c) we can see that the complex-valued wave speed $c_s$ and shear wave number $k_s$ are

$$c_s = \sqrt{\mu/(\rho - \beta\rho_f)} \cong \sqrt{\mu/\rho}$$

(2.2a)

$$k_s = c_s / \omega$$

(2.2b)

The coupled Eqs. (2.1a-b) lead to two compression waves, a fast wave and a slow wave with much larger attenuation. The compression wave speeds are given by

$$c_{pf} = \omega / k_{pf}$$

(2.3a)

$$c_{ps} = \omega / k_{ps}$$

(2.3b)

Here, $c_{pf}$ and $c_{ps}$ are the fast and slow compression wave speeds, respectively. The corresponding complex-valued wave numbers, $k_{pf}$ and $k_{ps}$, are derived from Eqs. (2.1a-b). In our frequency range of interest (50-400 Hz), the slow compression wave can't

propagate effectively as the relative motion between the lung parenchyma and air is impeded by viscous drag [10]. Hence, only the fast compression wave propagation may be detectable in the parenchyma. As the lung parenchyma is viscoelastic, the shear wave speed is frequency-dependent. The phase speed and attenuation are expressed within the complex valued shear wave speed. The compression wave attenuation is mainly due to the friction between the air and the lung parenchyma. The complex-valued fast compression wave speed is given by Eq. (2.3a). By implementing the above equations, the frequency dependent compression wave speed and attenuation of compression wave and shear wave in lung parenchyma can be calculated and were completely defined for simulation in COMSOL.

Previous studies [77, 101] suggested that the lung air volume fraction $\phi$ = 75%, the lung tissue density $\rho_p = 1000$ kg/m$^3$, and the air density in the lung $\rho_g = 1.21$ kg/m$^3$. The lung density is given by:

$$\rho = \phi \rho_p + (1-\phi)\rho_t \tag{2.4}$$

These properties result in a density of the normal lung $\rho = 250.9$ kg/m$^3$. When the PTX condition is present in the right chest, the right lung parenchyma was collapsed and thus, had a lower air volume fraction depending on the level of collapse. In this case, the original right lung region in the 3D model was split into two parts, the collapsed parenchymal region and the air region outside the lung. Two different levels of collapse were considered in the current study, which correspond to $\phi = 28\%$ and $\phi = 58\%$. Those two values, respectively, correspond to PTX of 89% and 53% by volume, approximately.

The lung compression wave speed and attenuation were then calculated using equation 2.3 for $\phi = 75\%$, $\phi = 58\%$, and $\phi = 28\%$.

The values of material properties of other parts in the upper torso such as soft tissue, ribcage, sternum, and scapula were based on previous studies [26, 79, 80]. The osseous structure and other biological soft tissue were considered as viscoelastic media and the Voigt model of viscoelasticity was used for these regions. So, the bulk modulus is related to the two complex Lame constants as

$$B_{b/t} = \lambda_{b/t} + \frac{2}{3}\mu_{b/t}$$
(2.5)

Here, $\lambda_{b/t} = \lambda_{b/t1} + j\omega\lambda_{b/t2}$ and $\mu_{b/t} = \mu_{b/t1} + j\omega\mu_{b/t2}$ [26, 79]. The subscript "b" denotes the osseous materials like the ribcage, scapulae and sternum and "t" denotes the soft tissue. Also, $\lambda_{b/t1}$, $\lambda_{b/t2}$, $\mu_{b/t1}$, and $\mu_{b/t2}$ denote volume elasticity, volume viscosity, shear elasticity and shear viscosity, respectively for osseous materials and tissue. In the COMSOL simulation, the lung region was set as a "pressure acoustics model". The soft tissue and the osseous region were respectively set as the "linear viscoelastic material model" with different material properties assigned as follows: $\mu_{b1} = 10$ GPa, $\mu_{b2} = 20$ Pa-s, $\lambda_{b1} = 2.6$ GPa, $\lambda_{b2} = 0$ and density $\rho_b = 1500$ kg/m$^3$ for the bone and $\mu_{t1} = 2.5$ kPa $\mu_{t2} = 5$ Pa-s, $\lambda_{t1} = 2.6$ GPa, $\lambda_{t2} = 0$ and the density $\rho_t = 1000$ kg/m$^3$ for the soft tissue such as fat, muscle and connective tissue. Bone and soft tissue volume viscosity $\lambda_{b2}$ and $\lambda_{t2}$ are taken to be zero in our frequency range of interest (50-400 Hz) [26]. Harmonic vibratory excitation with displacement amplitude of 1 mm was applied to the sternum. The outside surface of the torso was set as a free boundary condition. The outside surfaces

of the lungs were set as an "acoustic-structure boundary" in COMSOL. The number of elements for the porcine simulation was 313,742 and 313,548 for normal case and the PTX case, respectively. The number of elements for the human simulation was 395,788 for the normal case, 392,796 for the PTX = 53% and 392,548 for the PTX = 89%. Element size was set to be smaller than 1/6 of wave length for the acoustic simulation for all regions and frequencies considered (Fig. 2.1).
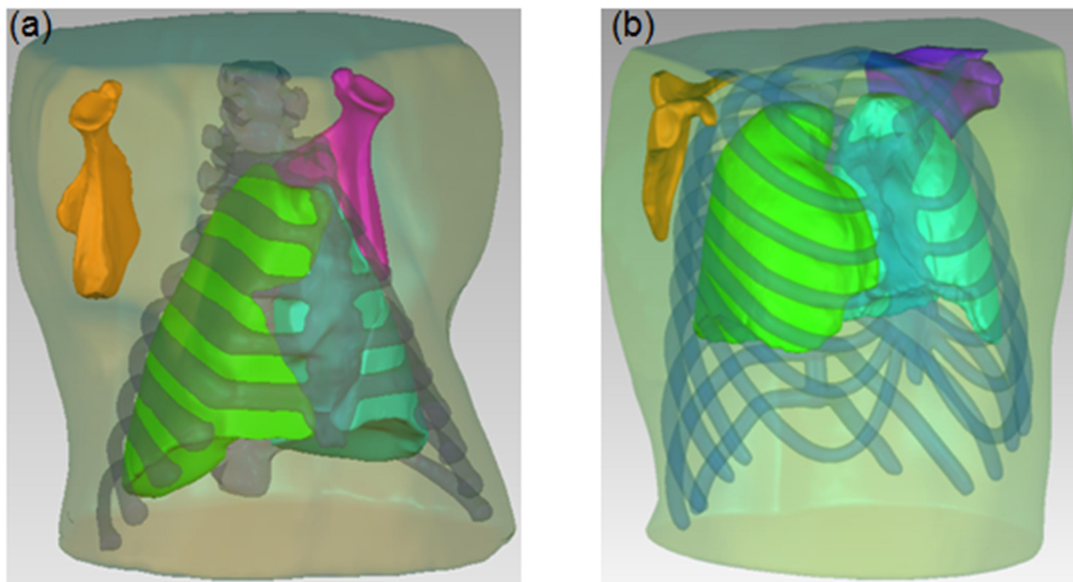


Figure 2.1 a) 3-D model of porcine upper torso and internal organs, (b) 3-D model of human upper torso and internal organs.

## 2.2.2 Experiment: Porcine studies – Normal and PTX cases



(a)



(b)
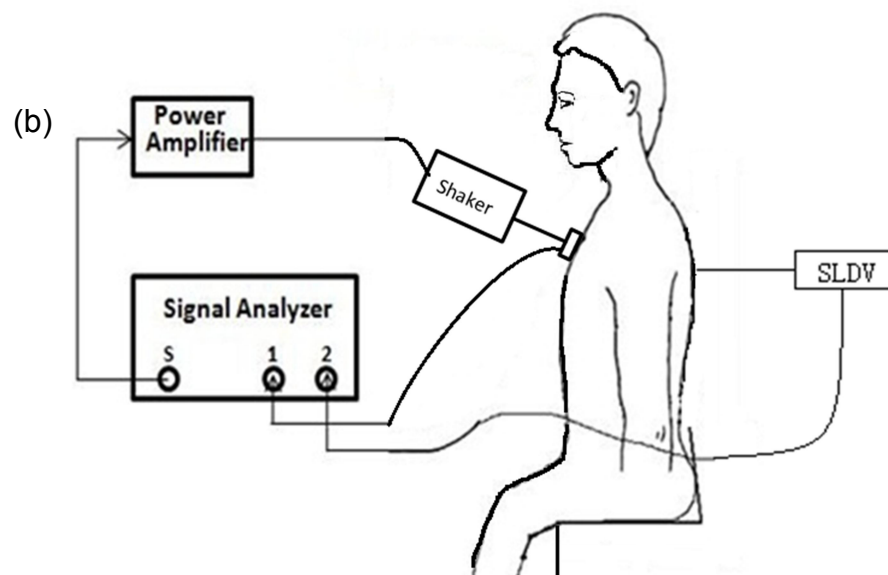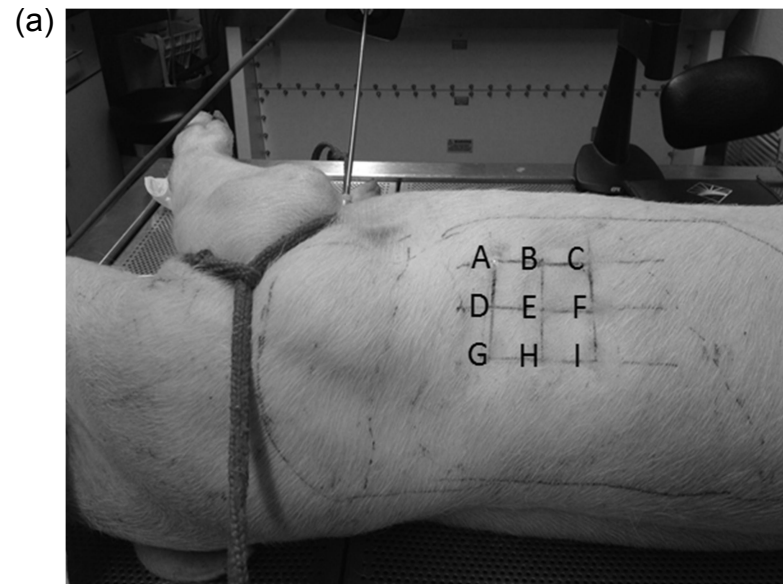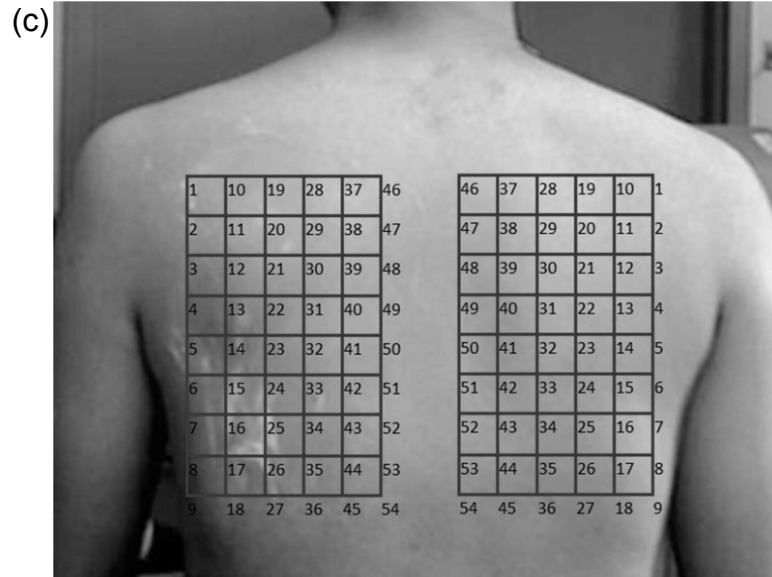
Figure 2.2 Experimental setup for human and porcine measurements. (a) Experimental setup for the porcine. (b) Schematic diagram of the experimental setup. (c) SLDV scanning points of human posterior.

Experiments were carried out on six freshly sacrificed female Landrace and Yorkshire cross pig subjects (weight 30 to 35 kg) after institutional animal care and use committee (IACUC) approval. The experimental setup is shown in Fig. 2.2(a). Immediately upon sacrifice the lung was kept inflated with air at continuous positive pressure of 5 cm $H_2O$ through an endotracheal tube. The pig was then secured in the left lateral decubitus position (right-side-up) with the skin hair of the measurement area shaved completely. P-RETRO-250 glass beads (45 – 63 µm dia., Polytec, Irvine, CA) were applied to the skin surface of subjects to enhance the laser reflectivity to enable an improved signal-to-noise ratio. The anatomy of the pig indicated that its lungs are located roughly between the first and tenth rib. The skin surface velocity was measured by a laser Doppler vibrometer (LDV) (PDV-100, Polytec, Irvine, CA) at 9 evenly spaced points in an array located in the area from the fifth rib to the ninth rib (Fig. 2.2(a)). A plexiglass

disk of radius 15 mm was gently pressed against the chest surface on the top of the sternum and driven by an electromagnetic shaker (ET-132, Lab-Works Inc., Mesa Costa, CA) that was connected to a power amplifier (P 3500S, Yamaha, Buena Park, CA).  An impedance head (288D01, PCB Piezotronics, Depew, NY) was mounted on the disk to measure the input acceleration, serving as a reference signal for the LDV measurements.  A periodic chirp with spectral content from 50 – 400 Hz was generated from a dynamic signal analyzer (SignalCalc ACE, Data Physics, San Jose, CA) and fed to the amplifier which drives the shaker.  The signal analyzer was also used to acquire and analyze the stimulus and output signals, which are the impedance head acceleration at the anterior chest and the LDV surface velocity at the posterior chest, respectively.

The signals are analyzed and results are presented in terms of the "frequency response function" (FRF).   Here, the FRF is defined as the frequency-dependent ratio between output acceleration, $ACC_P$ , (posterior chest) over the stimulus (i.e., reference) acceleration, $ACC_A$, (anterior chest).   This acceleration ratio is then converted to the decibel scale and is given by [69]:

$$FRF = 20 log_{10} \left( \frac{ACC_P}{ACC_A} \right) \tag{2.6}$$

The above measurements and analysis were performed for the normal (i.e., intact chest), and PTX states in each animal.  PTX was created by making a small incision in the seventh intercostal space in the right mid-axillary line then introducing air through the incision using a syringe.  The air pressure for inflating the lungs was set to "0" in the PTX state to allow for full lung collapse.  A 5 mm thoracoscopic trocar (Endopath

Dilating Tip, model 355, Ethicon, Cincinnati, OH) was inserted into the pleural space and a scope was used to visually confirm the PTX state.

### 2.2.3 Experiment: Human Studies – Normal Subjects

Experimental studies were carried out on three healthy human male subjects with ages of 25, 26 and 28, weight of 65, 68, and 67 Kg, and height of 175, 178, and 177 cm, respectively, after receiving appropriate Institutional Review Board (IRB) approval and informed consent. The subject was seated on a chair during the experiment.  As shown in Fig. 2.2(b), a plexiglass disk, the same as the one used for porcine experiment, was gently applied to the chest surface on the top of the sternum and driven by an electromagnetic shaker connected to a power amplifier.  The same chirp signal used in the animal experiments was generated from a scanning laser Doppler vibrometer (SLDV) (PSV-400, Polytec, Irvine, CA) and was fed into the power amplifier that was connected to the electromagnetic shaker.  Similar to the animal experiments, the impedance head was mounted on the disk to measure its acceleration, serving as a reference for the SLDV measurement.  The amplifier, shaker, and the impedance head were the same as the ones used in the porcine experiment.  The reflective glass beads were applied to the skin surface of subjects.  The SLDV was used to measure the skin surface velocity at an array of points on the posterior chest of the subject.  The measurements were acquired during a coached voluntary breath-hold period at the inspiration end.  There were 54 scan points on each side of the back (total of 108 scan points).  The experimental setup is shown in Fig. 2.2(c).

## 2.3    Results

First, the results of porcine experimental measurements described in Sec. 2.2 on normal and PTX cases are compared to the simulations described in Sec. 2.1 to validate the FE computer simulation model created in COMSOL.  Second, the results of experimental measurements described in Sec. 2.3 of normal human subjects are compared with numerical FE simulations described in Sec. 2.1 to further validate the model for human subjects.  Finally, results of numerical simulations of the human normal and PTX case are compared to provide predictions for the effects of PTX in humans.

### 2.3.1  Results of Porcine Studies.

The FRF from numerical simulations and from experimental measurements in six animals are plotted in Fig. 2.3(a) for the normal state at point B (see Fig. 2.2(a) for point location).   The labels for different surface points are shown in Fig. 2.2(a).   Both experimental and simulation plots are in the same decibel range.   The experimental FRF data of the porcine studies are only plotted at frequencies for which the coherence exceeded 0.85.  The data showed similar trends, but with inter-subject variability.  Fig. 2.3 (b) shows the mean FRF of all six pigs with the standard deviation indicated. In this figure, the simulation predication is compared to the mean FRF from all 6 pigs. Similar trends can be seen although the peaks (and valleys) in the experimental results have been minimized due to averaging. Figs. 2.3(c) and 3(d) show the simulation and experimental results of pigs #1 and #2, respectively, for normal and PTX states at a representative point B. It can be seen that the FRF amplitudes for the PTX state are lower than those for the normal state from 200 to 400 Hz for both simulation and

experimental results. Specifically, in the experiment there is an average reduction of 9.15 dB and 9.64 dB over this frequency range for pigs #1 and #2, respectively. The average reduction for all six pigs is 7.97 dB with a standard deviation of 2.60 dB. The simulation predicts a 7.48 dB reduction.
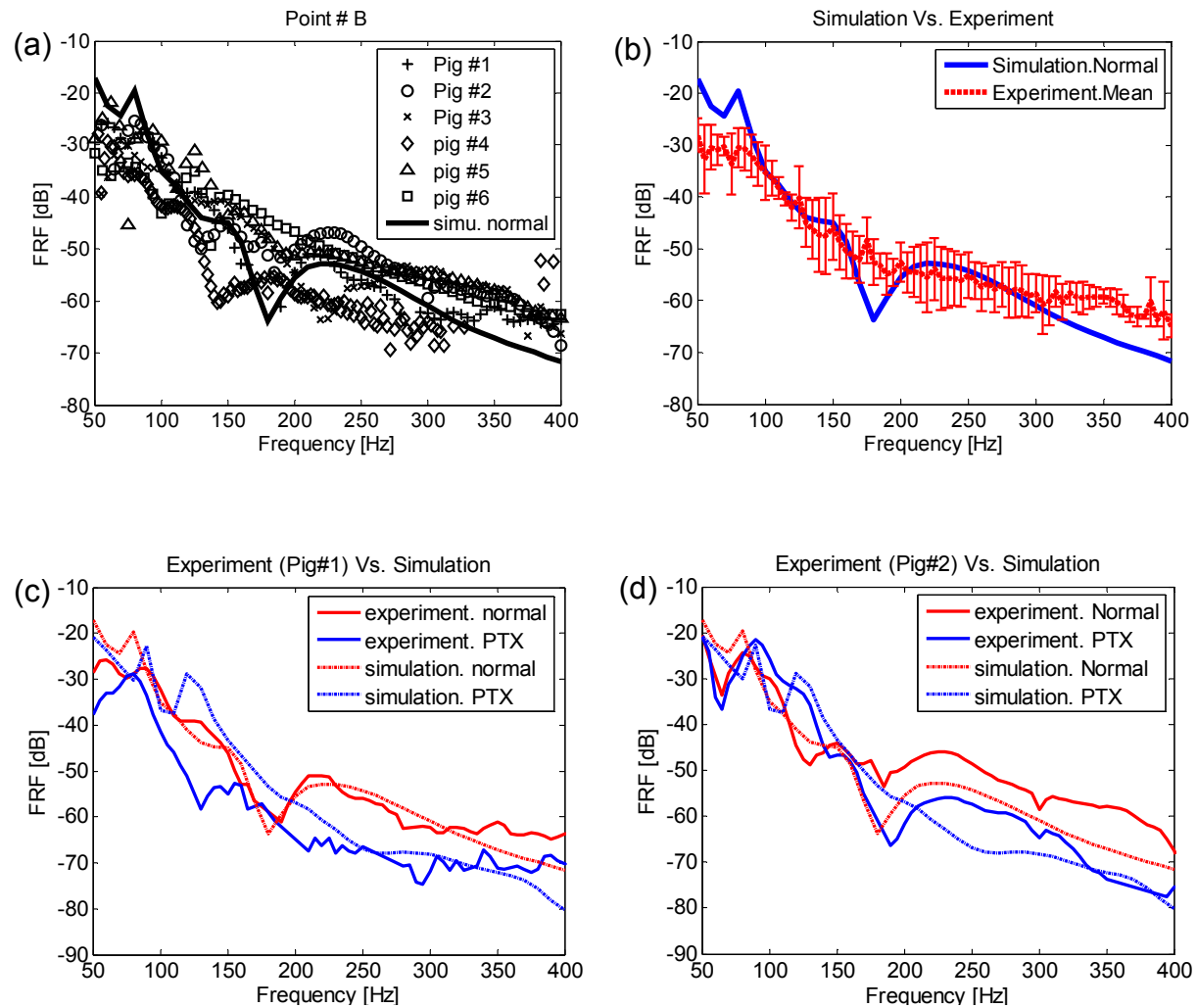


Figure 2.3 Porcine studies (a) Comparison of simulation and experimental results for normal state (b) Comparison of mean FRF of experiment and simulation for normal state. The error bars indicate standard deviation of six pigs. (c) Comparison of pig#1 experimental and simulation results for normal and PTX cases. (d) Comparison of pig#2 experimental and simulation results for normal and PTX cases.

### 2.3.2 Results of Human Studies.

In order to compare the results of simulation and experiment for the normal state in humans, FRF maps of the simulation and experiment were generated for the three healthy human subjects. Since the spatial resolution (distance between measurement points) was larger in the experiment, interpolation was used to more closely match the simulation spatial resolution (distance between the finite elements). Fig. 4 shows the FRF results at 60 Hz (Fig. 4(a)-(d)) and at 120 Hz (Fig. 4(e)-(f)), respectively. The simulation results are displayed in Fig. 4(a) and (e) for comparison. The color bar is in the decibel scale and is identical for simulation and experimental results. It can be seen that the FRF amplitudes tend to be larger in the lung region compared to the map boundaries. It also showed more attenuated amplitude over the scapulae, which is more appreciable at the top corners of several maps (e.g., Fig. 4(a-h)). In addition, inter-subject variability and some deviations between the patterns of simulation and experiment can be noticed. However, it is noticeable that the amplitudes of the experiment and simulation are comparable.

(g)  (h)
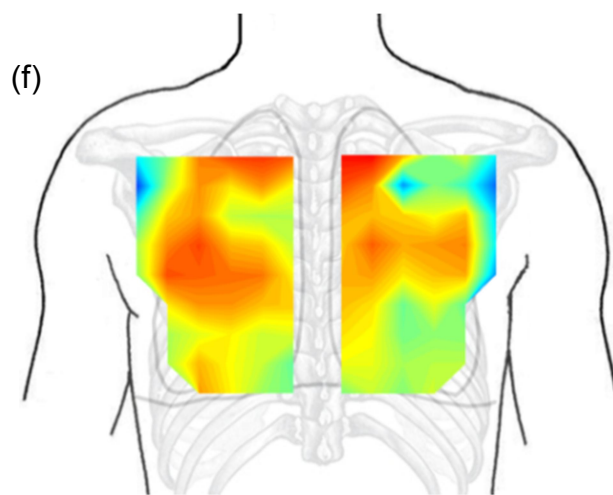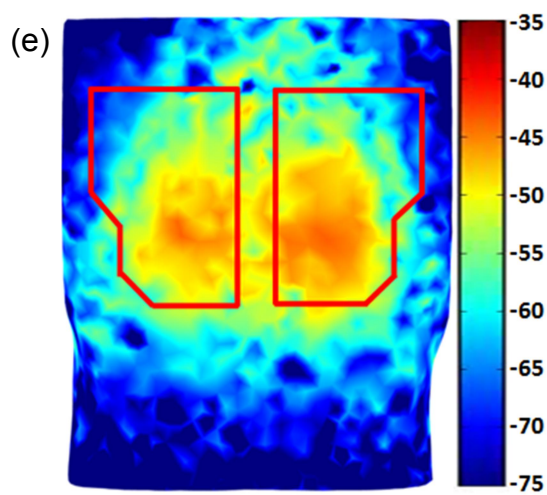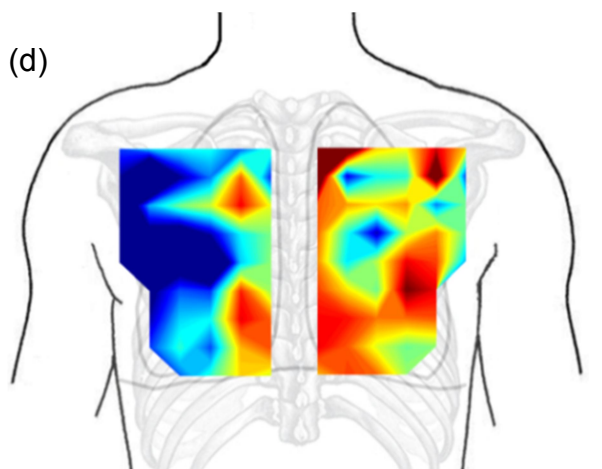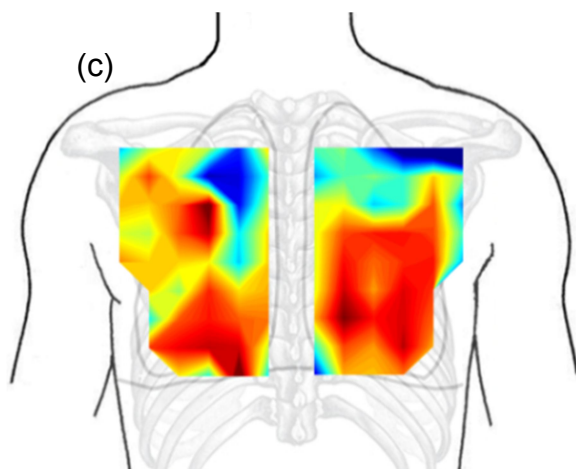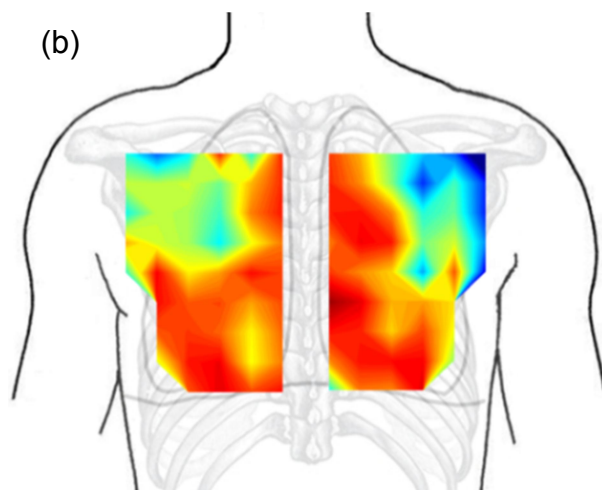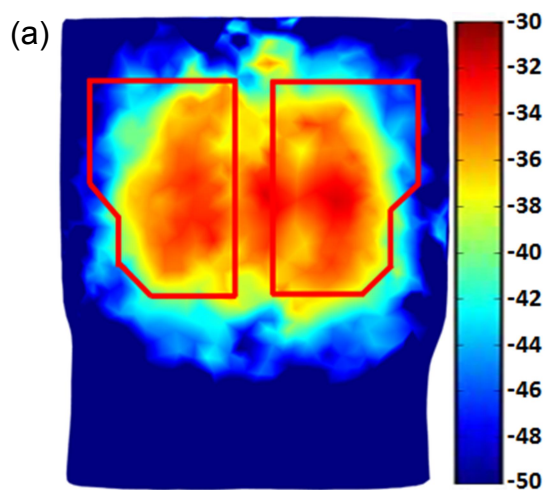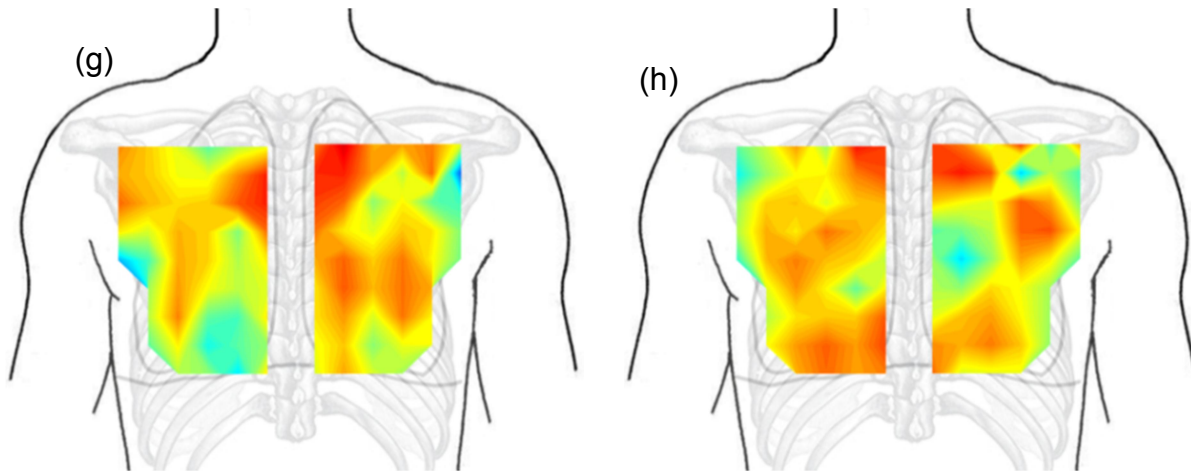


Figure 2.4 FRF images comparison of healthy human simulation and experimental results at 60 and 120 Hz. (a). Simulation at 60Hz. (b) Experiment: HS#1 at 60Hz. (c). Experiment: HS#2 at 60Hz. (d). Experiment: HS#3 at 60Hz. (e) Simulation at 120Hz. (f) Experiments: HS#1 at 120Hz. (g) Experiment: HS#2 at 120Hz. (h) Experiment: HS#3 at 120Hz. Color bar in dB scale.

In Fig. 2.5, numerical simulation and experimental measurement of the FRF are compared at three specific scanning points, which are points #15, #24 and #41 (point locations are shown in Fig. 2.2(c)). These three points on both sides of the back areas were taken in the location avoiding the scapulae, in order to have higher measurement signal-to-noise ratio (SNR). The experimental data are only plotted at frequencies where the coherence exceeded 0.85. Coherence was not good at high frequencies due to low SNR, and hence only the range of 50 – 200 Hz is shown. By comparing the simulation and experimental results of Fig. 2.5, similar amplitudes and trends can be seen, which further contributes to the validity of the model.

(a)

Point #15

Point #24

(b)
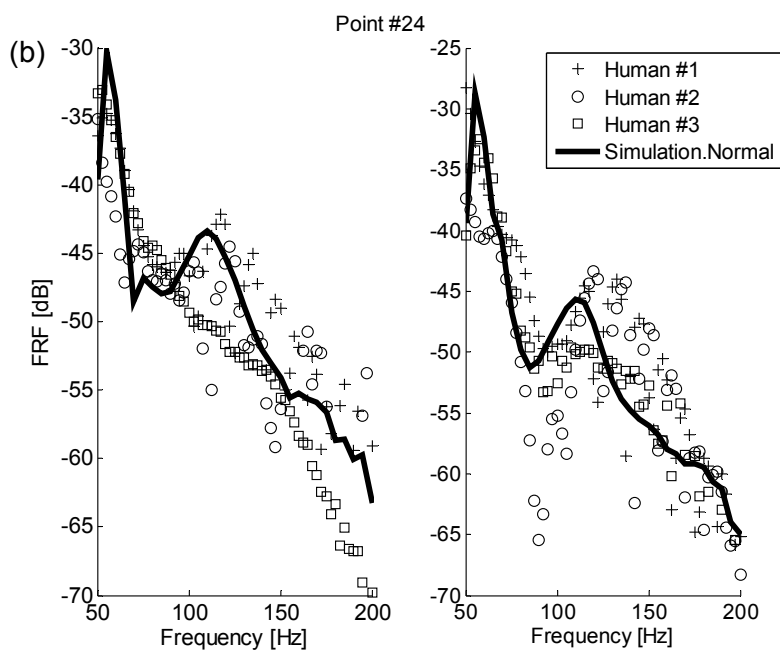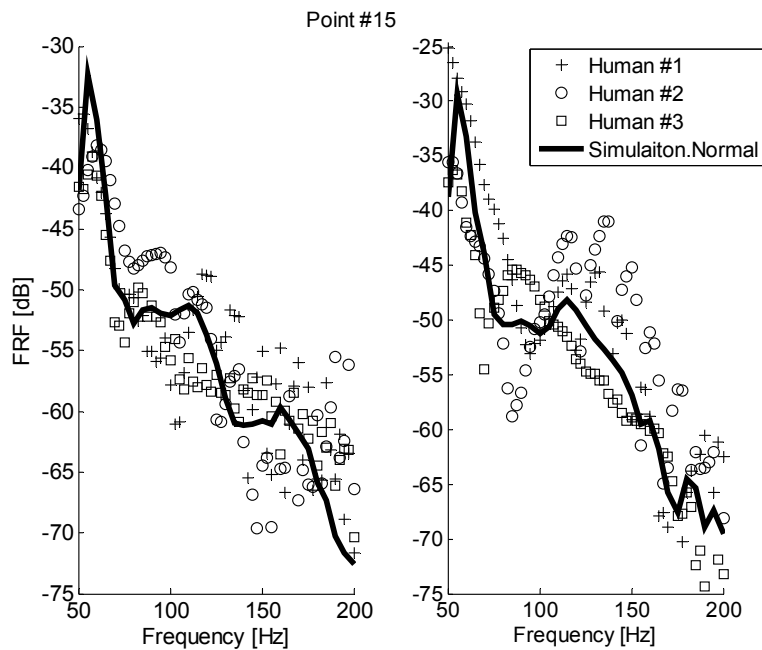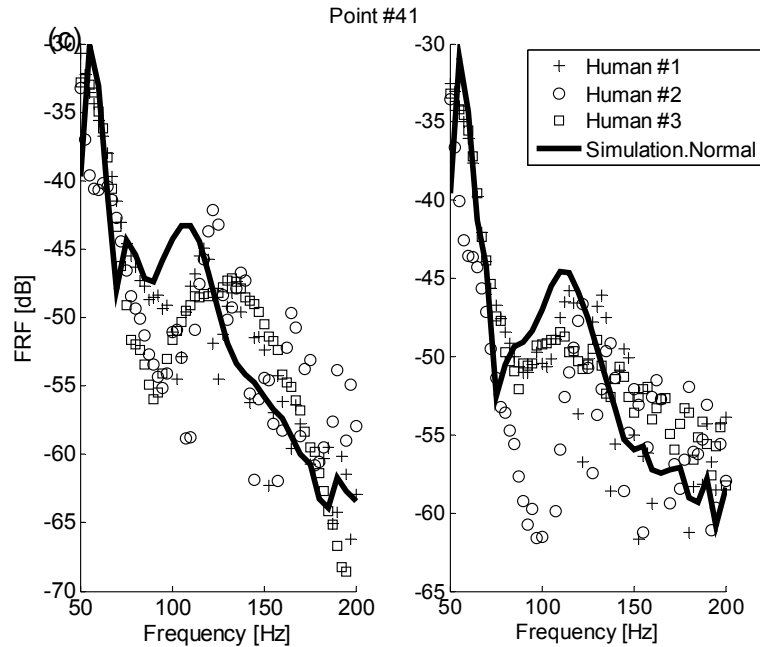
Figure 2.5 FRF plots at point #15(a), #24(b), and #41(c) on posterior chest (left/right sides correspond to left/right columns). Key: '—' simulation FRF, '+' HS #1 experiment, "○" HS #2 experiment, '□' HS#3 experiment.

The model was then used to predict FRF values at the posterior chest in a human subject for two different levels of PTX. Simulations were performed for PTX levels of 53% and 89% by volume, which corresponds to a lung air volume fraction of $\phi = 58\%$ and $\phi = 28\%$, respectively. Fig. 6 shows the FRF for the normal and the two PTX states. This prediction suggests that PTX may cause a drop in FRF at frequencies between 100-200 Hz. Specifically, in this frequency range there was an average reduction of 5.61 dB and 9.74 dB for the PTX levels of 53% and 89%, respectively. This is comparable to and consistent with the porcine study results of Fig 3(c), (d). The prediction further suggests that the FRF drop may be higher at larger PTX values and at higher frequencies for the smaller PTX state.
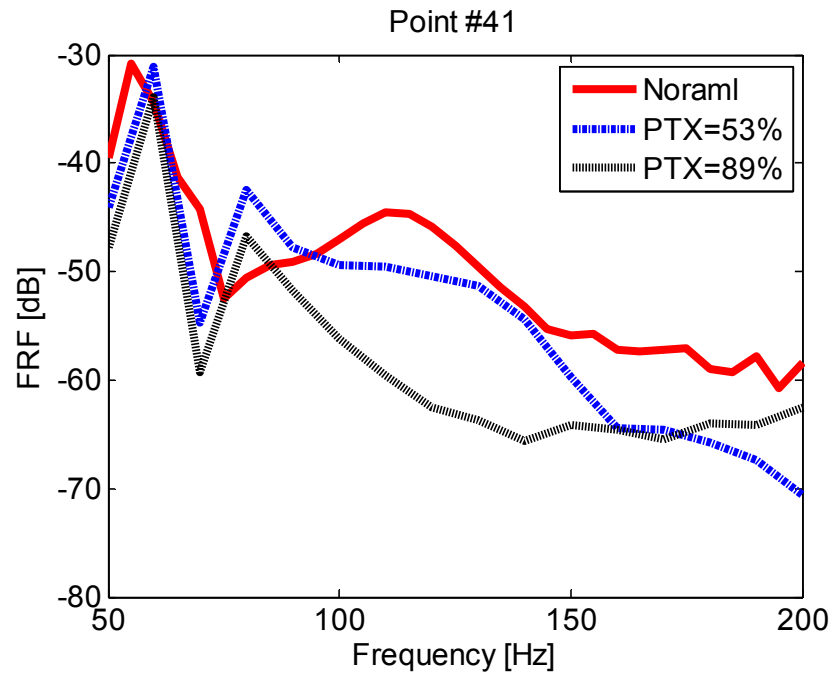
Figure 2.6 FRF amplitude of points #41 on right side of the posterior chest of the normal and PTX states (human simulation). Key: "—" PTX=0%; "‐‐" PTX=53%; "▪▪▪" PTX=89%.

In Fig. 2.7, the FRF amplitudes are shown for two different PTX levels of 53% and 89% at two specific frequencies 60 Hz and 120 Hz. As seen in the figures, when comparing right to left posterior side FRF amplitudes (only right lung is collapsed), the FRF amplitude reduction caused by PTX is evident, as previously observed in Fig. 2.6.
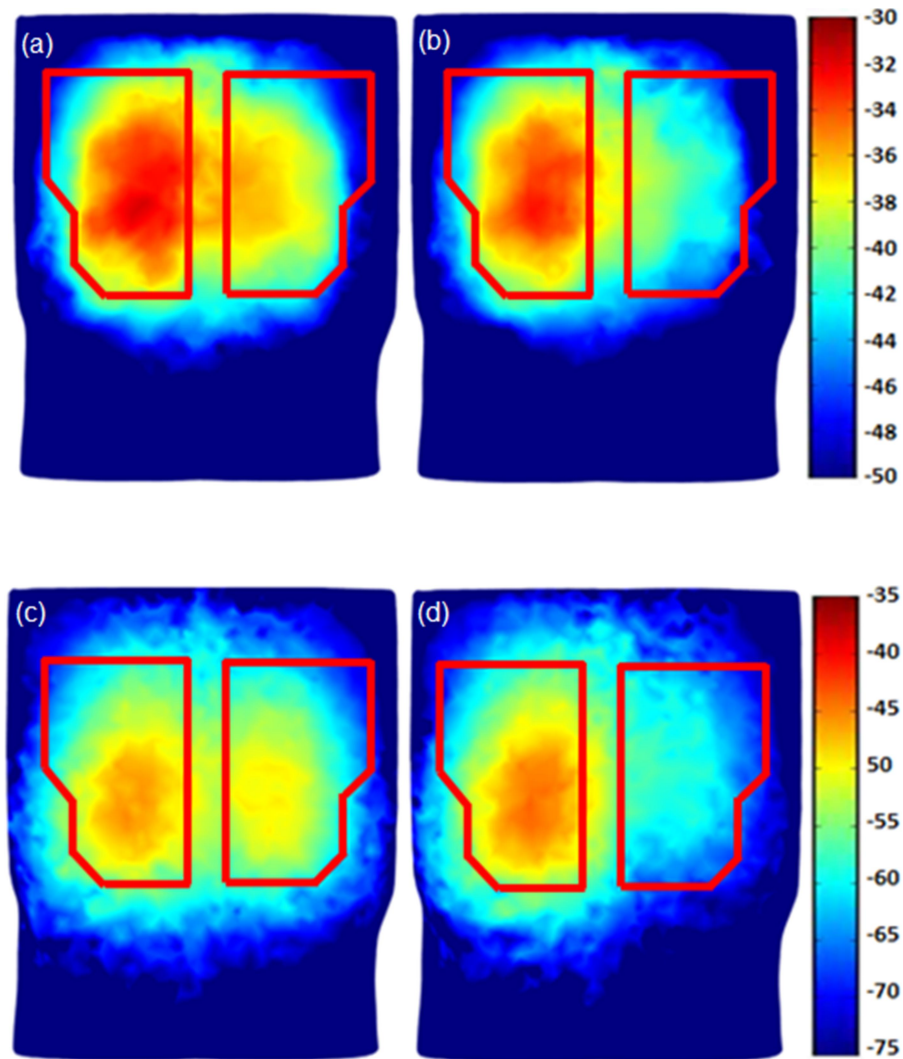
Figure 2.7 Human simulation results for PTX: (a) PTX = 53% and the excitation frequency is 60 Hz; (b) PTX = 89% and the excitation frequency is 60 Hz; (c) PTX = 53% and the excitation frequency is 120 Hz. (d) PTX= 89% and the excitation frequency is 120 Hz.

The model was also used to simulate the displacement of the lungs and other chest structures in response to surface excitation. Displacement in the anterior posterior direction in a torso cross section is shown in Fig. 2.8 at two excitation frequencies, namely 60 Hz and 120 Hz.  In this simulation, the right lung was collapsed, the left lung was kept normal, and the surface excitation was located at the middle of the top chest surface (over the sternum).  Patterns of shear waves emanating from the stimulus and

propagating into the chest are evident and are shown as red and blue (indicating high and low amplitude) bands.  These patterns are altered in the lung region as the acoustic properties are significantly different from the surrounding tissue.  One interesting aspect of this data is that the displacement amplitude in the normal left lung is higher than that in the PTX right lung.  As mentioned in the Introduction, simulation images such as those shown in Fig. 2.8 may provide better understanding on wave motion obtained from MRE and help in estimating soft tissue viscoelastic properties from MRE wave images.
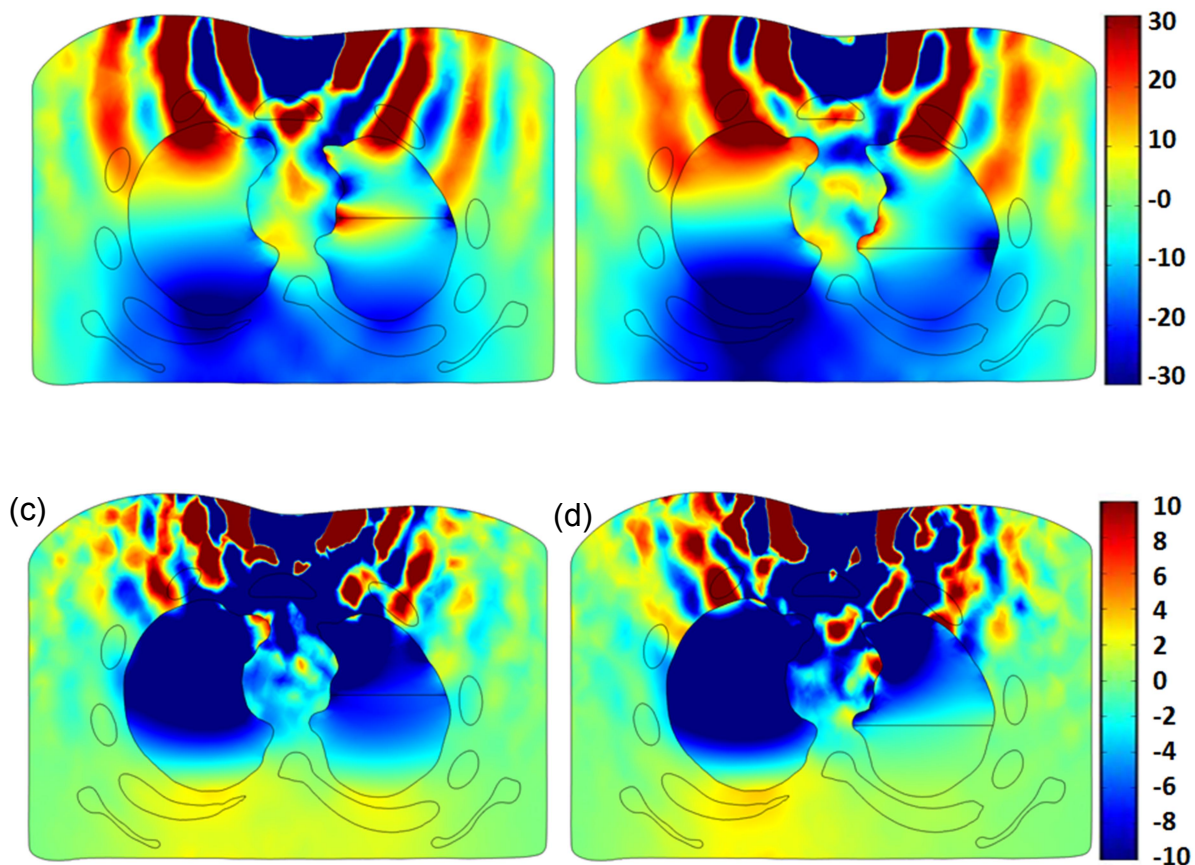


Figure 2.8 Human simulation at 60 and 120 Hz excitation frequency: cross section of torso showing displacement in the anterior posterior direction for (a) PTX= 53% at 60 Hz, (b) PTX=89% at 60 Hz, (c) PTX= 53% at 120 Hz, and (d) PTX=89% at 120 Hz in the right lung. The color bar shows displacement in [μm].

## 2.4    Discussion

Percussion is a common procedure during clinical chest exams.  The tapping stimulus used in CP and AP, is short and contains relatively low frequencies.  The short signal duration limits the amount of energy input.  This may lead to low signal-to-noise ratios especially at higher frequencies, which can reduce reliability.  In addition, the manual approach of the technique that relies on un-aided listening can be subjective, skill dependent and sometimes tedious.  This can pose further limitations on the utility of the technique.  The current study attempts to investigate enhancement of the technique by changing the stimulus and analysis methods.  Here, input waves are more controlled, introduced for a longer duration (30 seconds vs. < 1 second), and contain a wider frequency band.

The current study is also primarily aimed at developing a finite-element computational model based on tissue properties available in the literature and realistic 3D geometries extracted from actual CT scans of humans and animals.  The model was validated for animal and human geometries and computational predictions are consistent with experimental measurements. Though, we note that the human simulation with PTX was not validated experimentally in the present study. But, differences in the human simulation between normal and PTX cases matched those observed in the porcine simulations for normal and PTX cases, both of which were validated experimentally. One underlying hypothesis is that higher-frequency mechanical waves introduced at anterior chest surface propagate to the posterior chest through internal organs lying between the stimulus and measurement points.  The change in the relevant intra-thoracic structures would alter the wave propagation through the thorax, and hence

results in amplitude modification at the measurement location. Model predictions and experimental results showed that changes in the lung structure due to the presence of PTX (which creates more barriers to the acoustic waves due to additional impedance mismatch between lung, air, and chest wall) caused a drop in the FRF at higher frequencies, which is consistent with this hypothesis. Sound waves at lower frequencies on the other hand (due to their lower attenuation) can travel a longer distance around the internal organs. And consequently, structural changes of the internal organs may have a small effect on the transmission of these waves. This is consistent with the study findings that the presence of PTX had smaller effects on sound transmission at lower frequencies. Given the above hypothesis, one can argue that when PTX is present, the barrier it creates to the sound waves may lead to channeling more acoustic energy around the internal organs. Adding this possibility to the lower attenuation of the low frequency sound waves, an increase in the FRF value at the posterior chest may take place at lower frequencies. This may explain the results of Fig. 3(c) and (d) where a small increase in FRF was seen at low frequencies.

The effect of PTX on transmitted sound (Fig. 2.3 (c) and (d)) is consistent with earlier reports [57] where the transmitted sound amplitude was investigated in dogs with PTX. In that study the reduction of transmitted sounds with PTX was seen at frequencies 20-1500 Hz, while low frequency (< 100 Hz) transmitted sounds were not significantly affected. That finding also suggests that that FRF drop seen in the current study may continue at frequencies higher than those introduced in the current study. The maximum frequency in the current project was limited 400 Hz to keep the SNR

sufficiently high. The frequency range with high SNR may be widened when higher sensitivity sensors are available.

Significant inter-subject variability was seen in pig (Fig. 2.3(a)) and human (Fig. 2.5) studies. Variability may be due to the subject anatomical and size differences as well as varied measurement locations and measurement errors including human subject movement. However, there were similar general trends in each subject group and among both groups. For example the FRF decreased by about 30-40 dB as the frequency increased from 50-200 Hz for both the animal and human subjects, as the tissue acoustic properties were close between human and pig. The observed decrease in the transmitted acoustic energy with increasing frequency is consistent with previous studies [56] that suggested that the effect is due to increased attenuations with increasing frequency in biological tissue. It is also worthwhile noting that the FRF amplitude drop in 50-200 Hz range in the current study is comparable to previously reported values in the same frequency range [57] for canine subjects where the chest dimensions were close to half that of the current human subjects. This suggests that chest size may have a small influence (compared, for example, to tissue properties and acoustics barriers like the scapulae) on this frequency dependent attenuation.

In Fig. 2.5, the measured FRF shows peaks around 130 Hz. This trend is similar to simulation predictions and can be due to resonance in the chest, which is consistent with previous reports [57, 100]. Fig. 6 suggests that larger PTX may cause a larger FRF amplitude drop. This may be due to the increased size of the region of acoustic mismatch, which may be associated with more sound attenuation [27, 57, 101]. This result also suggests that the FRF amplitude drop may be too small to detect a small

PTX, which would limit the utility of the current approach, especially when a single point measurement is used. Spatial distributions of the simulated FRF amplitudes at 60 and 120 Hz for PTX of 53% and 89% are shown in Fig. 2.7. By examining that distribution, a difference of the FRF values over the left vs. right can be seen for both PTX levels. This data suggests that left to right FRF pattern comparisons may be helpful in detecting most moderate PTX. The left to right comparison may be useful in most cases since about 98% of PTX cases are unilateral [2].

As discussed above, sound transmission through the chest may be of value if altered transmission patterns correlate with pathology in ways that can be detected and used to provide a reliable and quantitative diagnosis of the disease or injury. Potential means of detection may be via measurement of the transmitted sounds on the torso surface, as done in this study, or via visualization of internal sound transmission using an imaging technique that measures internal vibratory motion, such as MR elastography. In either case, an accurate computer simulation of sound transmission through the chest and lungs under normal and pathologic conditions (Fig. 2.8) may aid in interpreting experimental measurements [60]. In this study, validated computational acoustic models proved to be capable of simulating transmission and noninvasive measurement of sound and vibration throughout the chest. The outcome of these models may also prove useful in the development of a more effective educational tool for teaching auscultation skills

## 2.5    Conclusion

In the present study, a computational model of sound transmission in the chest for surface acoustic excitation was developed.  The model was validated experimentally using data from three healthy human subjects and from six porcine subjects before and after pneumothorax induction. Model predictions were found to be consistent with findings and physical phenomena suggested by the animal and human studies.  The tested surface excitation method is an extension of the percussion approach that is commonly used during chest exam.  Simulation and experimental findings suggest that surface excitation may be useful in detecting pulmonary abnormalities such as a large PTX. The model may also prove useful for detecting other abnormalities, and developing learning tools.  The developed computational models can also predict wave propagation inside the chest which may be of use in assessing the performance of other acoustic diagnostic approaches, such as MR elastography.

**CHAPTER 3**

**3. A COMPUTATIONAL MODEL OF SOUND TRANSMISSION THROUGH THE**

**EXCISED PORCINE LUNG CAUSED BY AIRWAY INSONIFICATION**

(Previously published as (1) Peng Y, Dai Z, Mansy HA, Sandler RH, Balk RA, and Royston TJ (2014) Sound transmission in the chest under surface excitation: an experimental and computational study with diagnostic applications. Med Biol Eng Comput 52:695–706. (2) Dai Z, Peng Y, Henry B, Mansy HA, Sandler RH, Royston TJ (2014) A Comprehensive Computational Model of Sound Transmission through the Porcine Lung. J. Acoust. Soc. Am. (3) Henry B, Dai Z, Peng Y, Mansy HA, Sandler RH, Royston TJ (2014) Investigation of pulmonary acoustic simulation: comparing airway model generation techniques. Proc. SPIE 9038, Medical Imaging 2014: Biomedical Applications in Molecular, Structural, and Functional Imaging, 90380; doi:10.1117/12.2043643; http://dx.doi.org/10.1117/12.2043643)

## 3.1  Introduction

### 3.1.1  Motivation

The lungs are a unique, multiphase porous structure that have defied conventional noninvasive medical imaging methods and our ability to contrast and quantify changes in macroscopic properties that can be indicative of disease and which may be fundamentally linked to pathophysiologic and structural changes at the microscopic level. A wide range of pulmonary ailments result in significant changes, locally or diffusely, to the stiffness or density of lung tissue, with findings that include inflammation, fibrosis, edema, consolidation, or a mass effect (e.g., tumors). These changes often are not easily identifiable by currently available imaging modalities.

The utility of conventional ultrasound pulmonary imaging is limited due to the acoustic impedance mismatch between the air in the lungs and soft tissue. X-ray computed tomography (CT) and magnetic resonance imaging (MRI) provide useful anatomic information, but are often limited in their diagnostic accuracy, especially in distinguishing benign, infectious and malignant pathologies. CT also has the disadvantage of cancer risk associated with ionizing radiation. Moreover, it is suggested that Radio frequency (RF) tagging techniques of MRI are able to be used to access regional mechanical properties of the tissue [18, 66]; However,  this approach is limited duo to the changes in lung volume among the respiratory cycles.

Alterations in the structure and function of the pulmonary system that occur in disease or injury often give rise to measurable changes, spatially and temporally, in lung sound production and transmission that, if properly quantified, might provide additional information about the etiology, severity and location of trauma injury or other pathology [46, 56, 57, 74]. Indeed, simultaneous, multi-sensor auscultation methods have been developed to "map" sounds on the thoracic surface by several groups [3, 4, 12, 71, 74, 75]. Also recently, the phase contrast-based technique known as magnetic resonance elastography (MRE), has been applied to the lungs in pilot studies with limited success [28, 61–63]. MRE seeks to provide a map of the viscoelastic properties within the region of interest that will affect the shear wave motion that MRE measures. Previously, MRE has been successfully applied to the study of the mechanical properties of a variety of other organs and soft tissue regions in vivo, including the breast, brain, kidney, prostate, liver and muscle [42, 43, 45, 85, 89]. Application to the lungs has proven more challenging, given the poor signal-to-noise available in imaging due to a lower presence

of hydrogen in air than in soft tissue (containing water), and the complex nature of vibratory wave propagation found in the lungs. A better understanding of mechanical wave motion in the lungs would aid in the interpretation of the wave images that are acquired using MRE to reconstruct a quantitative map of variation in mechanical properties that can correlate with injury, the progression of disease and/or the response to therapy.

### 3.1.2  Literature review

The lung parenchyma is comprised of soft biological tissue and vasculature, as well as millions of microscopic air sacs (alveoli) that are connected through a complex branching airway structure. Microscopically the lungs are highly heterogeneous in terms of their physical properties, combining gas (air) that is linked through a complex and tortuous network of channels and microscopic sacs, non-Newtonian liquid (blood) that flows through an equally complex network of vessels of wide-ranging dimensions, and solid tissue structure comprised of a mixture of viscoelastic soft tissues that exhibit nonlinear behavior under large deformation.

Sound transmission in the pulmonary system can be analyzed by separating it into the airway acoustics and lung parenchymal acoustics. The acoustics of the respiratory airway tract can be further separated into the supraglottal and subglottal components. Our focus here is the subglottal region, which consists of the trachea that splits into the main-stem bronchi which further divide numerous times to create the complex bronchial trees. While the bronchial tree is extremely complex, geometrically it will exhibit less variability with time, relative to the supraglottal region, as voluntary actions of the subject will not significantly alter its geometry, unlike the subject's ability to alter the

glottal opening, tongue position, throat and mouth geometry, etc. In this article a comprehensive technique for relating the acoustic pressure throughout the bronchial tree to the acoustic pressure just below the glottis is developed.

The model of sound propagation in the subglottal airways consists of two fundamental parts.  First, it requires a mathematical description of the acoustic properties of individual airway segments, the description of which must be sufficiently sophisticated to include all of the phenomena of the gas and airway wall considered to be significant. Second, the dynamical description of individual airway segments must be integrated into a complex asymmetric airway tree encompassing up to several million branch segments if one attempts to model airway details down to the aveoli.  This task can be tackled by using the Horsfield self-consistent model of asymmetric dichotomy for the bronchial tree. Horsfield et al.[36, 38] proposed an approximate but comprehensive model based on detailed lung castings for both human and canine subjects. The Horsfield model of the human lung categorizes the airway tree into 35 different segment sizes, starting with $n$ = 35, the trachea, and ending with $n$ = 1, the terminal bronchiole, which itself terminates into two alveoli. It specifies the degree of asymmetry at each airway bifurcation through a recursion index called $\Delta^{(n)}$.  An airway of order n bifurcates into two airways of order n-1 and $n$-1-$\Delta^{(n)}$.  The Horsfield model is self-consistent in the sense that, for a particular airway order n, the bifurcated airway types (or daughter airways) are the same throughout the lung.

For the purpose of developing a tractable set of equations for predicting small-amplitude mechanical wave motion in the parenchyma for wavelengths larger than the microscopic heterogeneous features of the lung, macroscopic homogenized

representations of the lung's physical properties have been proposed. Based on this homogenous or stochastic spatially-averaged view, two different models for wave propagation have been put forth. One is sometimes referred to as the "effective medium" or "bubble swarm" theory. It has been prominently used in the literature for modeling lung acoustics since the 1980's [77, 79, 102]. More recently, there has been an interest in applying Biot's theory of poroelasticity to the lung [18, 86]. Application of Biot theory leads to a more complex theoretical model that predicts more wave types as compared to the effective medium theory.

### 3.1.3 Objectives of this study

The objective of the present study is to introduce and experimentally validate a comprehensive computational simulation model of sound transmission through the porcine lung. Airway and lung parenchymal acoustics are reviewed in Sec. 3.2. Experimental measurements on the surface of the excised lung using scanning laser Doppler vibrometry are covered in Sec. 3.3. The subject-specific model utilizing parenchymal and major airway geometry derived from x-ray CT images is described in Sec. 3.4. The lung parenchyma is modeled as a poroviscoelastic material using Biot theory. A finite element (FE) mesh of the lung that includes airway detail is created and used in COMSOL FE software to simulate the vibroacoustic response of the lung due to sound input at the trachea. In Sec. 3.5 the FE simulation model is validated by comparing simulation results to experimental measurements on the surface of the excised lung acquired using scanning laser Doppler vibrometry. The FE model is also used to calculate and visualize vibroacoustic pressure and motion inside the lung and its airways caused by the acoustic input. Finally the effect of diffuse lung fibrosis and a

local tumor on the lung acoustic response is simulated and visualized using the FE model.

## 3.2    Theory

### 3.2.1  Airway acoustics

It is of interest in the present study to be able to calculate the acoustic impedance (ratio of acoustic pressure to acoustic particle velocity as a function of frequency) as a function of the airway geometry and any changes it experiences. The Horsfield model, as modified by Habib et al. [31, 32] to account for non-rigid airway walls and terminal respiratory tissues renders this task possible. The first step is to calculate the input acoustic impedance at a terminal bronchiole,  $n$ = 1. Then, "march up" the recursion ladder from $n$ = 2, then 3 and so on until calculating the input impedance for $n$ = 35, the trachea. Referring to Fig. 3.1, for the $n^{th}$ order airway segment of length $l^{(n)}$, the input acoustic impedance $Z_{in}^{(n)}[\omega]$ (taken at the end closer to the trachea) is given by

$$Z_{in}^{(n)}[\omega] = \frac{Z_T^n[\omega] + Z_0^n[\omega] tanh\left[\gamma_0^{(n)}[\omega]l^{(n)}\right]}{1 + \left(Z_T^n[\omega]/Z_0^n[\omega]\right)tanh\left[\gamma_0^{(n)}[\omega]l^{(n)}\right]}, \quad n = 1,...,35 \qquad (3.1)$$

The terms $Z_0^{(n)}[\omega]$ and $\gamma_0^{(n)}[\omega]$ are the characteristic impedance and propagation coefficient of the $n^{th}$ airway segment, respectively, and are given in Royston et al [78].

The term $Z_T^{(n)}[\omega]$ denotes the acoustic impedance at the far end of each segment, which is given by

$$Z_T^{(n)}[\omega] = \begin{cases} \dfrac{N_T}{j\omega C_g + 1/\left[R_t + j\left(\omega I_t - 1/[\omega C_t]\right)\right]} & n=1 \\[4mm] \dfrac{1}{1/Z_{in}^{(n-1)}[\omega] + 1/Z_{in}^{(n-1-\Delta[n])}[\omega]} & n=2,...,35 \end{cases} \quad (3.2)$$

Here, $N_T$ denotes the total number of terminal ($n$=1) bronchiole segments, which are effectively in parallel with respect to the termination into the soft tissue of the parenchyma. For the Horsfield model, this can be calculated using the following recursion formula, taking $N_T^{(1)} = 1$ and $N_T = N_T^{(35)}$,

$$N_T^{(n)} = N_T^{(n-1)} + N_T^{(n-1-\Delta[n])} \quad (3.3)$$

The result is $N_T \approx 2.35$ million in this case. The term $C_g$ denotes the alveolar gas compression compliance based on the Dubois [21] six-element terminal airway model. Also based on the Dubois model, $R_t$, $I_t$ and $C_t$ denote the terminal tissue resistance, inertia and compliance. (The lumped airway wall inertance and resistance of the Dubois six-element model are replaced here by the more comprehensive airway tree model.)
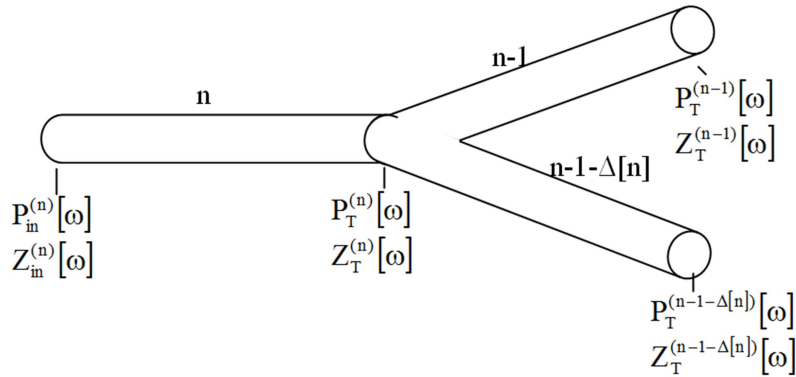


Figure 3.1 Airway acoustic model of one bifurcation.

### 3.2.2  Parenchymal acoustics

In previous Sec. 2.2, Biot theory of wave propagation in poroviscoelastic media and the effective medium theory were discussed that Measurements of compression wave speed and attenuation in freshly exercised pig lung matched theoretical predictions based on Biot theory much more closely than did the effective medium theory.  Biot theory was applied to find out the material properties of the lung parenchyma (Eq. 2.1-2.4).

### 3.3    Experiment
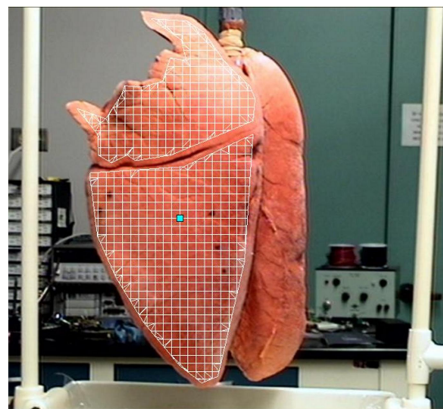


Figure 3.2 Experimental setup of SLDV measurement of lung surface motion.

SLDV measurements (Polytec PSV-400) on the surface of one suspended excised, preserved porcine lung (Nasco, Fort Atkinson, WI) subject to airway insonification were taken as shown in Fig. 3.2. The preserved lung was hung under a frame and inflated to a pressure of 20 cm $H_2O$ transpulmonary pressure for one hour before the experiment to help open the airways. During the experiment, that pressure was kept constant. Broad band sound (periodic chirp with spectral content from 50 to 1000 Hz and amplitude of about 1 Pa) generated by a 3.5 inch speaker (PDWR30W, PylePro,

Brooklyn, NY) was sent into the excised lung via the trachea. P-RETRO-250 glass beads (45 – 63 µm dia., Polytec, Irvine, CA) were spread on and adhered to the lung surface to enhance the laser reflectivity. The whole lung was scanned by the SLDV except the areas where the left and right lobe touched each other and some peripheral points without a clear line of sight to the laser. Four scans were made at different angles and then combined to cover the entire lung geometry. The lung was preserved using propylene glycol and its mechanical properties were stable and, although not the same, appeared close to that of live or freshly excised lung. This enables repeated experiments on the lung that take time. The SLDV measurements will be compared with computer simulations of lung excitation caused by airway insonification in Sec. 3.5.

## 3.4    Simulation

### 3.4.1    Lung and airway geometry construction

The preserved pig lung used in Sec. 3.3 was inflated at 20 cm $H_2O$ transpulmonary pressure and scanned in a CT scanner (Brilliance 64, Philips Electronics), with in plane pixel resolution of 512x512 and axial steps of 1 mm. The lung contour was constructed by importing the CT images into Mimics 14 (Materialise Group, Leuven, Belgium).

The geometry of pig lung airways was generated using an open source code medical image segmentation software ITK-SNAP Version 2.4. CT images were imported for automatic segmentation using the snake algorithm in ITK-SNAP [108]. The implementation of automatic segmentation allowed for a virtual base geometry to be constructed, which was used as a baseline for later models. Because of the way that automatic segmentation works in ITK-SNAP, however, only about twenty airway segments were created, since the quality of the segmentation is directly proportional to

the quality of the image. The airway tree generated by automatic segmentation is called airway #1. The white contrast was used for the automatic segmentation algorithm. The next set of models, therefore, were done manually, marking contrasted regions slice by slice. This was accomplished by marking the airway segments with the marker tool, and this was done according to the local contrasted region. A more complex and intricate airway tree (airways with a diameter of <3mm, the limit of the CT imaging in terms of contrasted region, creating a final model with around 500 segments) was generated and it was called airway #2. The lung CT images used for segmentation are shown in Fig. 3.3. The black regions inside the lung contour are the lung parenchyma, the white regions are the airway wall and the marked red regions are the air inside the airway. Both images are identical, except for the labeled airways. Fig. 3.3(a) shows the CT image with the labeling region for airway #1, and Fig. 3.3(b) shows the labeling region for airway #2.
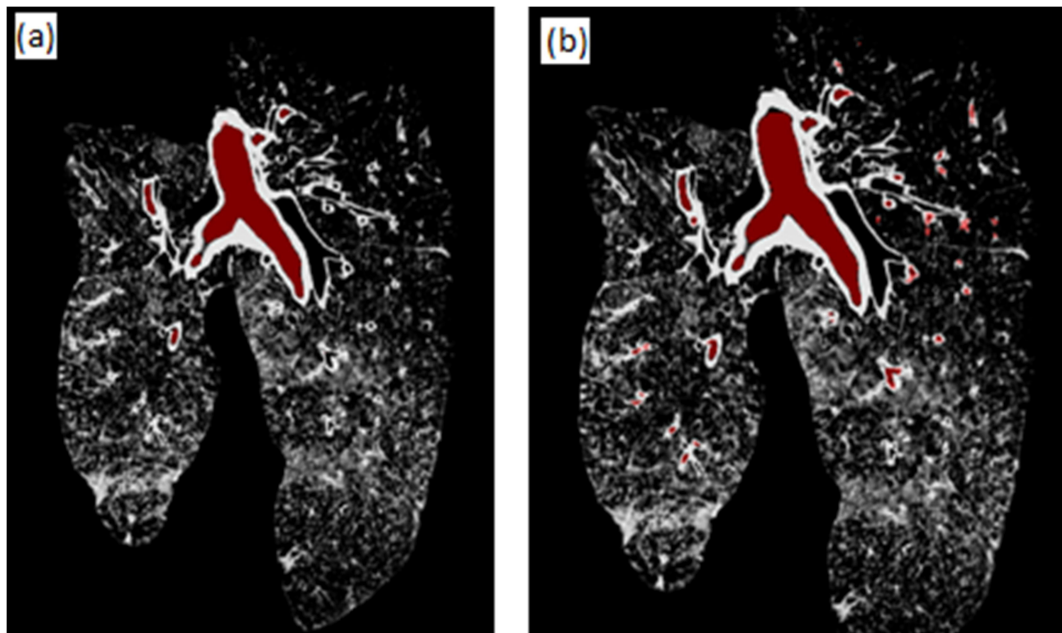


Figure 3.3  Lung CT images used for segmentation: (a) airway #1, (b) airway #2.

When the automatic and manual segmentation was completed for the airways, an additional manual segmentation step was performed on a thickness region surrounding the trachea and main stem bronchi. When all of the segmentation was completed, a surface tessellation algorithm was applied by ITK-SNAP in order to capture the three dimensional geometrical data, and this geometrical data was exported as a stereolithography (STL) CAD file so that it could be meshed properly in ANSYS. Fig. 3.4 shows the geometry of the two constructed airways.
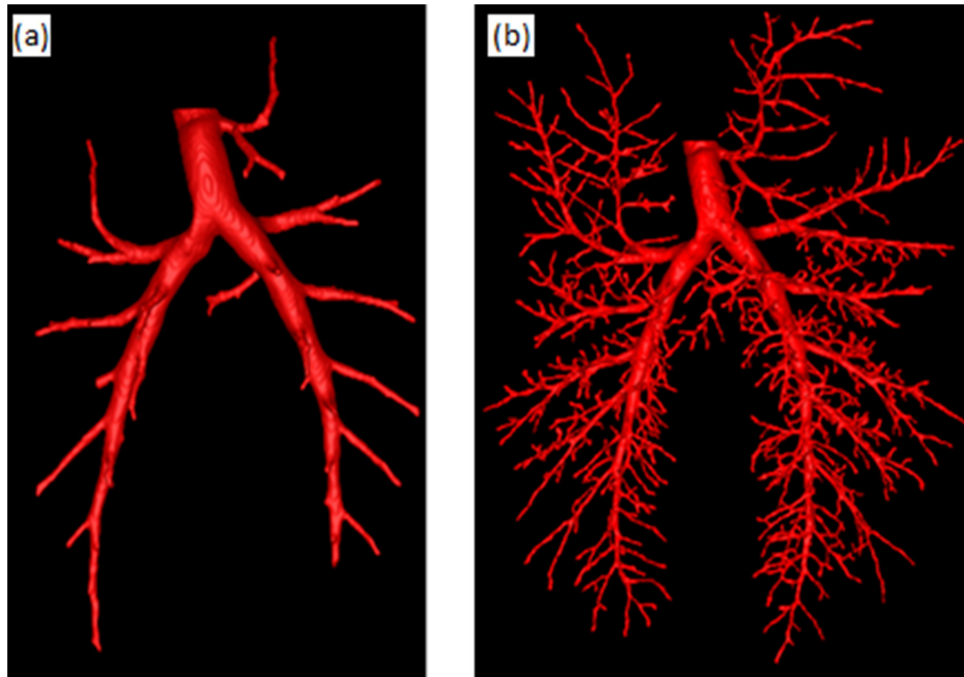


Figure 3.4 Geometry of the constructed airways: (a) airway #1, (b) airway #2.

Once the airway and thickness geometries were imported to ANSYS ICEM CFD 12.1 (Ansys Inc, Canonsburg, PA), a meshing tool provided by ANSYS, they were combined

with the geometry of the lung parenchyma. The geometry was checked in ANSYS for mesh quality, and once there were assurances that there were no problems with the geometry, it was volume meshed to create a finite element (FE) model. The volume mesh was imported into COMSOL 4.3a (COMSOL Inc, Burlington, MA) for simulation. Fig. 3.5 shows the volume mesh of the preserved pig lung with the different airway trees. The airway tree lumen (pink domain in Fig. 3.5) was specified as air. The airway tissue was a thin layer of about 2-3 mm surrounding the lumen and the rest of the mesh is the lung parenchyma.
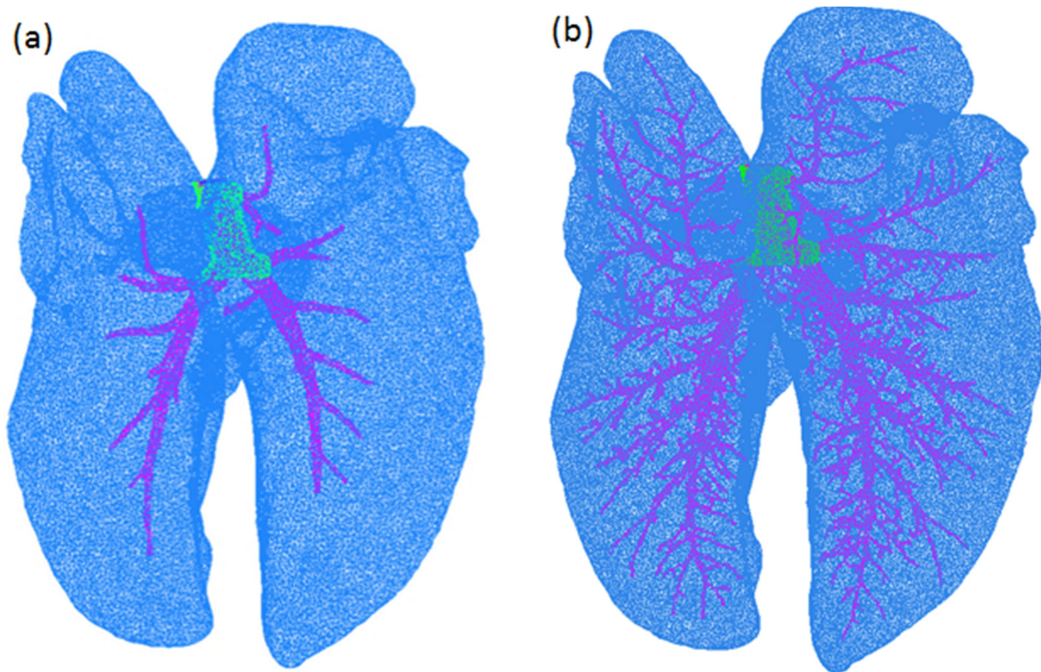


Figure 3.5 Volume mesh of lung with airway tree: (a) with airway #1, (b) with airway #2.

### 3.4.2  Finite element simulation of sound transmission in the lung

The acoustic structure interaction module of COMSOL 4.3a was used to simulate sound transmission in the preserved lung. The lung parenchyma was modeled as a viscoelastic solid by specifying its complex compression and shear wave speed. The airway tissue was modeled as a viscoelastic solid by specifying its complex Young's modulus taken from Suki et al. [92]. Both airway #1 and 2 are simplified airway trees; their distal airway segments are un-modeled due to the limit of the CT image resolution. So, the terminal impedance of the terminal segments (segment which stops bifurcating into daughter segments) needs to be calculated to represent the un-modeled downstream airways. The morphometry of the pig airway tree appears to be close to that of the human airway tree, especially the segments with small diameters. The Horsfield model is a structural model which is used for most mammalian airway trees; to the best knowledge of the authors, there is no such detailed structural parameters (including the order number and recursion index) for the pig airway tree. So, the human airway structural parameters are used to calculate the pig airway terminal impedance. An order number needs to be specified for the terminal segments of pig airway #1 and 2. The standard deviation of the terminal segment diameter is small such that the terminal segments are regarded as the same and their order number is found by relating their mean diameter to the closest value in Table 9-2 in Royston et al [78]. For airway #1 and #2, their terminal segment mean diameter is 0.258 cm and 0.115 cm, respectively; these correspond to the order number 17 and 12, respectively. Then the terminal impedance can be calculated by Eq. (2.2). Fig. 3.6 shows some terminal segments of airway #2 where the terminal impedances were specified. A harmonic sound pressure

input of amplitude 1 Pascal was applied at the trachea inlet. The number of tetrahedral elements of the lung with airway #1 and airway #2 is 748,583 and 842,607, respectively. To ensure convergence and accuracy, the element size is smaller than the one sixth of compression wave length at 800 Hz. The simulation was performed at 300 Hz, 500 Hz and 800 Hz. The lung density at 20 cm H2O is taken to be 250 $kg/m^3$. The airway wall tissue density is taken to be 1000 $kg/m^3$ and its Poisson's ratio to be 0.49998. The compression speed $c_p$ and shear wave speed $c_s$, the terminal impedance of airway #1 and #2 ($Z_T^{(17)}$ and $Z_T^{(12)}$) and the airway Young's modulus E are all frequency-dependent and they are listed in Table 3.1. The lung shear modulus was measured by the surface wave method [80] and fit by a fractional Voigt model as $\mu = [3.67 \times 10^3 + 235.09(j\omega)^{0.43}] \, Pa$. The complex shear wave speed was derived from Eq. (2.2). The compression wave speed was calculated by Eq. (2.3a).
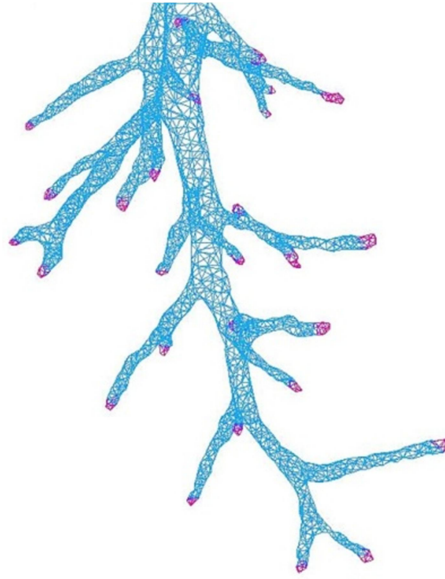


Figure 3.6 Airway #2 with terminal impedance specified (pink areas).

Table 3.1 Lung parenchyma and airway parameters in simulation

|  | 300 Hz | 500 Hz | 800 Hz |
|---|---|---|---|
| $c_p$(m/s) | 27.09 + 5.64i | 29.25 + 7.55i | 31.81 + 9.12i |
| $c_s$ (m/s) | 5.95 + 1.26i | 6.37 + 1.47i | 6.82 + 1.68i |
| E (MPa) | 0.28+0.93i | 0.28+1.55i | 0.28+2.49i |
| $Z_T^{(17)}$(Pa·s/m) | 16.23+30.22i | 18.76+51.10i | 25.37+92.14i |
| $Z_T^{(12)}$(Pa·s/m) | 11.54+8.40i | 10.76+16.09i | 10.44+28.04i |

### 3.4.3  Effects of diffuse lung fibrosis and local tumor

Many pulmonary ailments such as inflammation, fibrosis, edema and tumors result in significant changes, locally or diffusely, to the stiffness or density in the lungs that will affect wave propagation in the lungs. The FE simulation enables the visualization of the wave field in the lungs and can provide insight into changes in stiffness or density. Lung fibrosis and tumors are simulated as two representative pulmonary pathologies. It is reported that bleomycin-induced lung fibrosis locally increases median tissue stiffness 2-6 times relative to normal lung parenchyma [22, 53]. To the best knowledge of the authors, there are no reports in literature about the macroscopic shear viscosity of fibrotic lung tissue under our frequency range of interest (100-2000 Hz). The macroscopic shear viscoelastic properties of lung tumors are also lacking in the literature. Sinkus et al. [91, 92] applied harmonic shear wave excitation at 65 Hz and a direct-inversion modulus estimation to compare in vivo measurements made in six human breast-fibroadenoma patients with the results from six breast-carcinoma patients. Both the shear stiffness and shear viscosity of fibroadenomas and carcinomas were larger than the surrounding normal tissue. The shear viscosity had a large variation

while it was easier to differentiate malignancy from normal tissue by the shear stiffness. The shear stiffness increase ratio taken from the Sinkus study was used for the lung simulations here, extrapolated to our frequency range of interest as described below. For fibrosis and tumors, the shear stiffness was 1.5 and 3.33 times of those of the normal lung tissue, respectively. For lung fibrosis the shear viscosity was taken so that the shear wave attenuation (governed by the imaginary part of the shear wave number) was the same as the normal lung. For the tumor the increased shear viscosity always leads to smaller shear wave attenuation than the normal case; so, the shear viscosity which leads to the largest shear wave attenuation was selected. In the case of fibrosis the modified shear viscoelastic parameters were applied to the entire lung parenchyma, which also caused a slight change in compression wave speed. All other parameters in the FE simulation remained unchanged. Two spherical regions of diameter 30 mm and 20 mm were created in the FE lung model to represent local tumors, to which the modified shear viscoelastic parameters were applied. Table 3.2 lists the compression and shear wave speed for the lung fibrosis and tumor simulations.

Table 3.2 Compression and shear wave speed (m/s) for normal lung, lung fibrosis and tumor.

| Normal | 500 Hz | 800 Hz |
|---|---|---|
| $c_p$ | 29.25+7.55i | 31.81+9.12i |
| $c_s$ | 6.37+1.47i | 6.82+1.68i |
| Lung fibrosis | | |
| $c_p$ | 29.66 + 7.56i | 32.18 + 9.11i |
| $c_s$ | 7.95 + 2.36i | 8.53 + 2.69i |
| Tumor | | |
| $c_p$ | 32.13 + 9.23i | 34.47+10.40i |
| $c_s$ | 13.91 + 8.09i | 14.78 + 8.54i |

## 3.5    Results and Discussion

The experimental and simulation results are shown in this section. The experiments and simulation results are always displayed in the same color scale range. Simulations on these two cases with fewer elements (330,534 and 453,002 tetrahedral elements, respectively) gave nearly the same results as the presented simulations; so, there was confidence that the models used here had more than sufficient resolution for the frequencies considered.

In Figs. 3.7-3.9, the lung normal surface velocity magnitude from the experiments and simulation are displayed for the same regions and the color bar is in dB m/s for 1 Pa input acoustic pressure. The areas in the red dash line are the lung surfaces scanned in the experiment and the corresponding area in the simulation.  In Fig. 3.7 both the experiment and simulation show similar patterns of velocity amplitude distribution. The velocity amplitudes are largest in the central areas of the lung and then gradually decay in the peripheral areas. The lung surface response is asymmetric; generally, there is a larger area of high surface velocity on the left lung surface than on the right lung surface. The color distribution from the experiment is slightly more mottled compared with the simulation. This may be due to noise in the measurement, which resulted in a smaller than actual value of velocity amplitude measured at some scanning points. In addition, the structural inhomogeneity inside the lung may have made the sound transmission more complex than the current simulation can fully capture. The comparisons at 500 Hz and 800 Hz also show similar patterns of velocity amplitude distributions between experiment and simulation. It is observed that in general the lung surface motion at 500

Hz and 800 Hz is smaller than that at 300 Hz, as the compression and shear wave attenuation increases with frequency.

In Figs. 3.7-3.9 it's seen that the lung periphery has lower velocity amplitudes from the simulation than from the measurement. One possible reason is that when sound propagates in the airway tree, each airway segment expands and contracts, and radiates acoustic energy into the lung parenchyma. As the very small airway segments were not modeled in the finite element simulation, less energy couples into the lung parenchyma; so, the lung surface motion from the simulation is smaller than that from the experiment. Figs. 3.10-3.12 show the real part of the lung normal surface velocity for the experiment and simulation. The color bar has the scale of $\mu m/s$ for a 1 Pa input acoustic pressure. The real part of the velocity represents the lung surface motion at a specific phase angle or point in time. Like the velocity magnitude images, similar trends of velocity distribution between experiment and simulation can be seen. Though, trends agree better in the velocity magnitude distribution.
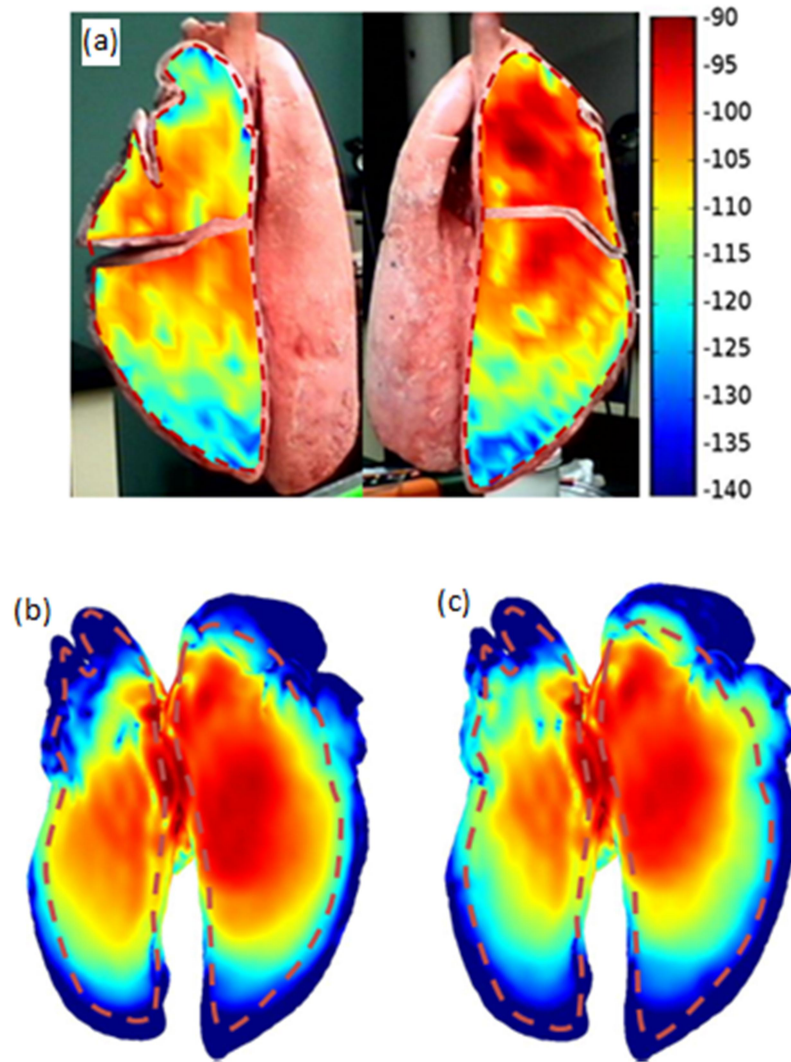
Figure 3.7 Lung normal surface velocity magnitude (dB m/s for 1 Pa input acoustic pressure) at 300 Hz (a) experiment (b) simulation, lung with airway #1 (c) simulation, lung with airway #2.
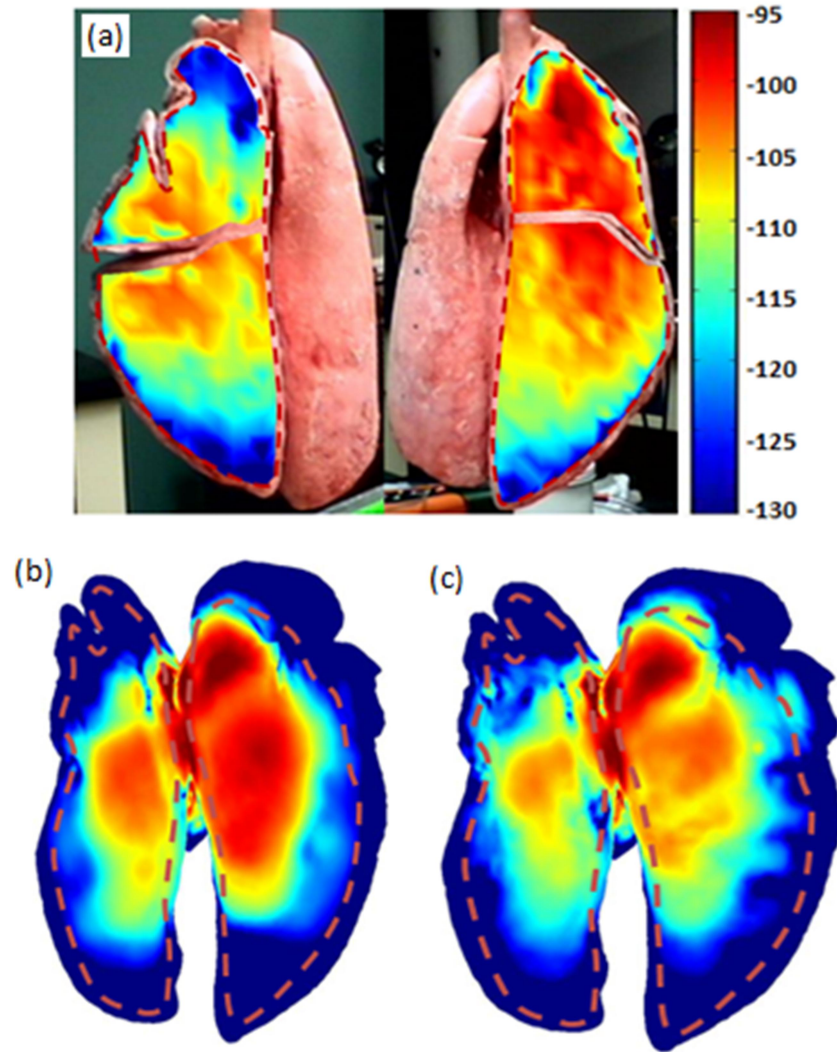
Figure 3.8 Lung normal surface velocity magnitude (dB m/s for 1 Pa input acoustic pressure) at 500 Hz (a) experiment (b) simulation, lung with airway #1 (c) simulation, lung with airway #2.
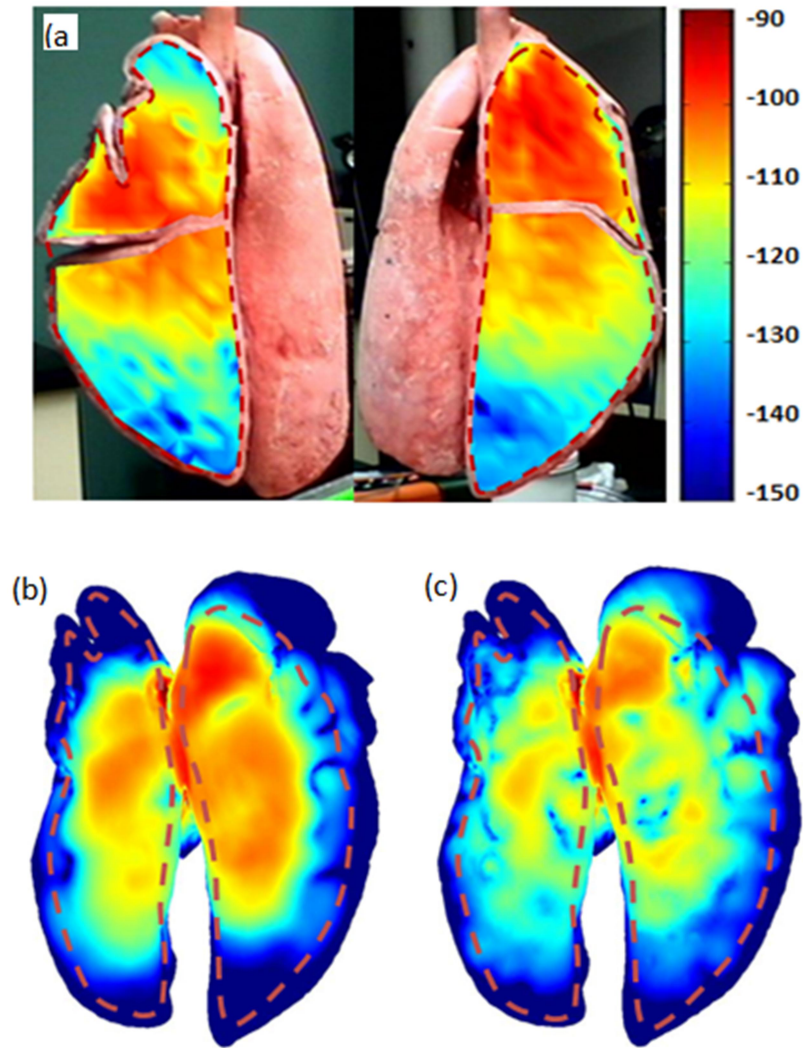
Figure 3.9 Lung normal surface velocity magnitude (dB m/s for 1 Pa input acoustic pressure) at 800 Hz (a) experiment (b) simulation, lung with airway #1 (c) simulation, lung with airway #2.
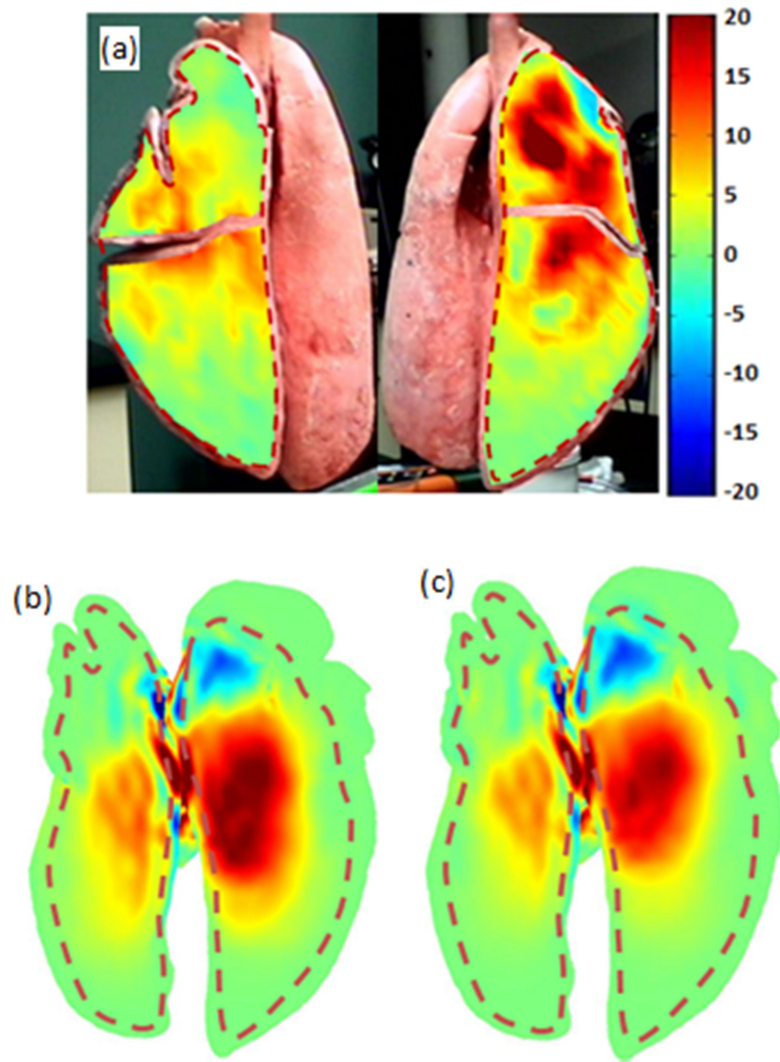
Figure 3.10 Real part of the lung normal surface velocity ($\mu m/s$ for 1 Pa input acoustic pressure) at 300 Hz: (a) experiment, (b) simulation, lung with airway #1 (c) simulation, lung with airway #2.
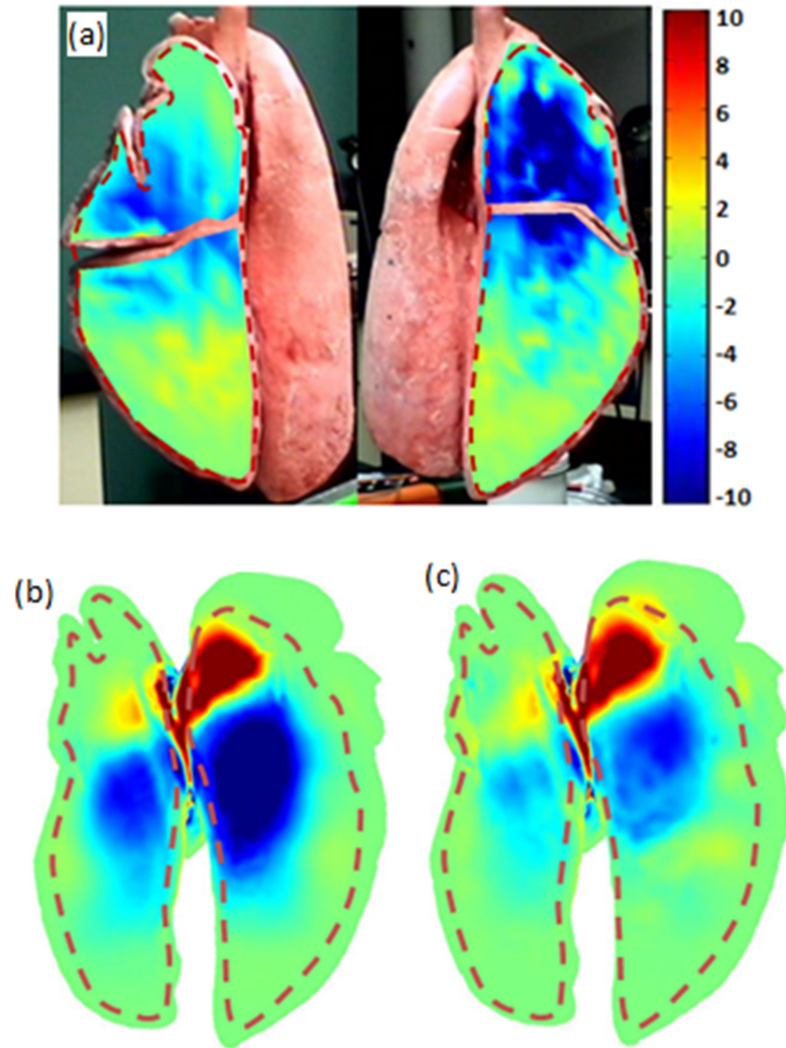
Figure 3.11 Real part of the lung normal surface velocity ($\mu m/s$ for 1 Pa input acoustic pressure) at 500 Hz: (a) experiment, (b) simulation, lung with airway #1 (c) simulation, lung with airway #2.
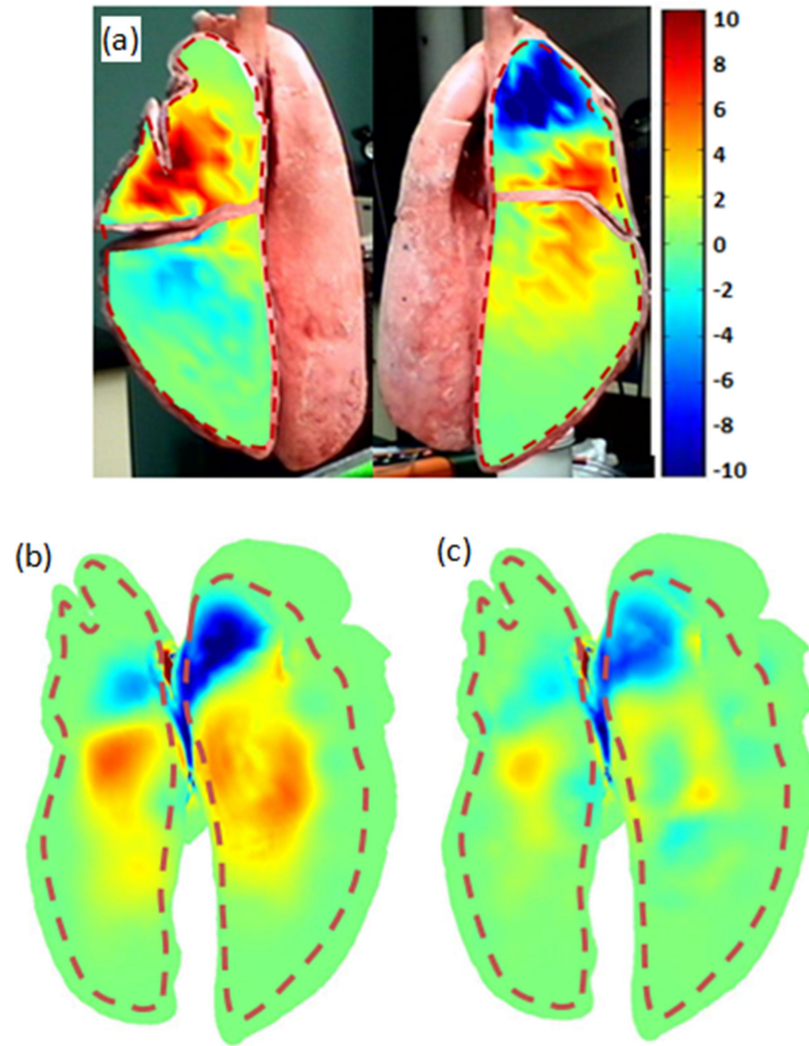
Figure 3.12 Real part of the lung normal surface velocity ($\mu m/s$ for 1 Pa input acoustic pressure) at 800 Hz: (a) experiment, (b) simulation, lung with airway #1 (c) simulation, lung with airway #2.
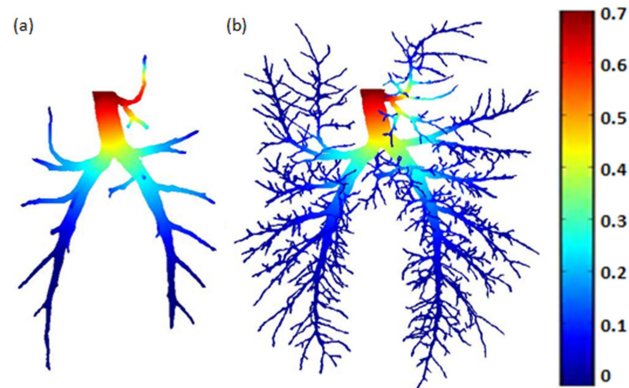
Figure 3.13. Real part of airway acoustic pressure (Pa) at 300 Hz: (a) airway #1 (b) airway #2.
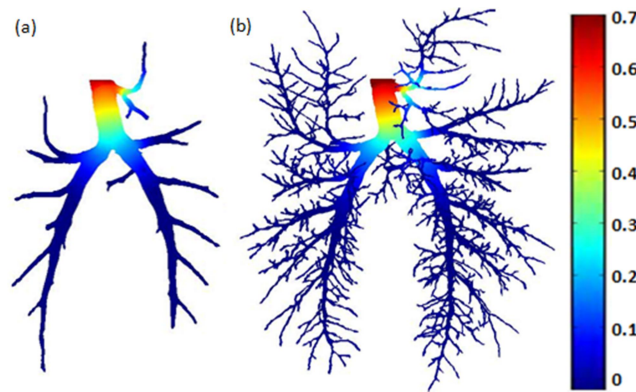


Figure 3.14 Real part of airway acoustic pressure (Pa) at 500 Hz: (a) airway #1 (b) airway #2.
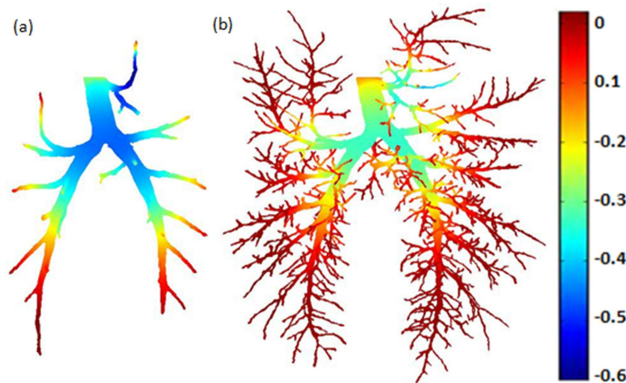


Figure 3.15 Real part of airway acoustic pressure (Pa) at 800 Hz: (a) airway #1 (b) airway #2.

While the SLDV only measures the lung surface motion, the computer simulations enable exploration of sound transmission inside the lung. Figs. 3.13-3.15 show the real part of airway acoustic pressure distribution at three different frequencies. For the large airway segments that both airway #1 and 2 have, their acoustic pressures are almost the same, this again shows that the simplified airway tree is nearly equivalent to the more detailed airway tree in terms of the airway acoustics of the larger airways. In Fig. 3.15, the real part of the airway acoustic pressure at 800 Hz is negative in some locations as the phase shift at 800 Hz was greater than that at 300 and 500 Hz.

Visual comparison of the two simulations with experiment in Figs. 3.7-3.12 suggests that the lung model with airway #1 provides a slightly closer match to experiment than the model with airway #2. This may seem counterintuitive as we might think that the more airway segments in the model, the closer the simulation to the experiment. The airway tree was constructed from CT images and the very small segments have relatively rough cylindrical shapes due to the CT resolution, which may not accurately represent the real case. Also it is observed in Figs. 3.13-3.15 that sound amplitude dramatically attenuates after several bifurcations at the frequencies considered; this suggests that most of the acoustic energy has left the airways prior to reaching the smaller segments represented in the airway #2 model.

Wave motion inside the lung can also be seen from the simulation. In Figs. 3.16, 3.18 and 3.20, five stacked horizontal slices spaced at 50 mm display the real part of the lung velocity in the anterior-posterior direction together with airway acoustic pressure. Cross-section images of the second top horizontal slice are shown in Figs. 17, 19 and 21. The real part of the velocity is in the y direction (anterior-posterior direction). Wave

propagations are seen more clearly in the cross-section images. These are compression waves based on the wave length. Table 3.3 lists the wave length estimated at these three frequencies and comparison with Biot theory predictions. It is found that at 500 Hz and 800 Hz the wave length estimated from simulation agrees well with Biot theory predictions. At 300 Hz the deviation is larger as the wave length is larger and there are fewer whole wavelengths in the lung cross section; reflections of finite boundaries may have more effect.
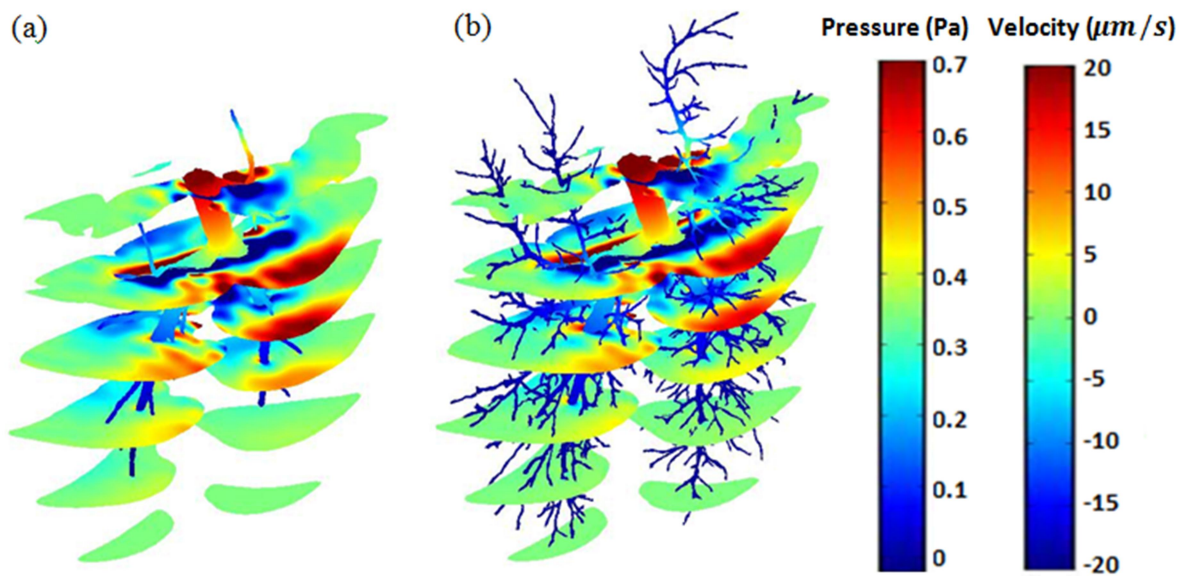


Figure 3.16 Stacked horizontal slices of the real part of the lung velocity in the anterior-posterior direction and airway acoustic pressure at 300 Hz.
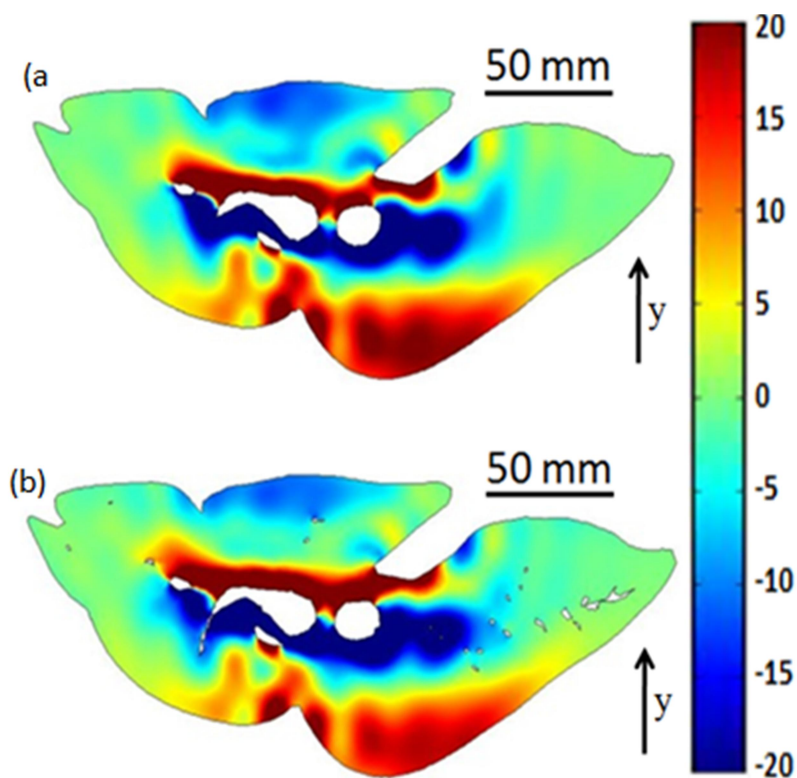
Figure 3.17 Cross-section Images of the real part of the lung velocity in the anterior-posterior direction (see arrow) in $\mu m/s$ at 300 Hz: (a) airway #1 (b) airway #2.
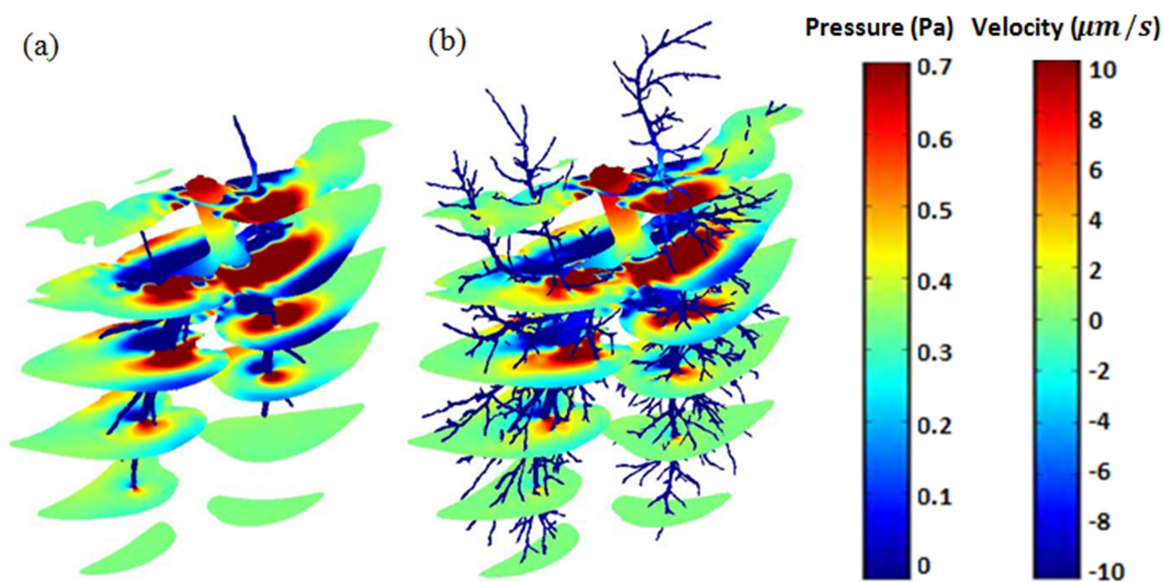


Figure 3.18 Stacked horizontal slices of the real part of the lung velocity in the anterior-posterior direction and airway acoustic pressure at 500 Hz.
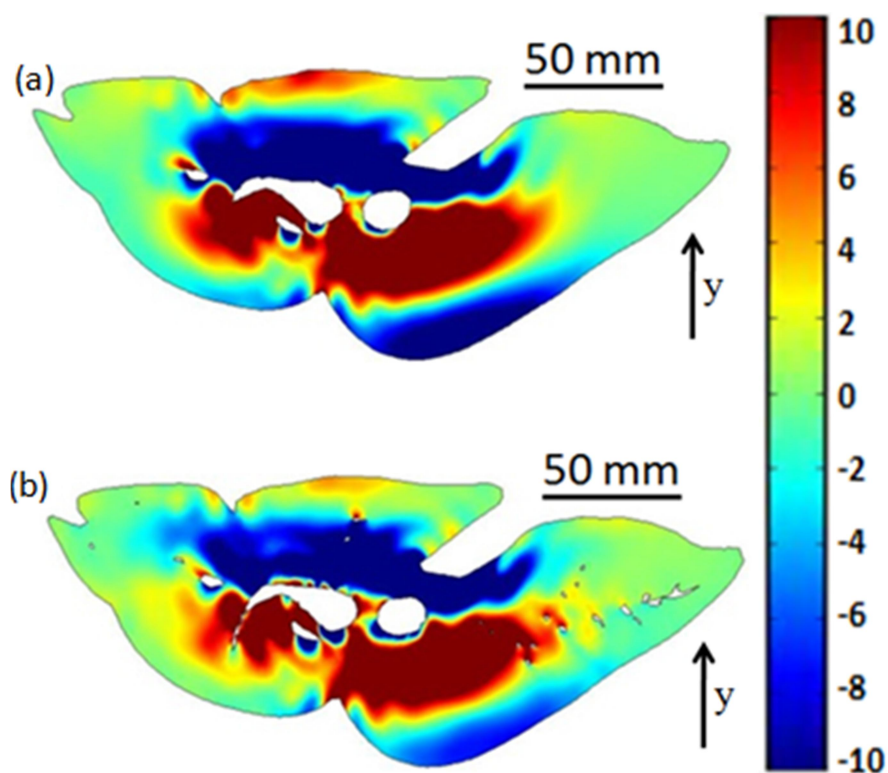
Figure 3.19 Cross-section Images of the real part of the lung velocity in the anterior-posterior direction (see arrow) in $\mu m/s$ at 500 Hz: (a) airway #1 (b) airway #2.
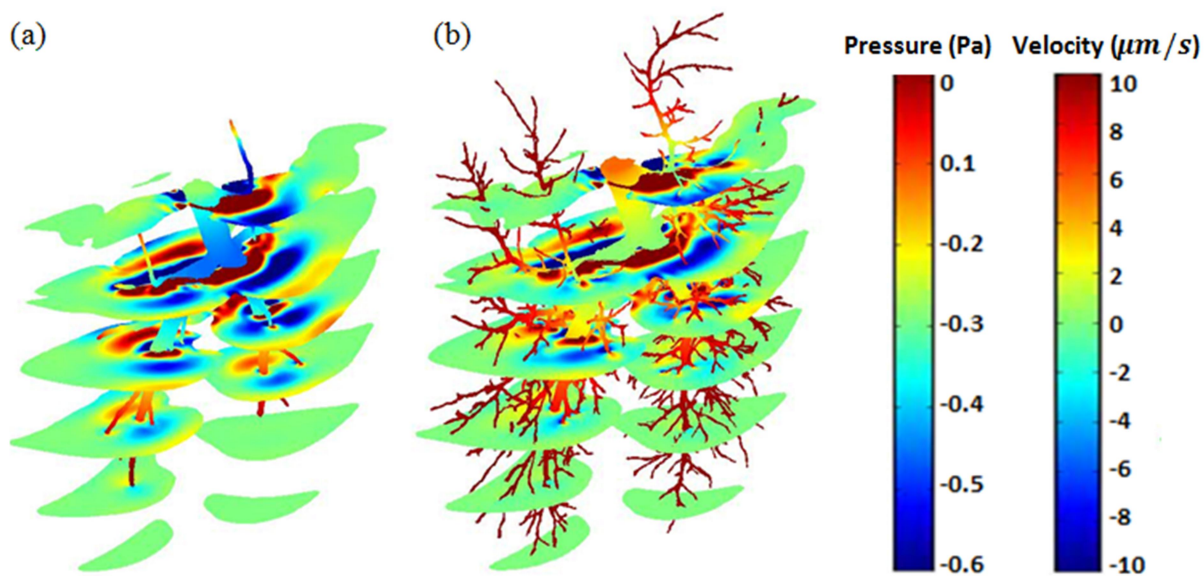


Figure 3.20 Stacked horizontal slices of the real part of the lung velocity in the anterior-posterior direction and airway acoustic pressure at 800 Hz.
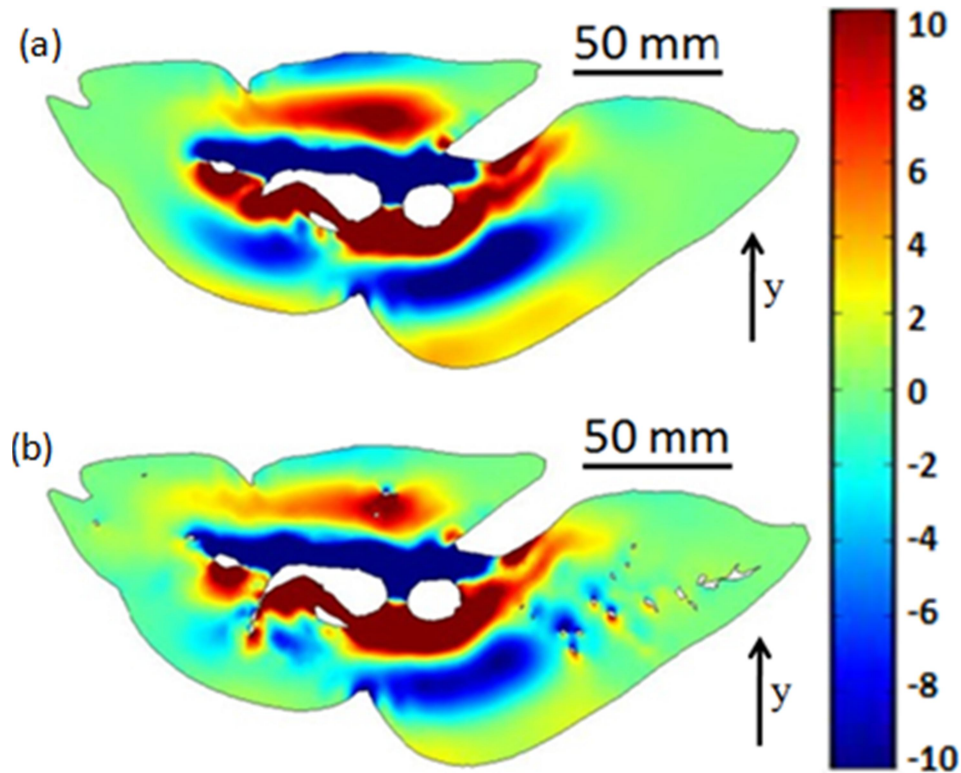
Figure 3.21 Cross-section Images of the real part of the lung velocity in the anterior-posterior direction (see arrow) in $\mu m/s$ at 800 Hz: (a) airway #1 (b) airway #2.

Table 3.3 Compression wave length (mm) estimation from simulation compared to Biot theory.

|  | 300Hz | 500Hz | 800Hz |
| --- | --- | --- | --- |
| Biot theory | 90.7 | 61.3 | 42.8 |
| Simulation, airway #1 | 82 | 60 | 38 |
| Simulation, airway #2 | 84 | 64 | 40 |

As shown in Figs. 3.17, 3.19 and 3.21, the shear wave is barely visible in our frequency range of interest. It appears that airway insonification mainly induces compression

waves in the lung. Diffuse lung fibrosis causes small changes in compression wave speed in the lung compared to significant changes in shear wave speed. So the very small differences in compression wavelengths reflected in cross-section images of the real part of the lung velocity are too weak to show alterations of wave propagation caused by diffuse fibrosis. Shear wave motion was induced in the simulation model by applying a harmonic shear force to the lung surface of 1 mm amplitude over an area of about 6.5 x 4 cm as shown in Fig. 3.22. Cross-section images are shown in Figs. 3.23 and 3.24. Shear motion was applied in out-of-plane direction. As wave images are mainly used to highlight the changes caused by diffuse fibrosis and the airway details do not greatly affect the wave fields, only simulations on airway #1 are presented here. For both frequencies, the shear wave length for lung fibrosis increases due to the increased shear stiffness. Table 3.4 lists the shear wave length estimated from simulation, which easily differentiates the normal from the fibrotic lung.
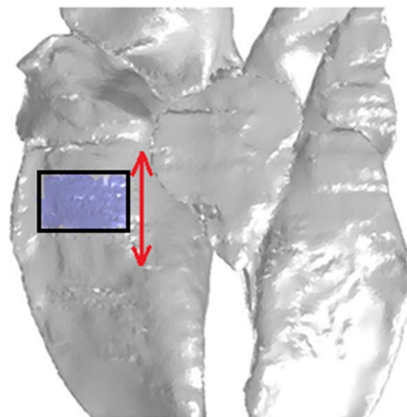


Figure 3.22 Shear motion applied to the lung surface.
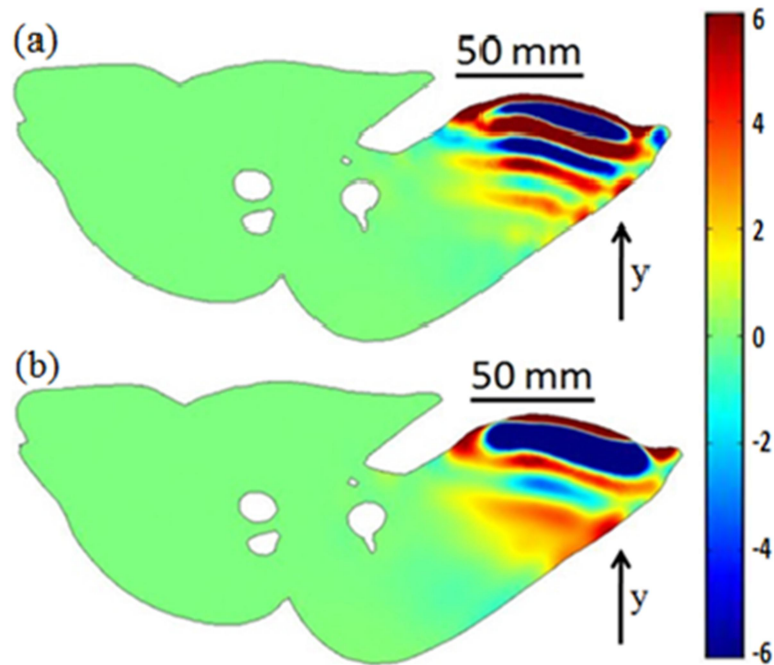
Figure 3.23 Cross-section Images of the real part of the lung velocity in the anterior-posterior direction (see arrow) in mm/s at 500 Hz: (a) normal lung, (b) fibrotic lung.
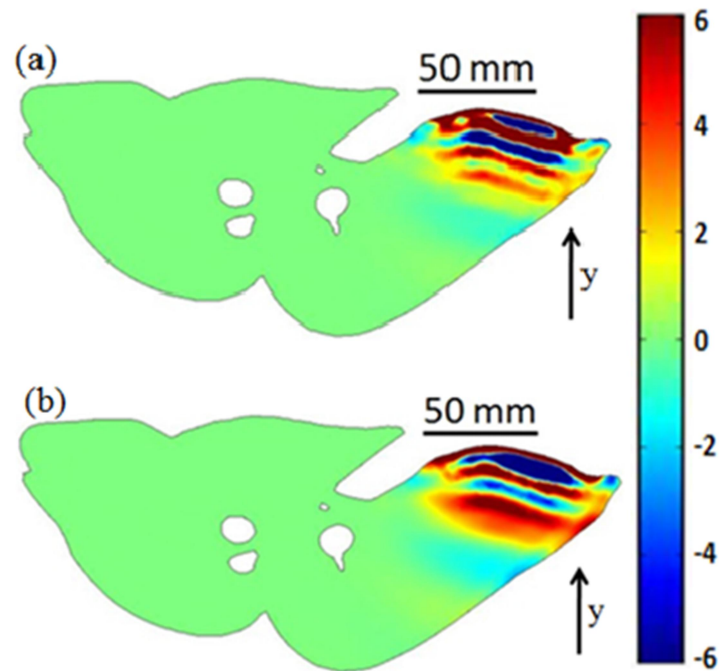


Figure 3.24 Cross-section Images of the real part of the lung velocity in the anterior-posterior direction (see arrow) in mm/s at 800 Hz: (a) normal lung, (b) fibrotic lung.

Table 3.4 Normal and fibrotic lung shear wavelength (mm) from simulation.

|          | 500Hz | 800Hz |
|----------|-------|-------|
| Normal   | 14.01 | 10.39 |
| Fibrotic | 17.88 | 12.69 |

Fig. 3.25 shows the cross-section images of the real part of the velocity at 500 and 800 Hz for the lung with tumor. Compared with Figs. 3.19 and 3.21, the compression wave length at each frequency remains almost the same while the wave fields are distorted by the tumors. Due to the impedance mismatch between the tumors and surrounding lung parenchyma, part of the tumor boundary where it is close to the main stem-bronchi is clearly visible.
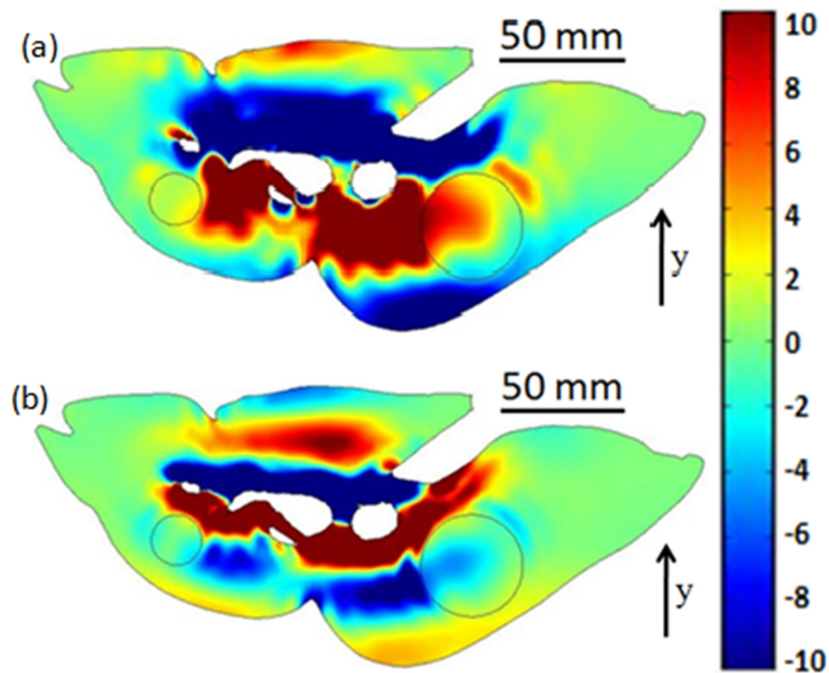


Figure 3.25 Cross-section Images the real part of the velocity in the anterior- posterior direction for the lung with tumor in $\mu m/s$: (a) 500 Hz, (b) 800 Hz.

It is acknowledged that the excised preserved lung will have differences from the in vivo case that may have an effect on its acoustic characteristics. Based on studies of others and of ours in vivo or in situ immediately upon sacrifice, we do not believe these effects are large, at least at the acoustic macroscopic scale.

## 3.6    Conclusions

A comprehensive computational simulation model of sound transmission through a porcine excised lung is presented and experimentally evaluated. Parenchymal and major airway geometry of this "subject-specific" model was created from x-ray CT images. The vibroacoustic response of the lung to sound input at the trachea is simulated in COMSOL finite element (FE) software. The lung parenchyma is modeled as a poroviscoelastic material using Biot theory. Acoustic impedances were applied to the airway terminal segments to represent the downstream un-modeled airway segments. The FE simulations were validated by comparisons with experimental measurements obtained using scanning laser Doppler vibrometry on the surface of an excised, preserved lung. Two levels of airway detail were used in the FE simulations and the model with fewer airway segments was closer to experimental measurements. The FE model was also used to visualize vibroacoustic pressure and motion inside the lung and its airways caused by the acoustic input. Effects of diffuse lung fibrosis and localized tumors on the lung acoustic response were visualized from FE simulations. This type of visualization could potentially be compared and matched with images from elastography measurements to better quantify lung material properties, such as stiffness.

CHAPTER 4

## 4. SOUND TRANSMISSION IN PORCINE AND HUMAN THORAX CAUSED BY AIRWAY INSONIFICATION

### 4.1    Introduction

#### 4.1.1    Motivation

Lung acoustic properties may be altered by various disease or injury states including fibrosis, congestion, consolidation, neoplasm, trauma, and pneumothorax (PTX).  These conditions often lead to structural and functional changes of the pulmonary system and measurable variations in sound transmission detectable over the chest surface during auscultation.  The presence of air within the lungs limits the utility of some imaging modalities.  For example, ultrasound has limited utility in imaging lung structures due to the acoustic impedance mismatch between the soft tissue and air within the lungs. Conventional magnetic resonance imaging (MRI) suffers from poor signal-to-noise-ratio (SNR) due to the lack of hydrogen found in air as compared to water.  X-ray computed tomography (CT) provides limited contrast for soft biological tissues and also introduces potentially harmful ionizing radiation.  Due to these limitations, a preliminary study that utilizes noninvasive measurement of external mechanical wave motion (sound and vibration) for lung injuries was performed in dog and porcine subjects [57, 75].  The study suggested that this method may provide information about lung mechanical property changes, which may have diagnostic value.

With the fast and continuous development of computational hardware, applications, simulation methods as well as advances in diagnostic imaging methods, new tools have become available.  These tools may allow better evaluation, interpretation and

quantification of pathological conditions and their response to treatment. From the early 1990s, the "Visible Human Project (VHP)" [109] has been made available through the U.S National Library of Medicine. That project is a free digital database of cross-sectional images of the human body acquired via multiple modalities. J Marescaux et al. [59] utilized this database to create a virtual reality (VR) simulation of hepatic surgery. He forecasted that surgical procedures, training, and teaching in a virtual reality environment would become feasible and more important.  Heng et al. [34] investigated VR simulation for knee arthroscopic surgery using a hardware system integrated with virtual reality technology.  Delingette et al. [19] introduced a virtual surgical training system utilizing 3-D models of liver, brain and heart generated from the VHP.

The ability to build realistic three dimensional (3D) models has been very useful for various computational simulations, including mechanics [67, 68], electromagnetics [83], and pathology [73].  However, challenges still exist especially in having accurate biological material property data for the computational models and validating the models for more general applications.  An experimentally validated acoustic computational model could aid in enhancing our understanding of sound transmission in the chest. Recently, a diagnostic technique for measuring tissue stiffness based on MRI technique called magnetic resonance elastography (MRE) has been applied to the lungs in research studies with some conditional success [28, 60].  This technique is able to provide a map of the viscoelastic properties within the region of interest (ROI).  These maps may correlate with injuries, the progression of diseases and/or the response to therapy.  Validated computational models would help predict transmission patterns of

the mechanical waves used in MRE, which may help interpret and understand MRE images.

### 4.1.2   Measurements of sound transmission in lung and thorax

Mechanical compression waves (sound) travel in the lung parenchyma much more slowly than in the air and soft tissue of which it is comprised.  Sound speeds in the human lung [4, 47, 48, 54, 71] and animal lung [40, 41, 77, 106] have been studied.  In human studies, sound was usually introduced into the mouth.  In animal studies, sound was usually applied and measured at the lung surface.  All these animal studies concluded that the sound speed depended on the lung volume, which is known to change throughout the respiratory cycle.  That volume change leads to an alteration of lung density and air volume fraction in the lung, which affects the sound speed.  This is consistent with theoretical models [77].

In order to acquire the response of the thorax, some previous investigations focused on the transmission of sound introduced from the mouth then to measurements on the chest surface.  For the circumstance, properties of the system which are in either static or even dynamic conditions are able to be measured and compared by the model predictions and other hypotheses.  The amplitude and phase delay of transmission can be found by the FRF of the chest surface response and a reference.  The reference can be measurement of the extrathoracic trachea or other measurable approaches.  Amplitude of frequency-dependent matches the substance of the accounting parenchymal losses of the thorax model [96, 101].  Kraman et al [47, 49] proposed an approach for measuring sound transmission from the mouth to the chest wall and the approach was also studied by Wodicka et al [103] and Pasterkamp et al [74]. The

reports from their study indicated that the amplitude at the right lung site was significantly greater than the one at the left lung site in the low frequency range. In addition, the findings also suggested that the changes in lung structure caused by disease were able to affect the amplitude and speed of the sound transmitted from the airways then propagated to the chest surface. Böhme et al [9] reported that a decrease of transmitted amplitude at low frequencies In patients with emphysema and Mansy et al confirmed the similar finding in dogs with pneumothorax [57] later in the study. Differently, it was reported [20] that cardiogenic pulmonary edema could cause increasing amplitude of sound transmitted to the chest wall in dog and the consolidated lung.

### 4.1.3  Poroviscoelastic modeling of lung.

In 1956, Biot developed a theory [5, 6] for the stress wave propagation in a porous elastic solid containing compressible viscous fluid, which predicts the existence of two types of compression waves in fluid-saturated porous media. This theory has been widely used in many geophysical applications and extended to poroviscoelastic medium. There have already been numerous studies on poroelastic and poroviscoelastic modeling of soft tissues. Mow et al. [64] first applied the biphasic theory to the articular cartilage which is a biphasic material composed of the solid matrix and interstitial fluid. Simon et al. [87, 88] proposed multiphase poroelastic finite element models for soft tissue structures and extended the model including transport and swelling in the tissue. Currently there have been limited studies on poroviscoelasticity modeling of lung acoustics. Siklosi et al. [86] modeled the lung parenchyma as a porous solid with air-filled pores by Biot theory as a model for its compression wave speed. Dai et al. [16]

compared Biot theory of wave propagation in poroviscoelastic media and an "effective medium" theory based on a closed cell assumption to model sound transmission in the lung parenchyma. In that study, compression wave speed and attenuation in freshly excised pig lung agreed pretty well with predictions from the theory which were based on Biot theory significantly more closely than the effective medium theory.

### 4.1.4 Chest wall material properties.

To quantify material properties of soft biological tissue in the human body, Von Gierke et al. [26] carried out experiments on the human thigh and upper arm, in which the skin surface was excited by a vibrating piston with different frequencies and propagation of surface waves was measured using stroboscopy. The soft tissue was considered as a viscoelastic medium and the viscous and elastic material parameter values were estimated based on experimental measurements. Garner et al. [25] studied human bone viscoelastic properties over a wide range of frequencies. Experiments were conducted by using torsional and bending methods, which were previously used by Lakes et al. [51], on human dry and wet compact bone to investigate their material properties, especially Young's modulus and shear modulus. According to these studies, the bone material properties were found to be frequency-dependent due to bone viscoelasticity.

### 4.1.5 Objectives of this study.

The main objective of this study is to develop and experimentally validate a comprehensive computational acoustic model that simulates sound propagation in the airways, lungs, and chest wall, and how propagation is changed under the pathological condition of pneumothorax (PTX). Experimental measurements and methods of

generating a 3-D computational model are described in Sec. 4.2. The lung region is modeled as a poroviscoelastic material based on Biot theory. A finite element (FE) model of the pig chest that includes the underlying organ details is constructed and used in FE software package to simulate the vibroacoustic response of the chest surface caused by the sound input at the trachea. In Sec. 4.3 and 4.4 the results of pigs and human from the FE simulation are compared with experimental measurements for cases of normal and PTX states. A discussion of the results is provided in Sec. 4.5, followed by conclusions in Sec. 4.6.

## 4.2    Materials And Methods

### 4.2.1  Experimental porcine studies
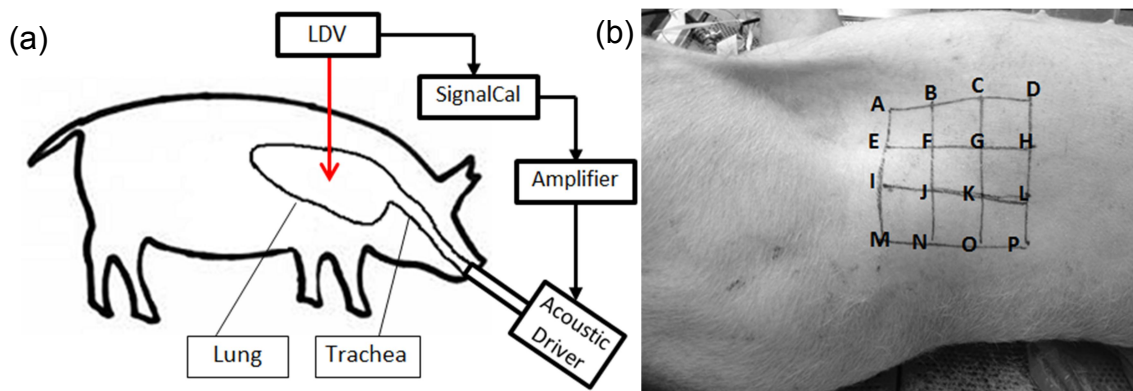


Figure 4.1 (a) Experimental setup for porcine subject. (b) The location of array of measuring points.

Experiments were conducted on five freshly sacrificed female Landrace and Yorkshire cross pig subjects (weights 30-35 kg) after getting approval of the institutional animal care and use committee (IACUC). The experimental setup is shown in Fig. 4.1(a). Immediately after the pig was euthanized, it was secured in the left lateral decubitus

position (right-side-up) with the skin hair of the measurement area shaved completely. In addition, the pig lungs were kept inflated with air at an airway pressure of 5 cm $H_2O$ through an endotracheal tube. The anatomy of the pig indicated that its lungs are located roughly between the first and tenth rib. During the experiment, the airway pressure was adjusted to 20 cm $H_2O$ to help fully open the airways inside the lung. A laser Doppler vibrometer (LDV) (PDV-100, Polytec, Irvine, CA) was used to measure the velocity of the skin surface at 16 evenly spaced points in an array located in the area from the fifth rib to the ninth rib (Fig. 4.1(b)). In order to enhance the laser reflectivity for improved signal-to-noise ratio, P-RETRO-250 glass beads (45 – 63 µm dia., Polytec, Irvine, CA) were applied to the skin surface of subjects. A broadband periodic chirp signal with spectral content from 50 – 800 Hz was generated from a dynamic signal analyzer (SignalCalc ACE, Data Physics, San Jose, CA) and fed to an amplifier (P 3500S, Yamaha, Buena Park, CA) to drive a 3.5 inch speaker (PDWR30W, PylePro, Brooklyn, NY). The sound wave generated from the speaker was sent into the pig lung through the endotracheal tube. As the sound pressure generated by the speaker is frequency dependent, a 1/4 inch microphone (378C01, PCB Piezotronics, Depew, NY) was inserted into a drill hole in the proximal endotracheal tube. This measured pressure was used for the FE simulation as the acoustic pressure input described in Sec. 4.2.4.

The above measurements were performed for the normal and pneumothorax (PTX) states for each animal. The PTX state was purposefully created by making a small incision in the seventh intercostal space in the right mid-clavicular line, which allowed air to enter into the plural space. The airway pressure was set to "0" in the PTX state to

allow for full lung collapse. A 5 mm thoracoscopic trocar (Endopath Dilating Tip, model 355, Ethicon, Cincinnati, OH) was inserted into the chest and an endoscope was used to visually confirm the PTX state.

### 4.2.2 Experimental Studies of Normal Human Subjects
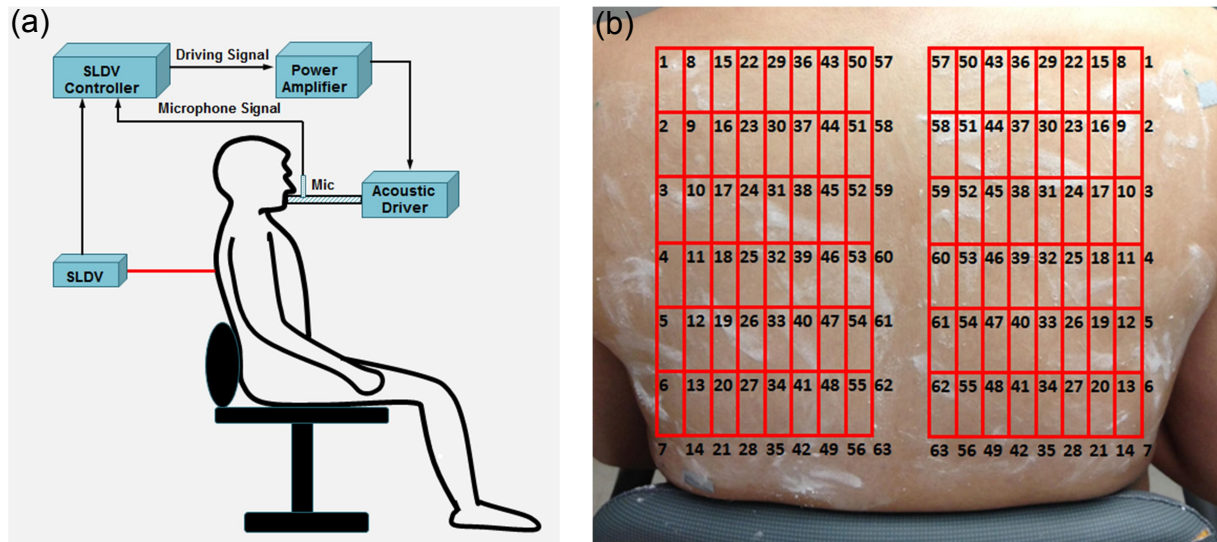


Figure 4.2 (a) Schematic diagram of the experimental setup on human subject. (b) The location of array of measuring points.

Experimental studies were carried out on three healthy human subjects (HS) after receiving appropriate Institutional Review Board (IRB) approval. Figure 4.2 (a) is showing a schematic diagram of the experimental setup. In the experiment, the HS with no known pulmonary pathologies was sitting on a chair. In order to improve the signal to noise ratio (SNR), the HS was requested to sit still and hold their breath during the measuring process (short time, around 20 seconds per measurement). Retro reflective glass beads (nominal diameter = 45 – 63 μm) were applied on the measured region (Figure 4.2(b)) which was the skin surface of the back of the subject, to increase the reflection for a scanning laser Doppler vibrometer (SLDV) (PSV-400, Polytec, Irvine,

CA).  A tube was kept in the mouth of the HS through which sound came from a 3.5 inch speaker (PDWR30W, PylePro, Brooklyn, NY) and was guided to the mouth and transmitted into the airways.  A 1/4 inch microphone (377A01, PCB Piezotronic, Depew, NY) measuring the sound pressure was mounted at the outlet of the tube close to the month of the HS as a reference for the SLDV.  The speaker was connected to a power amplifier (P 3500S, Yamaha, Buena Park, CA) and driven by a periodic chirp signal with spectral content from 50 – 600 Hz; this excitation source was generated by the SLDV system.  There were 63 scanning points (Figure 4.2(b)) on each side of the back (total of 126 scan points for the entire back).

The array data of the scanning locations was then processed by the SLDV acquisition system to determine the frequency response function (FRF) at each measuring point. To ensure that the FRF has a high SNR in the frequency range of interest, the coherence between the signal measured by the SLDV and the reference signal is calculated as a measure of the SNR with respect to the reference.  The definition of the FRF for each scanning point can be found in Peng et al. [75].

### 4.2.3  Material property measurement of pig muscle tissue

Because investigations of the compression wave properties of porcine muscle tissue are sparse, an experiment was implemented on a piece of pig muscle tissue obtained from the posterior chest of a pig in order to measure the compression wave speed and the attenuation in the pig muscle tissue.  The schematic diagram of the experimental setup is shown in Fig. 4.3.
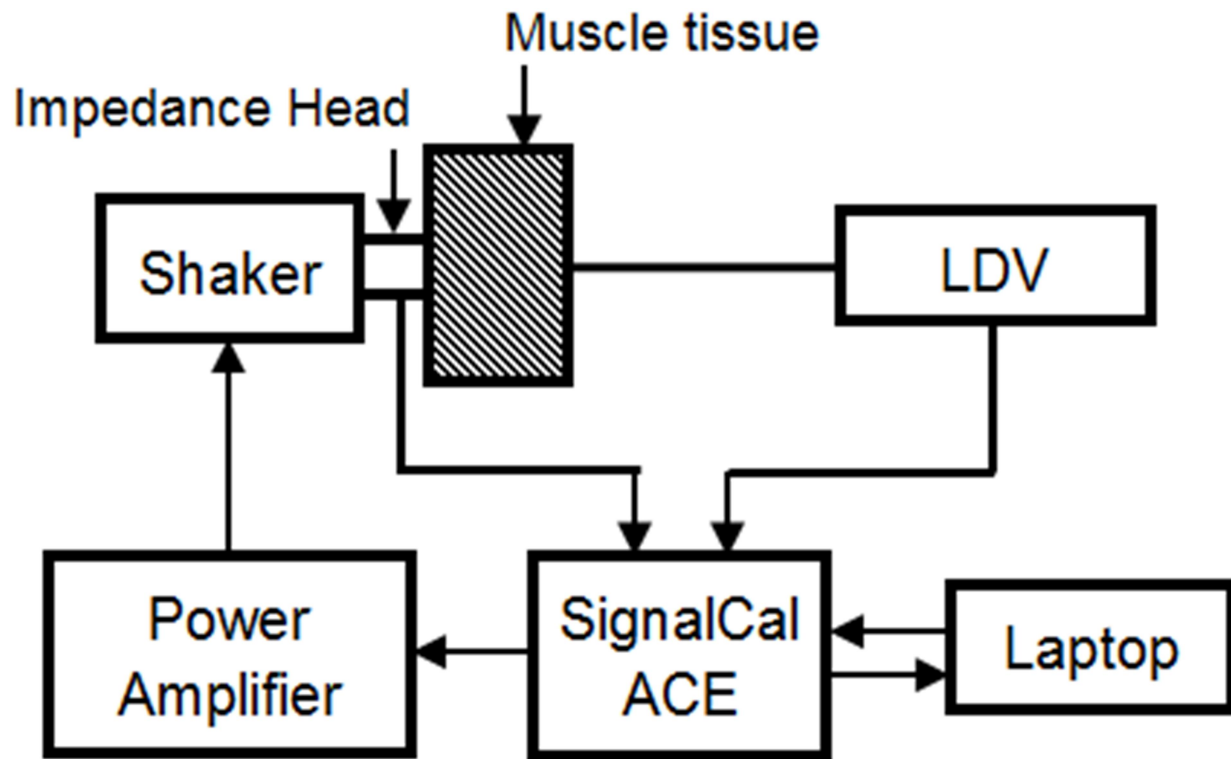
Figure 4.3 Schematic of experimental setup.

A sinusoidal chirp signal containing frequencies from 50 to 4000 Hz was generated from a dynamic signal analyzer (SignalCalc ACE, Data Physics, San Jose, CA) and was fed into a power amplifier (P 3500S, Yamaha, Buena Park, CA) that was connected to an electromagnetic shaker (ET-132, Lab-Works Inc., Mesa Costa, CA). An impedance head (288D01, PCB Piezotronics, Depew, NY) was mounted on the shaker and was placed in contact with the muscle tissue to measure the input acceleration signal to the tissue sample. The sample thickness was L = 5.8 cm and contact area with the input from the shaker was circular with a diameter of 2 cm. The out-of-plane velocity of on the other side of sample was measured by a laser Doppler vibrometer (LDV) (PDV-100, Polytec, Irvine, CA). The acceleration and velocity measurements were recorded by the same signal analyzer with a sampling frequency of 102.4 kHz and data was stored in a

laptop computer.  The input acceleration signal measured by the impedance head was denoted by x(t).  The output acceleration signal y(t) was the derivative (with respect to time) of the velocity measured by the LDV.  Consequently, the compression wave speed can be calculated from the phase angle $\theta_{xy}$ of the cross-spectral density function between x(t) and y(t).  The transit time $\tau$ can be calculated from the slope of the $\theta_{xy}$ frequency curve by

$$\tau = -\frac{1}{2\pi}\frac{d\theta_{xy}}{df}$$ (4.1)

For a linear viscoelastic material, the complex-valued compression wave number $k_p$ is given by

$$k_p = k_{pR} + jk_{pI} = \frac{\omega}{c_p}$$ (4.2a)

Here, $c_p$ is the complex-valued compression wave speed.  $\omega$ is the angular frequency. The real part of the compression wave number $k_{pR}$ is related to the phase speed $c_{ph}$ (calculated by dividing the thickness, L, by the transit time, $\tau$ ) [18] by

$$k_{pR} = \frac{\omega}{c_{ph}}$$ (4.2b)

The attenuation of the compression wave is governed by the imaginary part of the wave number $k_{pI}$ [18].  To estimate the attenuation of the compression wave in the tissue, a continuous sinusoidal input with a single frequency was used.   That signal was generated from the dynamic signal analyzer, sent to the amplifier and delivered into the sample by the shaker.  The input acceleration $a_1$ was measured by the impedance head

and the output acceleration $a_2$ was derived from the velocity measured by LDV. The experiment was repeated for different frequencies in from 50 to 1000 Hz. Assuming planar compression wave, the input and output accelerations ($a_1$ and $a_2$, respectively) can be expressed by:

$$a_1 = A_0 \cdot e^{j(k_p x_1 - wt)} = A_0 \cdot e^{-k_{pI} x_1} \cdot e^{j(k_{pR} x_1 - wt)} \tag{4.3}$$

$$a_2 = A_0 \cdot e^{j(k_p x_2 - wt)} = A_0 \cdot e^{-k_{pI} x_2} \cdot e^{j(k_{pR} x_2 - wt)} \tag{4.4}$$

Where $A_0$ is the amplitude of acceleration. Then

$$\left| \frac{a_2}{a_1} \right| = e^{-k_{pI}(x_2 - x_1)} = e^{-k_{pI} L} \tag{4.5}$$

$$k_{pI} = -\ln\left( \left| \frac{a_2}{a_1} \right| \right) / L \tag{4.6}$$

After evaluating $k_{pR}$ and $k_{pI}$, the complex compression wave speed is determined from Eq. (4.2a). Experimentally determined values of these material properties will be used in the following section(s).

### 4.2.4  Computational simulations

### 4.2.3.1     Three dimensional geometry model construction of the pig

To generate the 3D porcine geometries for computational studies, comprehensive geometrical details of the torso structures were constructed from CT images obtained from scans with 1 mm slice steps and pixel matrix size 512x512 (Brilliance 64, Philips Electronics). The pig used for scanning was similar in size (weighted 34 Kg) to those studied in the acoustic experiments described in Sec. 4.2.1. CT image sets were imported and processed using Mimics V14 (Materialise, Plymouth, MI), which is a

biomedical image processing software for the segmentation of 3D models. Different density of the contrast regions (lungs, bone regions, and muscle tissue regions) can be distinguished in the software to assign layers at each slice of the CT images. Then all of the 2D layers can be combined to create a 3D model for each part. The 3D models for torso, ribcage, scapulae and lungs are shown in Fig. 4.4 (a).
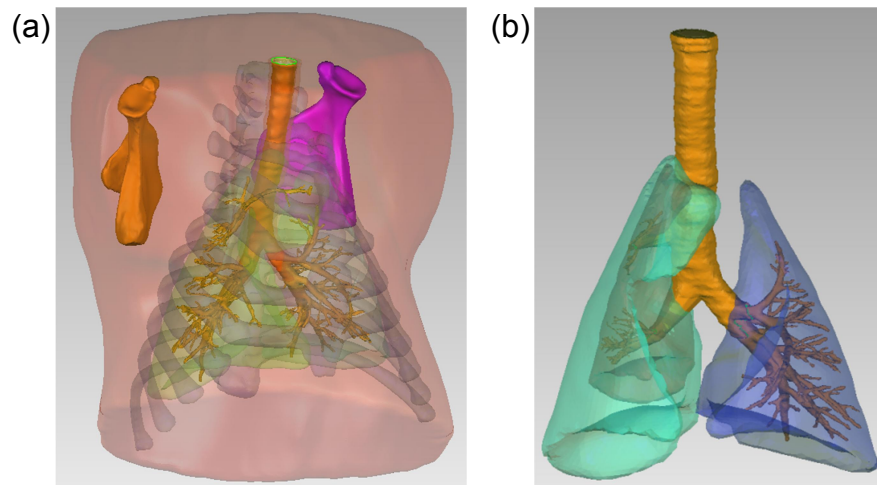


Figure 4.4 (a) 3-D model of porcine upper torso and internal organs. (b) 3-D model of porcine PTX lung and airways.

To build the 3D model of airways inside the lung, an open source medical image segmentation software ITK-SNAP Version 2.4 [108] was used to construct the geometry of the different chest structures. CT images were imported for automatic segmentation using the Snake Algorithm in ITK-SNAP [108]. The automatic segmentation was used as a first step in generating the geometry, which can later be improved manually. Due to the contrast resolution quality of the CT image sets, there were twenty airway segments created by the automatic segmentation method; the quality of the segmentation is largely dependent on the quality of the images. Because of the

complexity and small size of the distal branches of the airways, these airways were completed manually by marking contrasted regions slice by slice. This was achieved by creating the airway segments with the marker tool in the local contrasted regions. By combining the above automatic and manual approaches a more intricate airway tree with around 100 segments was constructed.

The mainstem bronchi and trachea were the starting point of the Snake Algorithm[108], and were the first to be automatically segmented. With the completion of all the segmentations, a surface tessellation algorithm was applied by ITK-SNAP for capturing the 3D geometrical data and this data was exported as a stereolithography (STL) CAD file so that it could be meshed properly in ANSYS ICEM CFD.

Once the airways and trachea geometries were imported to ANSYS ICEM CFD 12.1 (Ansys Inc, Canonsburg, PA), a meshing tool in ANSYS, they were combined with the files containing the geometries of the torso, lungs, ribcage and scapulae built in Mimics V14. The geometries were checked in ANSYS for mesh quality and intersecting errors. Once the geometry passed that test, it was volume meshed to create a FE model. In addition, the surface of the trachea and mainstem bronchi was extruded in the radial direction to construct the thickness of the airways, creating two volumes for the airways: one for the air, and another for the thickness of the mainstem bronchi and trachea walls. To generate a 3D model of PTX, the right lung was rescaled by a factor of 71% in volume (PTX = 95%) and fit inside of the original right lung volume, while keeping the rest of the 3D models the same except that the remaining volume inside the chest cavity was assumed to be filled with the PTX air. The PTX percentage is defined by the ratio of volume of PTX air and the volume of the inflated normal lungs

**4.2.3.2    Three dimensional geometrical construction of human**
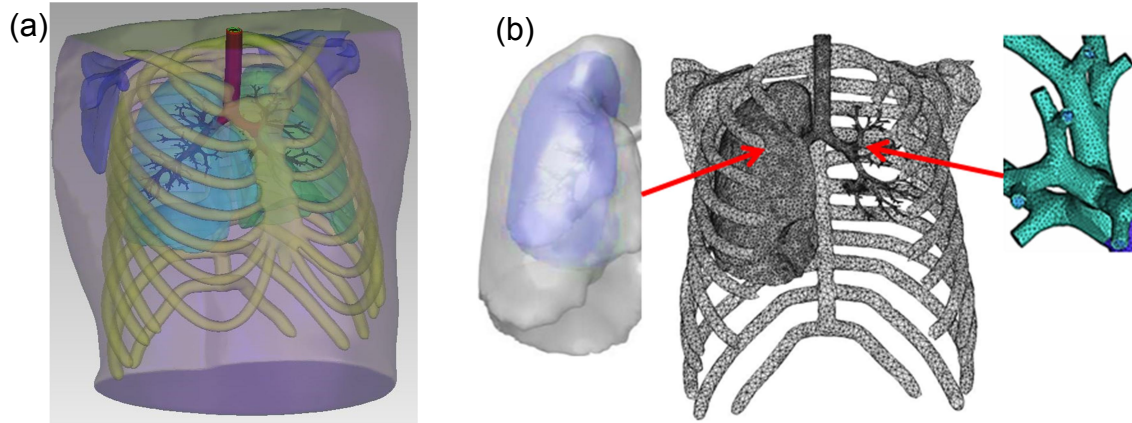


Figure 4.5 (a) 3-D model of human upper torso and internal organs.  (b) 3-D meshed model of human PTX lung and airways coupled.

In order to simulate the experimental process described in the previous sections, a comprehensive human 3D model is needed.  In this study, the human geometry without airways was first constructed from the CT images of a male human subject from the Visible Human Project (VHP) [109] of the National Library of Medicine (NLM) and is shown in Figure 4.5 (a).  To construct the 3D geometries from the CT images, the CT image sets were imported and processed using Mimics V14 (Materialise, Plymouth, MI), which is a commercial image processing and 3D modeling software. The created 3-D model contains the geometries of torso, lungs, ribcage, cartilage, and scapulae.  The dimensions of the human model were rescaled to appreciate the average size of the tested human subjects in the experimental study.

For simulating sound propagating in the airways coupled with the lungs and other organs, a 3D model of airways needs to be integrated with the lung models.  In the previous study, Dai et al, and Peng et al. [18, 75] proposed an approach of creating airways by using the original CT or MRI images to generate 3D models.  In this study, a

computer automatically generated 3-D airways by using a method proposed by Kitaoka et al. [44] that follows hard-coded mathematical laws and conditions. Figure 4.5(b) shows the computer generated airways coupled with other organs.

After the 3-D model of the airways was created, the following steps are the same as the ones done for the porcine 3D models. To simulate the pathological case when the lung is collapsed (PTX), the 3D model of the right lung was shrunk 70% in volume which corresponds to a PTX = 90% and fits inside of the original lung cavity while the models of other organs parts were kept the same. The corresponding model of the airways in the right lung were also rescaled with same shrinking rate and fit into the shrunk right lung to approximate the PTX case (Figure 4.5(b)).

### 4.2.3.3 Material properties of lung parenchyma

Sound propagation into the lungs and transmission to the chest surface was modeled in a FE environment COMSOL Multiphysics® 4.3b (COMSOL Inc, Burlington, MA) using the acoustic-solid interaction module for frequency domain analysis. The entire volume mesh of the relevant parts, such as chest wall (soft tissue), lungs, trachea, ribcage, scapulae and airways mentioned above were imported into COMSOL for simulation.

Material properties of each organ needed to be provided to the modeling software before running the simulation. For the lung parenchyma, previous studies and the Sec. 2.2 demonstrated that Biot theory of wave propagation in poroviscoelastic media [5, 6] was a more accurate model than the previously-used effective medium theory [18] to model sound transmission in the lung parenchyma (Eq. 2.1-2.4). In our frequency range of interest (for porcine from 50 to 700 Hz, for human from 50 to 600Hz), the slow

compression wave can't propagate as the relative motion between the lung parenchyma and air is impeded by viscous drag [10]. Note that, only the fast compression wave propagation may be detectable in the lung parenchyma in the current study. The information of material properties calculated from would be input into COMSOL to perform the simulations.

Taking the porcine model for instance, Fig. 4.4 (a) shows the chest structure under normal conditions. When the PTX is introduced in the right chest, the right lung collapses and thus will have a lower air volume fraction depending on the level of collapse. In this case, the chest region in the 3D model that was originally occupied by the right lung was split into two portions, the collapsed parenchymal region and the air outside the lung (Fig. 4.4 (b)). For the current simulation, the 3D model was made to create a large PTX state with $\phi = 11\%$. This value of air volume fraction is corresponding to a PTX ~= 95%, which presents the extreme state of PTX similar to that induced in the experiment. The lung compression wave speed, shear wave speed and attenuation were then calculated using Eq. (2.3) for this air volume friction. For the human model, the information has been provided in the previous Sec 4.2.3.2.

### 4.2.3.4    Airway acoustics in pig and human lungs

For the porcine and human 3D geometric model, the distal airway segments are un-modeled because of the limit of the resolution of the CT image. However, the terminal impedance (ratio of acoustic pressure to acoustic particle velocity as a function of frequency) of the terminal segments needs to be calculated to represent the downstream airways that are un-modeled. A structural model (called the Horsfield model) was utilized to perform the needed impedance calculations [36, 37]. That model

can be applied to most mammalian airway trees and including that of the pig which appears to have a morphology that is close to the human airway tree, especially the segments with small diameters. Hence, in these calculations the structural parameters of the human airway are used to calculate the pig airway terminal impedance. The corresponding terminal impedances for the human airways were also calculated using the Horsfield model. The theory of Horsfield model was explained in Sec. 3.2.1.

To calculate the impedance for the terminal airways, an order number needs to be specified for the terminal segments of the pig airways. The standard deviation of the terminal segment diameter is small such that the terminal segments are regarded as the same and their order number is found by relating their mean diameter to the closest value in Table 9-2 in Royston et al. [82]. For the normal airway of the current model, the terminal segment mean diameter is 0.1568 cm, which corresponds to the airway order number 14. For the PTX state, the lung is collapsed and this causes a decrease in airway diameters. Note, the Young's modulus of the bronchioles are about 20 times larger than that of the surrounding lung parenchyma, and the larger airways are stiffer due to the airway cartilage. The effect of surrounding lung parenchyma on airway diameter decrease is very small and is neglected for estimation of airway diameters of the collapsed lung. Assuming the airway segment as a thin-walled elastic tube (airway viscoelasticity doesn't affect airway segment diameter under steady state conditions), the relationship between airway radius and transpulmonary pressure is [24]

$$da^{(n)} = \frac{\alpha^{(n)}}{2} dp \qquad (4.7)$$

where $da^{(n)}$ is the change of radius of airway segment with order $n$. $dp$ is the transpulmonary pressure change. And

$$\frac{\alpha^{(n)}}{2} = \frac{\left(a^{(n)}\right)^2}{E^{(n)}h^{(n)}}$$

(4.8)

Here $a^{(n)}$, $h^{(n)}$ and $E^{(n)}$ are the radius, wall thickness and Young's modulus of the airway segment with order n; $E^{(n)}$ is calculated from airway cartilage Young's modulus $E_c$ and airway soft tissue Young's modulus $E_s$ by

$$E^{(n)} = c^{(n)}E_c + (1-c^{(n)})E_s$$

(4.9)

From studies by Suki et al. [92], $E_c$ and $E_s$ are taken to be 392 kPa and 58.1 kPa respectively. $c^{(n)}$ is cartilage percentage of airway segment with order number n and it is listed in in Table 9-2 in Royston et al. [82]. $dp$ is -20 cm $H_2O$ from normal to PTX state. From Eq. (4.7), for airway segments with order number from *n*=15 to *n*=27, the segment diameter decreases at an average ratio of 32% and this ratio is close to but only a bit larger than experimental studies on airway diameters under different transpulmonary pressure in dogs [94]. Diameters of trachea, main stem bronchi and lobar segments have much smaller decreases due to their high cartilage content. Finally, the acoustic impedance of the terminal airway segment in the PTX state was calculated for the decreased airway segment diameters.

**4.2.3.5    Material properties of muscle tissue and bone**

The values of material properties of muscle tissue were based on previous studies [26, 79, 81].    According to their studies, the soft muscle tissue was considered as

viscoelastic media and the Voigt model of viscoelasticity was used. So, the shear modulus can be expressed as:

$$\mu_t = \mu_{t1} + j\omega\mu_{t2} \tag{4.10}$$

Here the subscript "t" denotes the soft tissue. $\mu_{t1}$, and $\mu_{t2}$ denote shear elasticity and shear viscosity, respectively. $\mu_{t1} = 2.5 \times 10^3$ Pa and $\mu_{t2} = 15$ $Pa \cdot s$ [26, 79]. With the reported soft tissue density of 1100 kg/m³, the complex shear wave speed can be calculated by using the Eq. 2.2a in Sec. 2.2.1. With the compression wave speed and attenuation of muscle tissue measured in the Sec. 4.2, the muscle tissue mechanical properties can be completely defined in the simulation.

The complex young's modulus of the bone can be represented by $E = E_{b1} + j \cdot E_{b2}$ with $\tan\delta_E = E_{b2} / E_{b1}$ [14, 25] and subscript "b" denotes the bone. The values of the loss tangent $\tan\delta_E$ is frequency dependent and was experimentally measured by Garner et al. [25]. For the current frequency range of interest, the real part of $E$ is taken to be $E_{b1} = 12.7$ GPa in the simulation [14]. The complex shear modulus is expressed as $\mu_b = \mu_{b1} + j\omega\mu_{b2}$ with $\tan\delta_\mu = \mu_{b2} / \mu_{b1}$. The shear loss tangent $\tan\delta_\mu$ was determined from previous experimental measurements [25, 51] and the real part of shear modulus is $\mu_{b1} = 3.15$ GPa [14].

In the COMSOL simulation, the normal lung region, collapsed lung region and air region were set as a "pressure acoustics model". The soft/muscle tissue and the bone were set as the "linear viscoelastic material model". A free boundary condition was applied on the torso surface while an "acoustic-structure boundary" was applied on the lung-

muscle tissue interface.  Acoustic excitation at the inlet of the trachea was applied in the simulation by using frequency dependent sound pressure measured in the experiment in Sec. 4.2.

## 4.3    Results of pig study

The results of pig study will be presented in this section.  In order to find the real part of the compression wave number, the phase speed is calculated from the phase angle ((Fig. 4.6(a)) of the cross-spectral density function described in Sec. 4.2. From the experimental measurement and Eq. (4.1) and (4.2), it is straightforward to get the value of the real part of wave number which is 1345.5 m/s; and this value was used in the simulation described in Sec. 2.3.2.

The experimental results of imaginary part of wave number are plotted in Fig. 4.5 (b). The measured data points were used to find the best curve fit expression for the current frequencies of interest.  That expression was used to determine the material properties for the simulation described in Sec. 2.3.2.
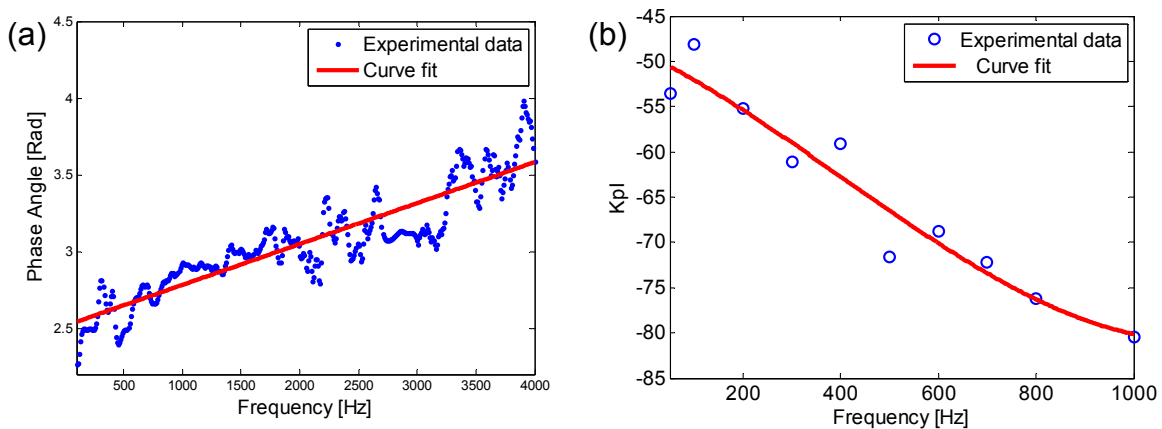


Figure 4.6 Experimental results and curve fitting of (a) the compression wave phase speed and (b) the imaginary part of wave number. "•": measured data points of phase speed. "o": measured data points of imaginary part of wave number;  "—": fitting curve.
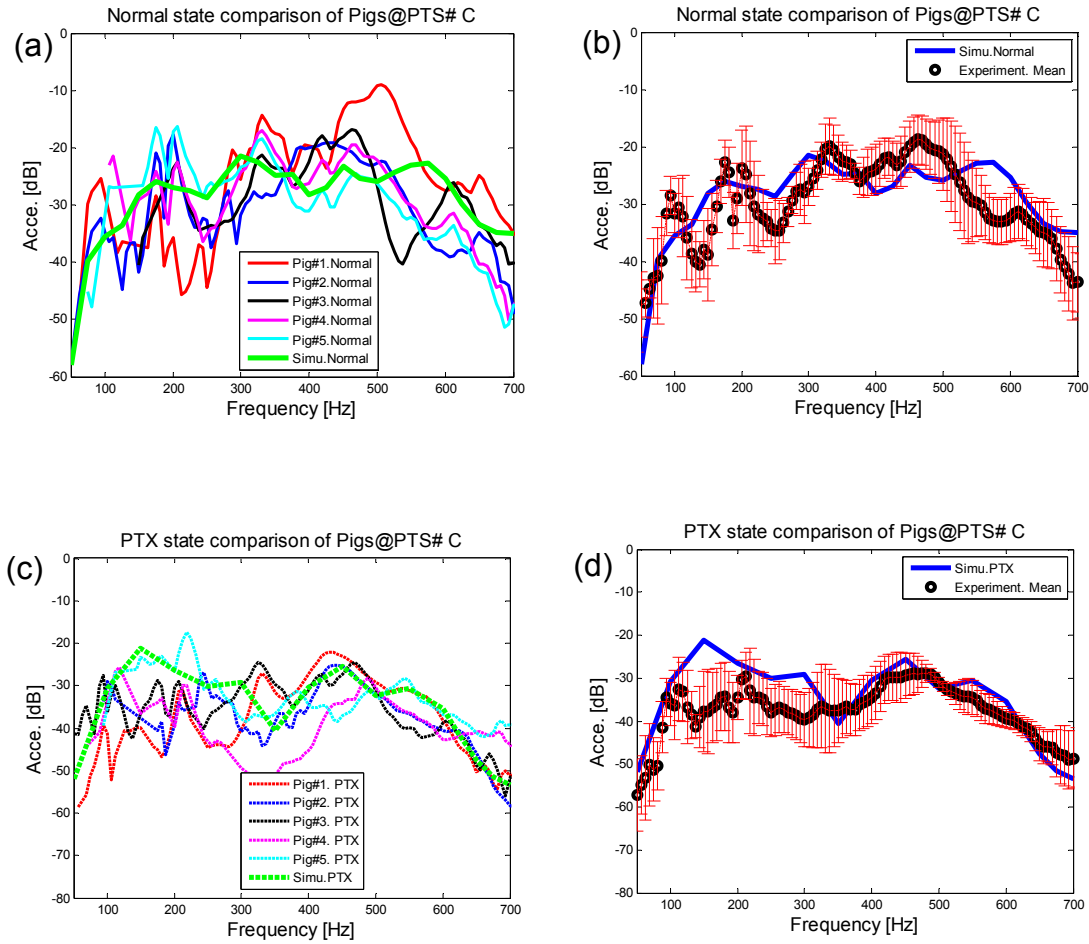
Figure 4.7 Acceleration on the chest surface for normal state at point C: (a) comparison of simulation and experiments on five pigs; (b) comparison of mean acceleration of experiment and simulation. The error bars indicate standard deviation of five pigs. Acceleration on the chest surface for PTX state at point C: (c) comparison of simulation and experimental acceleration of five pigs; (d) comparison of mean acceleration of experiment and simulation. The error bars indicate standard deviation. Units (m/s$^2$ in dB scale).

The acceleration amplitude of the normal and PTX states at point #C on chest surface (see Fig. 4.1(b) for point location) is shown in Fig. 4.7(a) and (c). Experimental results for all five pigs and simulation results are shown. The experimental acceleration was calculated from the velocity (measured by LDV). The experimental data are only

plotted at frequencies where the coherence (between input pressure and the measured velocity) exceeded 0.85. It can be seen in the figure that the variability in the measured values is noticeable for the normal and PTX states. Fig 4.7 (b) and (d) show the mean acceleration of five pigs for the normal and PTX state along with the simulation results. In these two figures, the simulation prediction is comparable with the experiment mean and similar trends can also be observed. The locations of spectral peaks are a little different between experiment and simulation, especially below 250 Hz. It can also be seen from Fig. 4.7 (b) and (d) that the standard deviation is smaller at frequencies larger than 250 Hz , which may be due to the higher signal to noise ratio (SNR) at the higher frequencies. The simulation predictions were compared with experimental results at other measurement locations and results were similar to those presented here.

In Fig. 4.8(a), experimental results of the normal state and PTX state are compared at a specific measurement point #C. The experimental data for normal and PTX are only plotted at frequencies where the coherence exceeded 0.85. It can be seen that the acceleration amplitudes of the PTX state are consistently lower than those of the normal state in the frequency range from around 250 to 700 Hz. In the frequencies from 50 to 250 Hz, the amplitude differences between the normal and PTX state appear smaller. In Fig. 4.8(b), the maximum change of amplitude between the normal and PTX states is about 20 dB. The average reduction over the frequency range of 250 Hz to 700 Hz for the five pig subjects is 9.92 dB with a standard deviation of 1.88 dB. Fig. 4.8 (c) shows the average energy for the normal and PTX state of experimental results of the five pig subjects and the results of simulation. It can be seen that in the frequency range under consideration, the average transmitted energy in the normal state is higher than that in

the PTX state for every subject. Comparison at other points also showed a drop in torso surface acceleration amplitude and average energy for the PTX state.
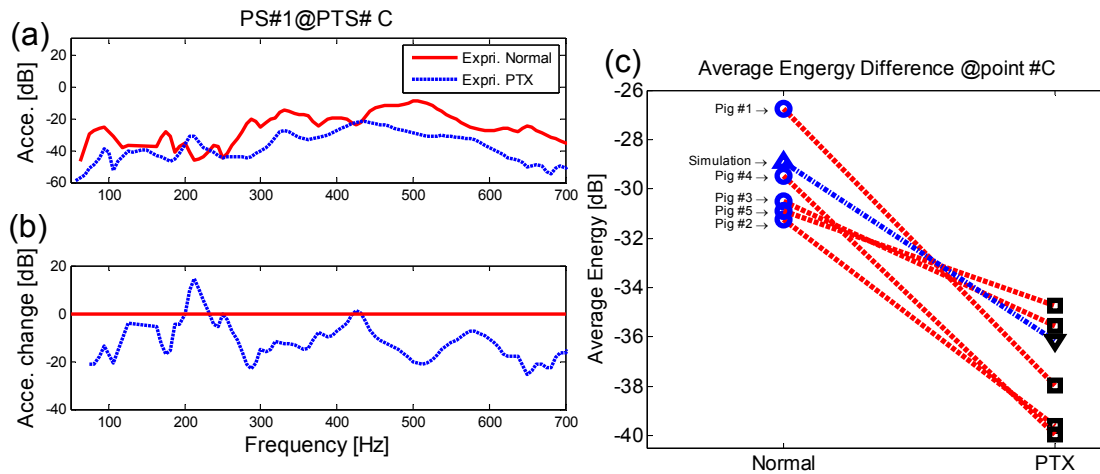


Figure 4.8 Experimental comparison of normal and PTX state. (a)The comparison of normal and PTX. (b) The acceleration amplitude change between PTX and normal states (Change=PTX-Normal). (c) Average measured energy of normal and PTX state at point #C for five pig subjects in the 50-700 Hz frequency band. Experimental result (Normal): o; Experimental result (PTX): □; Simulation result (Normal): "Δ"; Simulation results (PTX): "▽"; "---" connects the results of the same pig subject; "— - —" connects the results of simulation.

In Fig. 4.9 (a) and (b), simulation results of the normal state and PTX state are compared at surface measuring point #C. The results at other points are similar. Simulation results match experimental trends in that the acceleration amplitudes of the PTX state are lower than those of the normal state in the frequency range from 250 to 700 Hz. The average reduction predicted by the simulation over the frequency range from 250 Hz to 700 Hz for the presented points is 9.05 dB with a standard deviation of 3.16 dB (Fig. 4.9). The drop in the acceleration amplitude with PTX is close to experimental result of 9.92 dB.
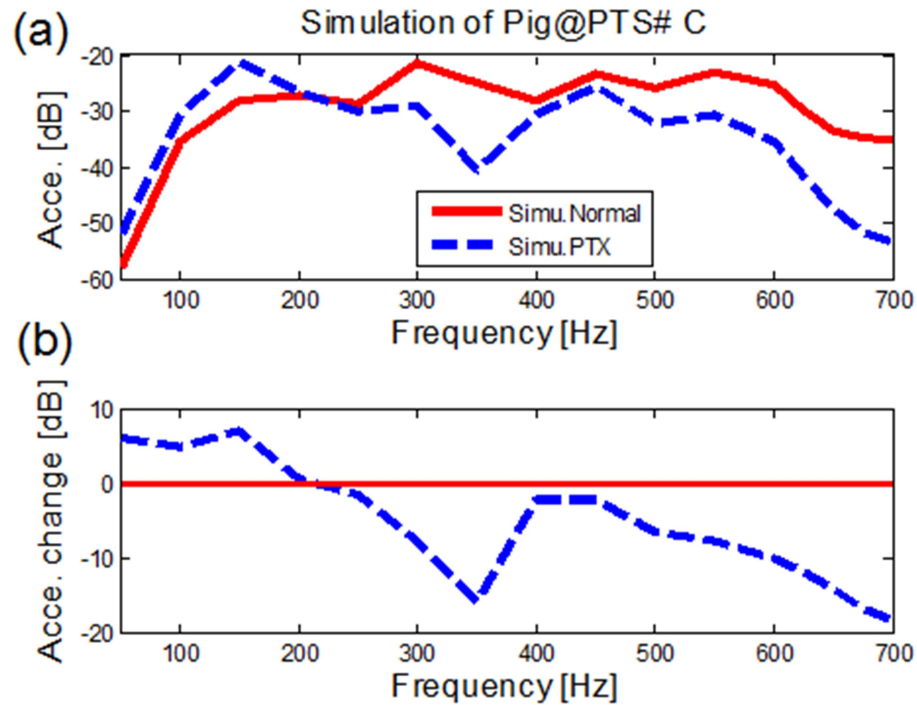
Figure 4.9 Simulation results for normal versus PTX state at point #C. (a) The simulation results of normal and PTX state; (b) The normalized PTX results.

The cross section image of torso displacement in the left to right direction and air acoustic pressure at frequencies of 600 Hz is shown in Fig. 4.10(a) and (b) for the normal and PTX state of the right lung. The scale for the acoustic pressure is only applicable to the PTX air and not the air in the lungs. Patterns of compression waves emanating from the airways and propagating into the chest are evident and are shown as red and blue (indicating positive and negative displacement) bands. These patterns are changed in the collapsed lung side due to change in lung acoustic properties and the acoustic impedance mismatch between the lung and the air in the chest.
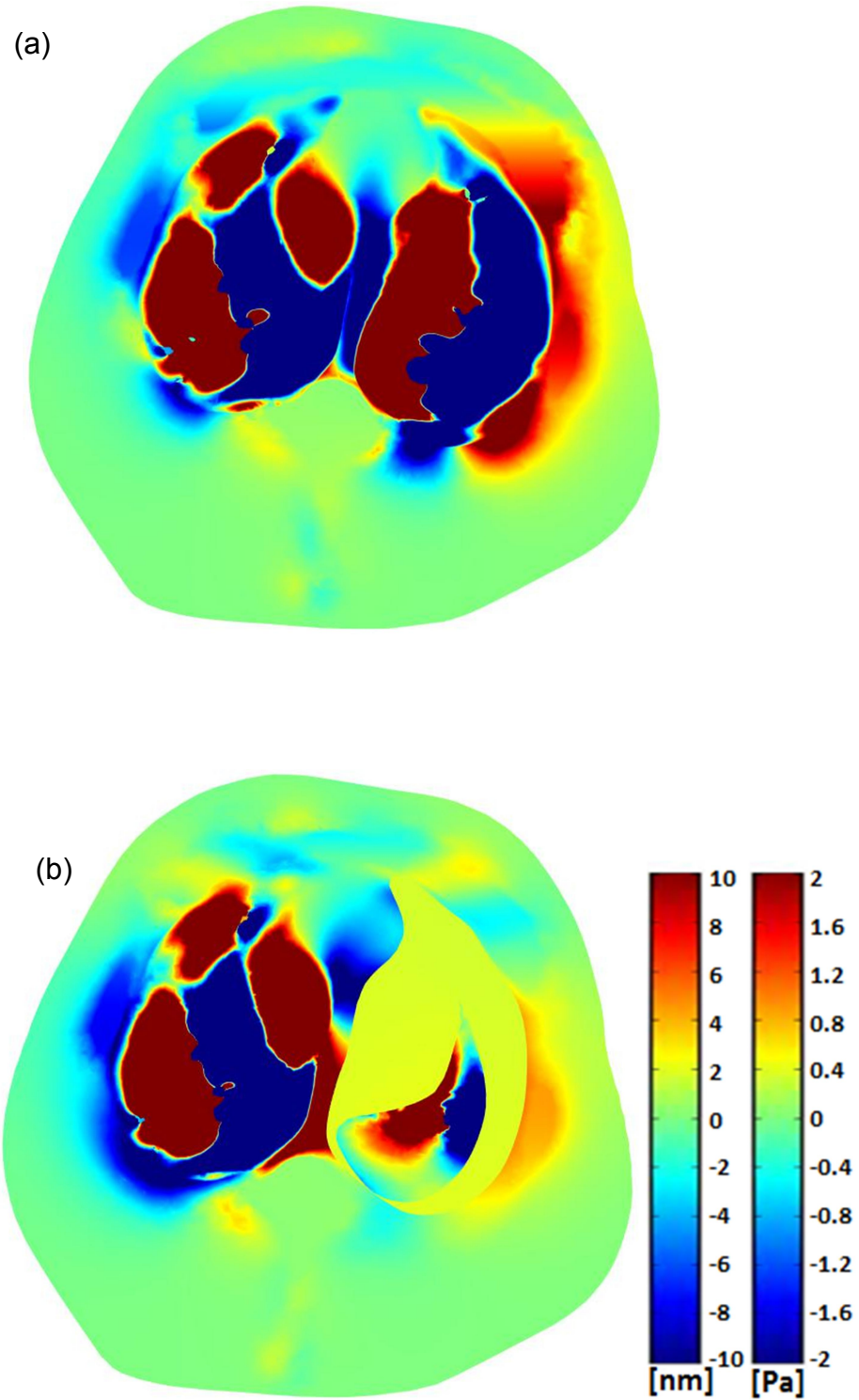
Figure 4.10 Simulation at 600 Hz: cross section of torso showing displacement in the left to right direction for (a) normal state and (b) PTX state. Color bar shows tissue displacement in [nm] and air acoustic pressure in [Pa].

## 4.4    Results of human study
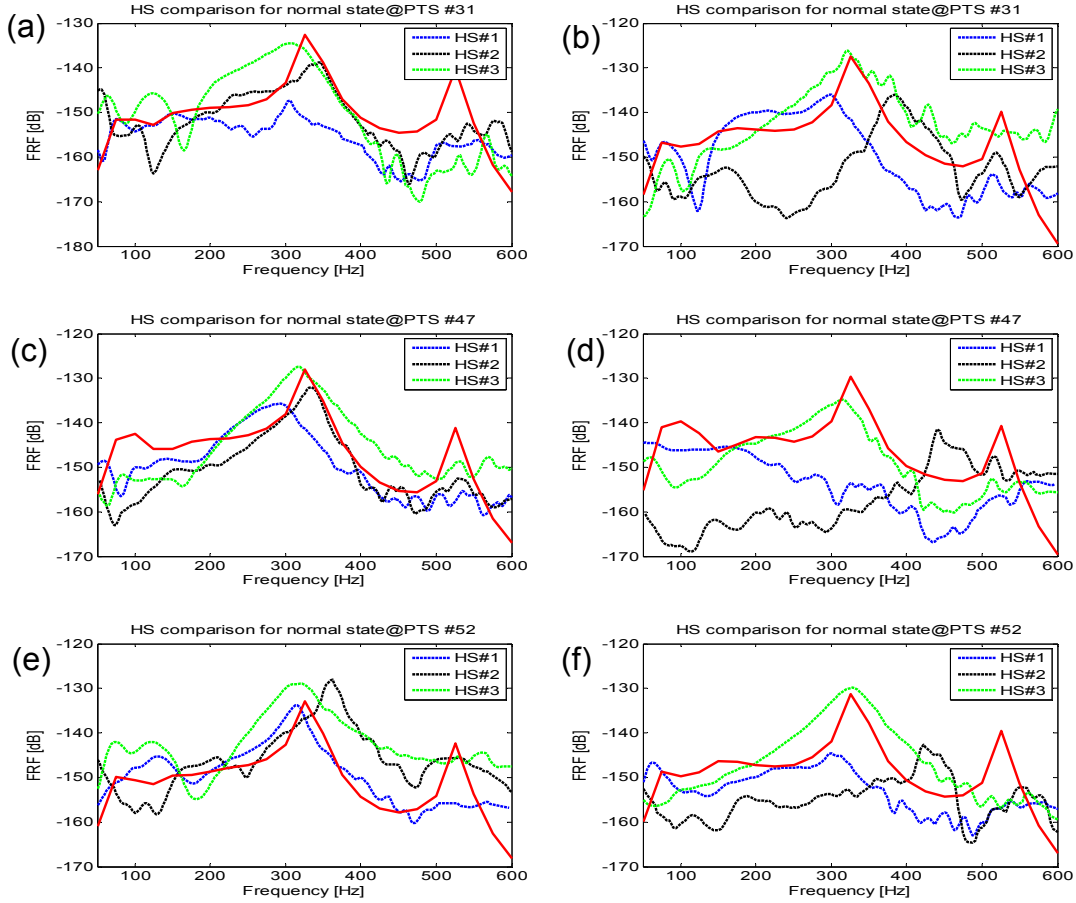


Figure 4.11 point FRF comparison of results of experiment and simulation. (a,c,e) the results of the point FRF for point #31,# 47, and  #52 on the left side of the back (figure 4.2(b)). (b,d,f) the results of the point FRF for point #31,# 47, and  #52 on the right side of the back. "—": the results of simulation.

In the Figure 4.11, the FRF simulation and experimental results of three human subjects at the point #31, 47 and 51 are compared.  The results of simulation capture the trend of the experiment well, though the variations among subjects also can be observed.  In addition, a shift of peaks and dips can also be observed.  This may be because of the difference in the size between the simulation model and the three experimental subjects; the 3D model human used for simulation was scaled to an average size of three human subjects.

FRF images of normal state from simulation and experiment are shown in Fig. 4.12. The red rectangle in the Fig. 4.12(a) indicates the corresponding measurements in the experiments. Both simulation and experiment are in the same color scale which could be seen from the color bar.
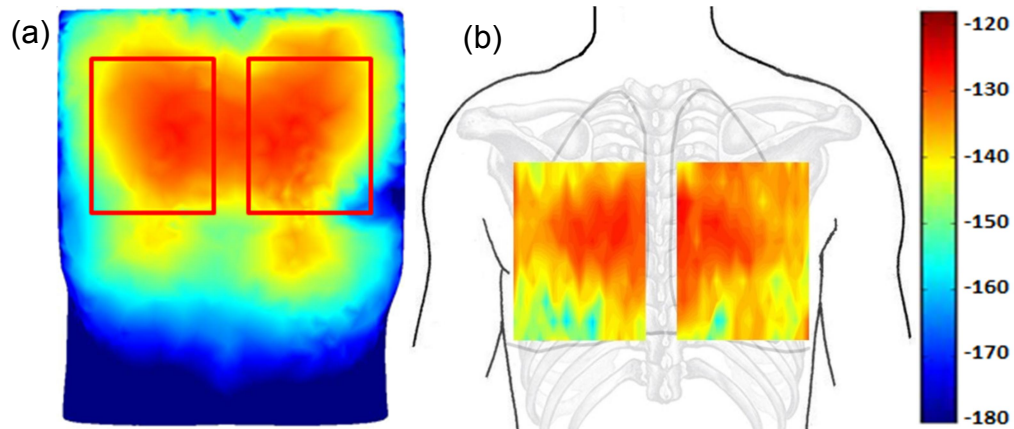


Figure 4.12 FRF comparison at 500 Hz with no pathologies (a) simulation (b) experiment. The rectangle on (a) indicates the corresponding measurements in the experiment. Both simulation and experiment are in the same color scale.
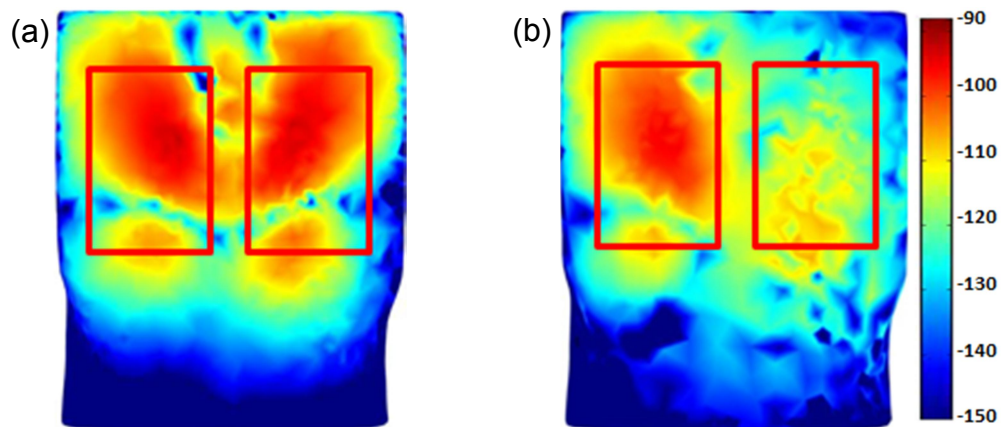


Figure 4.13 Comparison of human simulation in normal and PTX case at 300 Hz. (a) normal condition. (b) PTX = 90% at right lung.

In the figure 4.13, we can observe that, when the PTX condition in 300 Hz, lower amplitude is observed in the PTX lung. This prediction matches the results of the pig study shown in the previous section and reports [56, 75].

In the Figure 4.14, it shows that the effects of tumor in the lung. We can see that more attenuation happening at the tumor region and the wave is distorted due to mismatch impedance. For the interior wave propagation, we could see that compression wave propagating out from the major airways. Cross section images such as those presented in the Fig 4.14 could be used to validate or better understand the images obtained from elastography imaging modalities such as magnetic resonance elastography which were mentioned in the previous sections.
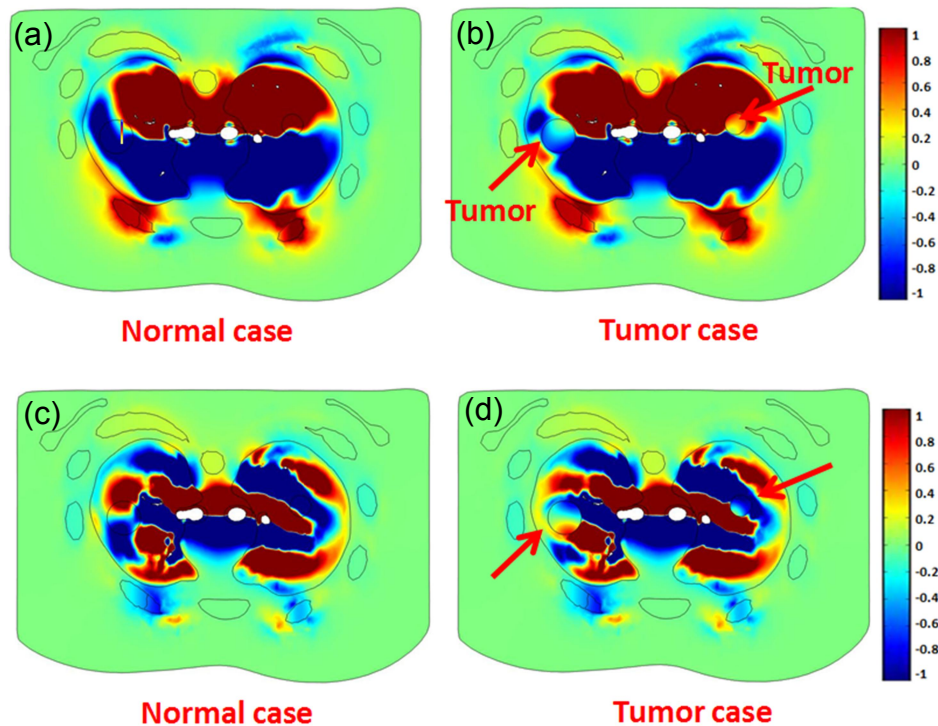


Figure 4.14 Comparison of human simulation in normal and cancer case at 300 Hz (a, b) and 800 Hz (c, d). Figure (a ,c): normal condition. Figure (b, d): tumors were applied at the arrow pointing location.

## 4.5    Discussion

The current experimental technique (described in the sec. 4.2.1 and 4.2.2) is similar to methods presented and applied to cats and dogs in previous studies [20, 57].  In Mansy et al. [57], an electronic stethoscope was used to measure the transmitted acoustic waves on the chest skin surface.  Instead, a LDV was used to for measurements in the current study.  As the electronic stethoscope is attached to skin surface, it may alter the dynamics of the system. A benefit of using a non-contacting LDV is that it does not alter the system it is measuring.

One objective of the present study is to investigate whether the technique of airway insonification can be successfully implemented on relatively large animals like a pig as studies on animals with pulmonary injuries or diseases can be carried out more easily than on human subjects.  Another objective of the study is to develop a computational model of sound transmission in the pig and human chest.  To the best knowledge of the authors, the material properties of bone are close to those of human within our frequency range of interest [14, 51].  So, the complex young's modulus and shear modulus of material properties of human bone were used in the simulation.

Pig and human CT scans were used to build realistic 3D geometries for FE simulation. The results of simulation and experiments on five pig subjects in the normal and PTX states are compared in Fig. 4.7. Inter-subject variability was seen in Fig. 4.7 (a) and (c) for normal and PTX state, respectively.  This variability mainly may be, at least in part, due to the porcine subject size differences.  Simulation results capture the main trends seen in the experiments results.  In Fig. 4.7 (b) and (d), the mean of experimental results of five pigs for both states and the simulation prediction are plotted together for

further comparison. Again, experimental and simulation trends match. However, a shift of peaks and dips can be observed especially in the Fig. 4.7 (b) and (d). This may be because of the difference in the size between the simulation model and the experimental subjects. Chest surface accelerations from model predictions are higher than the experimental results at most of the frequencies of interest. A possible reason for this trend is underestimating the viscous tissue properties for the model.

Due to the limitation of the CT scan image resolution, accurate separation of muscle, fat and skin for the pig and human torso could not be achieved. Therefore, in this computational study, the muscle, fat and skin were considered as materials with the same density and viscoelastic properties as their acoustic properties such as wave speed and attenuation are closer compared to the great difference of these properties from lung acoustic properties. However, these different tissue types and underlying structures will cause wave reflection and refraction. So a computational model with tissues of their respective material properties may achieve closer agreement between simulation and experimental results. Future efforts can focus on creating more accurate and separated 3D models of muscle, fat and skin when clearer CT/MRI images are available in the future.

In the current experimental studies, measurements were performed on a limited portion of the chest surface due to the time it took for the LDV to measure each point consecutively. In future studies, a sensor pad or a vest integrated with sensors that can cover most or all of the chest surface and measure all the points simultaneously or an entire chest measurement by scanning laser Doppler vibrometer could provide more comprehensive experimental information [52].

Fig. 4.8 (a) and (b) suggest that the PTX has an amplitude drop of transmitted sound in the range of 250 to 700 Hz. Similar findings were reported in previous studies on canine subjects [57]. Transmitted sound amplitude decrease in PTX is likely due to the acoustic impedance mismatch at the boundaries of the air in the chest and collapsed lung [57, 58]. This can be seen more clearly in Fig. 4.8 (c), where the average transmitted energy over all frequencies in the experiment for PTX state was lower in all pig subjects. In Fig. 4.9, simulation predictions of PTX were found to be similar to experimental measurements presented in Fig. 4.8(a). The observed decrease in the transmitted acoustic energy with increasing frequency is consistent with the results of the experiment. For both simulation and experiment, the acceleration amplitudes decrease by about 2-20 dB in the 250 - 700 Hz frequency range. Simulation also suggests that that acceleration amplitude drop may continue above the frequencies in the current study. The maximum frequency in the current experimental study was limited 700 Hz to maintain a sufficiently high SNR.

As shown in the current study, detecting PTX was achieved by measuring transmitted sound on the chest surface. In Fig. 4.10, the model was used to predict torso displacement caused by transmitted sound. Visualization of wave motion inside the torso measured by an imaging technique such as MRE, may also help interpret tissue viscoelasticity from wavelength images. An accurate computer simulation of sound transmission through the chest and lungs under normal and pathologic conditions may be helpful to enhance our understanding of auscultation results and our ability to use the sounds for diagnosis. The *in silico* model developed here may also prove useful in

the development of a more effective educational platform for acoustic-based diagnostic methods.

In Fig. 4.11, the simulation and experimental results of human were plotted together for comparison. The trend of the experimental results is pretty similar with each for three HS though deviations of the results can be observed which may be because of the different body size of each HS. Simulation results capture the trend of the experimental one very well. Peaks and dips shift can be also seen in the simulation and experimental results. As mentioned in the previous for pig study, it may be because of difference of simulation model and experimental HS. In addition, by comparing the FRF images of simulation and experiment (Fig. 4.12) on the back of the 3D model and the human subject, we could observe that high amplitude is located in the lung regions in the simulation results (Fig. 4.12(a)). Similar patterns can be observed in experimental results (Fig. 4.12(b)). With the experimental validation, the model was used to investigate pathologies such as PTX (Fig. 4.13) and cancer (Fig.4.14) when the insonification technique was applied. The pattern differences may be useful as features for identification of abnormal conditions. For PTX, the result was consistent with the pig study (Fig. 4.9). For the caner case (Fig. 4.14), it is worth noting that mismatched impedance between the normal and cancer tissue can be observed. The simulation images shown in Fig. 4.10 and 4.14 may help in understanding displacement images obtained from elastography imaging modalities such as MRE.

## 4.6    Conclusion

A computational model was developed for simulating acoustic transmission from airways to the chest surface in a pig and human. The model was validated by

experimental measurements on five porcine subjects before and after PTX induction. The human model was validated with three normal human subjects and pathological investigations were conducted on PTX and cancer with the model. Simulation and experimental findings suggest that certain characteristics of acoustic transmission patterns may be useful in detecting pulmonary abnormalities such as PTX and cancer. Model predictions were found to be consistent with experimental measurements and the literature. The developed computational models can also predict wave propagation inside internal organs which may be of use in assessing the performance of other acoustic diagnostic approaches.

**CHAPTER 5**

**5. CONCLUSION**

**5.1    Summary of Accomplishments**

In this dissertation, the experimental validation of an upper torso acoustic model focusing on the pulmonary system was studied. These computational models simulated sound transmission and measurement via non-contact sensors (SLDV) placed on the torso surface. They also simulated the transmission and measurement of externally introduced sound via the airways or via percussion on the torso surface.  A theoretical model for sound propagation in the airways was integrated into the models and used to predict the acoustic impedance at the airway terminals in the simulation for the effect of several pathologies such as pneumothorax and cancer case.  This work is relevant to the goals of the Audible Human Project in which the development of advanced auscultatory techniques for the lung may be useful in the development of a more effective educational tool for teaching stethoscopic skills in the future. In addition, it could catalyze the development of new inexpensive, portable auscultative methods, as well as more advanced multimode acoustic imaging modalities.

**5.2    Review and discussion for  each chapter**

In Chapter 2, an improved percussive technique was proposed and conducted on porcine and human subjects.   A finite element computational model of sound transmission in the chest for surface acoustic excitation was developed.   The model was validated experimentally for the normal and PTX case. Model predictions were found to be consistent with findings and physical phenomena suggested by the animal and human studies.   The tested surface excitation method is an extension of the

percussion approach that is commonly used during chest exam.  The Simulation and experimental findings suggested that surface percussive excitation may be useful in detecting pulmonary abnormalities such as a large PTX. The model may also prove useful for detecting other abnormalities, and developing learning tools. Because the interior of the computational model could be viewed and investigated,   the models was able to predict wave propagation inside the chest which may be of use in assessing the performance of other acoustic diagnostic approaches, such as MR elastography.

Sound insonification was proposed in Chapter 3 for study the sound transmission.  The experiment was conducted on excised pig lungs. A comprehensive computational simulation model of sound transmission through a porcine excised lung was also developed and experimentally evaluated. Parenchymal and major airway geometry of this "subject-specific" model was created from x-ray CT images. In the computational model, the lung parenchyma was modeled as a poroviscoelastic material using Biot theory. Acoustic impedances were applied to the airway terminal segments to represent the downstream un-modeled airway segments base Horsefield model. The results of FE simulation were validated by comparisons with experimental measurements obtained using scanning laser Doppler vibrometry on the surface of an excised, preserved lung. Two levels of airway detail were used in the FE simulations. From the results of comparison, it was suggested that the model with fewer airway segments was closer to experimental measurements. The FE model was also used to visualize vibroacoustic pressure and motion inside the lung and its airways caused by the acoustic input. Effects of diffuse lung fibrosis and localized tumors on the lung acoustic response were visualized from FE simulations. This type of visualization could potentially be compared

and matched with images from elastography measurements to better quantify lung material properties, such as stiffness.

In Chapter 4, the same airway insonification technique was applied to the upper torso of porcine and human subjects. Corresponding computational models of the upper torso with integrated organs including lungs, ribs, and airway trees were developed for simulating acoustic transmission from the airways to the chest surface. The model was validated by experimental measurements before and after pneumothorax induction. Findings of comparison suggested that certain characteristics of acoustic transmission patterns may be useful in detecting pulmonary abnormalities such as PTX. Model predictions were found to be consistent with experimental measurements and the literature. The developed computational models were also used to simulate lungs with other pathological conditions such as cancer. With the validated models, wave propagation inside internal organs was studied and effects caused by different abnormal conditions of the pulmonary system were discussed. The development of the computational models may be of use in assessing the performance of other acoustic diagnostic approaches.

## 5.3    Recommendations of Future research

**Airways generation**

In order to investigate the sound transmission through the pulmonary system and torso using computational methods, the finite element model of the airways needs to be created. In the current study, the generation of the model of the airways of pigs and human was based on their CT or MRI images. CT and MRI imaging can deliver useful and relatively accurate anatomical information for lung airways up to several

bifurcations; however, due to the limit of image resolution, any segments of several millimeters in length and below cannot be viewed easily. In addition, manually creating the airways could be very time-consuming. So, in the future research it would not be practical to model the entire bronchial tree within any explicit analytical framework, down through nominally 2.35 million branch segments in a human study. Although, as discussed in the previous sections the small airway segments only contribute a very small portion of the total sound energy that is transmitted to the chest surface and the airway tree can be simplified by truncating the small airway segments and applying the terminal impedance calculated by the Horsfield model of the human lung. To better understand the contributions of the small airways, more airway segments could be taken into deeper consideration in the future study. One approach that can be used to quickly and easily generate more airways is to programmatically create the airway geometries. For example, Kitaoka implements a deterministic algorithm that can create an intricate airway geometry using nine branching laws and four supplementary laws. These laws govern how the branching duct structure grows, from airway length and diameter to bifurcation angles. The algorithm has proved itself to be an efficient means of generating airway structures that are statistically relevant to human airways, and it has been further developed to generate 4D models of the human lung, where flow through the lung is transient, and the lung volume itself changes over inhalation and exhalation. In comparison, Tawhai et al adapted a different approach using image registration and segmentation. Image segmentation provides several benefits compared to Kitoaka's method, namely the accuracy of the airway structure being generated.

Because the digital geometries are grown based on CT/MRI data, the level of accuracy on the patient-specific level is higher.

**Lung MRE**

In the past decade, the phase contrast-based technique known as magnetic resonance elastography (MRE) has been applied to the lungs in pilot studies with limited success. MRE seeks to provide a map of the viscoelastic properties within the region of interest that affects the shear wave motion that MRE measures. Previously, MRE has been successfully applied to the study of the mechanical properties of a variety of other organs and soft tissue regions in vivo, including the breast, brain, kidney, prostate, liver and muscle. Application to the lungs has proven more challenging, given the poor signal-to-noise available in imaging due to much lower presence of hydrogen in air than in soft tissue (water), and the complex nature of vibratory wave propagation found in the lungs. An experimentally validated computational model could be used as a supporting approach to better understanding of mechanical wave motion in the lungs. MRE would also aid in identification of viscoelastic properties of specific organ tissue, which will benefit more accurate computational simulations of lung sound generation and transmission in return.

**Pathological models**

One of the objectives of AHP is to study alterations in sound generation or transmission in the human chest under various abnormal conditions caused by the changes in lung structure, mechanical properties, boundary conditions and some other factors. These abnormal pathological conditions can be lung fibrosis (ILD), surfactant imbalance, tumors, emphysema, PTX, HTX, pleural effusion, pneumonia, emphysema, and COPD.

The experimental investigations on some of these lung diseases and injuries have been reported in previous literature. However, it is still very difficult to completely understand the alterations of acoustic properties caused by some of these lung diseases or injuries due to the small number of patients and the imitations of experimental approaches. With the aid of the developed computational models, more pathological conditions causing changes on acoustic properties will be able to get a deeper understanding and better interpretation of the acoustic measurements, including MRE measurements, and aid in differentiating various pathologies.

**Study of Lung (breath) Sounds**

In the current research, the way to study of sound transmission was to externally introduce sound into the lung. These two active sound generating methods, as described, could better understand and control the quantity of the input sound applied to the human body. However, the sound originally generated from normal breathing could be considered as a unique alternative excitation source which is already inside of the lungs. Current investigations on breath sounds are limited. This is because of the complex structural nature of the lung and the difficulty in lung sound measurement under the subglottal region. Lung sounds are known to contain spatial information that can be accessed using simultaneous acoustic measurements at multiple locations. If better and precise fundamental understanding of the lung sounds can be achieved, more information about the severity and location of the trauma or pathology will be provided for lung disease diagnostics.

**Educational Tool for Physicians.**

From an educational perspective, recent studies have emphasized the continued importance of skilled auscultation in medicine and the fact that this skill is in decline among younger physicians. With the technologies of virtual reality and the experimentally validated computational model from the outcome of AHP, physicians could be provided a more effective educational experience. A student would not just listen to audio recordings but would be able to interactively vary anatomy and type and degree of pathology, as well as sensor position, type and contact pressure, and hear, "see" and "feel" (if integrated within a haptic environment) the results and associate them with quantifiable metrics.

# CITED LITERATURE

1. Acikgoz S, Ozer MB, Royston TJ, et al. (2008) Experimental and Computational Models for Simulating Sound Propagation Within the Lungs. J Vib Acoust 130:nihpa45263.

2. Athanassiadi K, Kalavrouziotis G, Loutsidis A, et al. (1998) Surgical Treatment of Spontaneous Pneumothorax: Ten-year Experience. World J Surg 22:803–806.

3. Benedetto G, Dalmasso F, Spagnolo R (1988) Surface distribution of crackling sounds. IEEE Trans Biomed Eng 35:406–12.

4. Bergstresser T, Ofengeim D, Vyshedskiy A, et al. (2002) Sound transmission in the lung as a function of lung volume. J Appl Physiol 93:667–74.

5. Biot MA (1956) Theory of Propagation of Elastic Waves in a Fluid-Saturated Porous Solid. II. Higher Frequency Range. J Acoust Soc Am 28:179.

6. Biot MA (1956) Theory of Propagation of Elastic Waves in a Fluid-Saturated Porous Solid. I. Low-Frequency Range. J Acoust Soc Am 28:168.

7. Bohadana AB, Kraman SS (1989) Transmission of sound generated by sternal percussion. J Appl Physiol 66:273–277.

8. Bohadana AB, Patel R, Kraman SS (1989) Contour maps of auscultatory percussion in healthy subjects and patients with large intrapulmonary lesions. Lung 167:359–372.

9. Böhme HR BH (1972) Variable low-frequency sound conduction of the lung in pulmonary emphysema. Z Gesamte Inn Med 27:765–770.

10. Bourbié T, Coussy O (1987) Acoustics of Porous Media. 334.

11. Bourke S, Nunes D, Stafford F, et al. (1989) Percussion of the chest re-visited: A comparison of the diagnostic value of ausculatory and conventional chest percussion. Ir J Med Sci 158:82–84.

12. Charleston-Villalobos S, Cortés-Rubiano S, González-Camerena R, et al. (2004) Respiratory acoustic thoracic imaging (RATHI): Assessing deterministic interpolation techniques. Med Biol Eng Comput 42:618–626.

13. Choi J, Xia G, Tawhai MH, et al. (2010) Numerical study of high-frequency oscillatory air flow and convective mixing in a CT-based human airway model. Ann Biomed Eng 38:3550–71.

14. Cowin SC (2001) Bone mechanics handbook, 2nd ed. Gulf Publishing Company, Huston,TX

15. D'yachenko AI, Lyubimov GA (1988) Progration of sound in pulmonary parenchyma. Fluid Dyn 23:641–652.

16. Dai Z, Peng Y, Henry B, et al. (2014) A Comprehensive Computational Model of Sound Transmission through the Porcine Lung. J. Acoust. Soc. Am.

17. Dai Z, Peng Y, Mansy HA, et al. (2014) Comparison of Poroviscoelastic Models for Sound and Vibration in the Lungs. J Vib Acoust 136:0510121–5101211.

18. Dai Z, Peng Y, Mansy HA, et al. (2014) Comparison of Poroviscoelastic Models for Sound and Vibration in the Lungs. J Vib Acoust 136:051012.

19. Delingette H, Pennec X, Soler L, et al. (2006) Computational Models for Image-Guided Robot-Assisted and Simulated Medical Interventions. Proc IEEE 94:1678–1688.

20. Donnerberg RL, Druzgalski CK, Hamlin RL, et al. (1980) Sound transfer function of the congested canine lung. Br J Dis Chest 74:23–31.

21. DuBois AB, Brody AW, Lewis DH, Burgess BFJ (1956) Oscillation Mechanics of Lungs and Chest in Man. J Appl Physiol 8:587–594.

22. Ebihara T, Venkatesan N, Tanaka R, Ludwig MS (2000) Changes in extracellular matrix and tissue viscoelasticity in bleomycin-induced lung fibrosis. Temporal aspects. Am J Respir Crit Care Med 162:1569–76.

23. Feldgus S, Landis CR (2000) Large-Scale Computational Modeling of [Rh(DuPHOS)] + -Catalyzed Hydrogenation of Prochiral Enamides:  Reaction Pathways and the Origin of Enantioselection. J Am Chem Soc 122:12714–12727.

24. Fung Y (1997) Biomechanics: Circulation. 571.

25. Garner E, Lakes R, Lee T, et al. (2000) Viscoelastic Dissipation in Compact Bone: Implications for Stress-Induced Fluid Flow in Bone. J Biomech Eng 122:166.

26. Von Gierke HE, Oestreicher HL, Franke EK, et al. (1952) Physics of Vibrations in Living Tissues. J Appl Physiol 4:886–900.

27. Goll JH (1979) The Design of Broad-Band Fluid-Loaded Ultrasonic Transducers. IEEE Trans Sonics Ultrason 26:385–393.

28. Goss BC, McGee KP, Ehman EC, et al. (2006) Magnetic resonance elastography of the lung: technical feasibility. Magn Reson Med 56:1060–6.

29. Guarino JR (1974) Auscultatory percussion. A new aid in the examination of the chest. J Kans Med Soc 75:193–4.

30. Guarino J (1980) AUSCULTATORY PERCUSSION OF THE CHEST. Lancet 315:1332–1334.

31. Habib RH, Chalker RB, Suki B, Jackson AC (1994) Airway geometry and wall mechanical properties estimated from subglottal input impedance in humans. J Appl Physiol 77:441–451.

32. Habib RH, Suki B, Bates JH, Jackson AC (1994) Serial distribution of airway mechanical properties in dogs: effects of histamine. J Appl Physiol 77:554–566.

33. Hansen LB, Brøns M, Nielsen NT (1986) [Auscultatory percussion of the lungs. Prospective comparison of 2 methods of clinical examination of the lungs]. Ugeskr Laeger 148:323–5.

34. Heng P-A, Cheng C-Y, Wong T-T, et al. (2004) A Virtual-Reality Training System for Knee Arthroscopic Surgery. IEEE Trans Inf Technol Biomed 8:217–227.

35. Henry B, Dai Z, Peng Y, et al. (2014) Investigation of pulmonary acoustic simulation: comparing airway model generation techniques. In: Molthen RC, Weaver JB (eds) SPIE Med. Imaging. International Society for Optics and Photonics, p 90380W

36. Horsfield K, Cumming G (1968) Morphology of the bronchial tree in man. J Appl Physiol 24:373–383.

37. Horsfield K, Dart G, Olson DE, et al. (1971) Models of the human bronchial tree. J Appl Physiol 31:207–217.

38. Horsfield K, Kemp W, Phillips S (1982) An asymmetrical model of the airways of the dog lung. J Appl Physiol 52:21–26.

39. Hu S, Hoffman EA, Reinhardt JM (2001) Automatic lung segmentation for accurate quantitation of volumetric X-ray CT images. IEEE Trans Med Imaging 20:490–8.

40. Jahed M, Lai-Fook SJ (1994) Stress wave velocity measured in intact pig lungs with cross-spectral analysis. J Appl Physiol 76:565–571.

41. Jahed M, Lai-Fook SJ, Bhagat PK, Kraman SS (1989) Propagation of stress waves in inflated sheep lungs. J Appl Physiol 66:2675–2680.

42. Jenkyn TR, Ehman RL, An K-N (2003) Noninvasive muscle tension measurement using the novel technique of magnetic resonance elastography (MRE). J Biomech 36:1917–1921.

43. Kemper J, Sinkus R, Lorenzen J, et al. (2004) MR elastography of the prostate: initial in-vivo application. Rofo 176:1094–9.

44. Kitaoka H, Takaki R, Suki B (1999) A three-dimensional model of the human airway tree. J Appl Physiol 87:2207–2217.

45. Klatt D, Hamhaber U, Asbach P, et al. (2007) Noninvasive assessment of the rheological behavior of human organs using multifrequency MR elastography: a study of brain and liver viscoelasticity. Phys Med Biol 52:7281–94.

46. Kompis M (2001) Acoustic Imaging of the Human Chest. Chest 120:1309–1321.

47. Kraman SS, Austrheim O (1983) Comparison of lung sound and transmitted sound amplitude in normal men. Am Rev Respir Dis 128:451–4.

48. Kraman SS (1983) Speed of low-frequency sound through lungs of normal men. J Appl Physiol 55:1862–1867.

49. Kraman SS, Bohadana AB (1989) Transmission to the chest of sound introduced at the mouth. J Appl Physiol 66:278–281.

50. Kruse SA, Rose GH, Glaser KJ, et al. (2008) Magnetic resonance elastography of the brain. Neuroimage 39:231–7.

51. Lakes RS, Katz JL, Sternstein SS (1979) Viscoelastic properties of wet cortical bone—I. Torsional and biaxial studies. J Biomech 12:657–678.

52. Li B, You JH, Kim Y-J (2013) Low frequency acoustic energy harvesting using PZT piezoelectric plates in a straight tube resonator. Smart Mater Struct 22:055013.

53. Liu F, Mih JD, Shea BS, et al. (2010) Feedback amplification of fibrosis through matrix stiffening and COX-2 suppression. J Cell Biol 190:693–706.

54. Mahagnah M, Gavriely N (1995) Gas density does not affect pulmonary acoustic transmission in normal men. J Appl Physiol 78:928–937.

55. Manduca A, Oliphant TE, Dresner MA, et al. (2001) Magnetic resonance elastography: Non-invasive mapping of tissue elasticity. Med Image Anal 5:237–254.

56. Mansy HA, Royston TJ, Balk RA, Sandler RH (2002) Pneumothorax detection using computerised analysis of breath sounds. Med Biol Eng Comput 40:526–532.

57. Mansy HA, Royston TJ, Balk RA, Sandler RH (2002) Pneumothorax detection using pulmonary acoustic transmission measurements. Med Biol Eng Comput 40:520–525.

58. Mansy HA, Royston TJ, Sandler RH (2001) Acoustic characteristics of air cavities at low audible frequencies with application to pneumoperitoneum detection. Med Biol Eng Comput 39:159–167.

59. Marescaux J, Clément JM, Tassetti V, et al. (1998) Virtual reality applied to hepatic surgery simulation: the next revolution. Ann Surg 228:627–34.

60. Mariappan YK, Glaser KJ, Hubmayr RD, et al. (2011) MR elastography of human lung parenchyma: technical development, theoretical modeling and in vivo validation. J Magn Reson Imaging 33:1351–61.

61. Mariappan YK, Kolipaka A, Manduca A, et al. (2012) Magnetic resonance elastography of the lung parenchyma in an in situ porcine model with a noninvasive mechanical driver: correlation of shear stiffness with trans-respiratory system pressures. Magn Reson Med 67:210–7.

62. McGee KP, Lake D, Mariappan Y, et al. (2011) Calculation of shear stiffness in noise dominated magnetic resonance elastography data based on principal frequency estimation. Phys Med Biol 56:4291–309.

63. McGee KP, Hubmayr RD, Ehman RL (2008) MR elastography of the lung with hyperpolarized 3He. Magn Reson Med 59:14–8.

64. Mow VC, Kuei SC, Lai WM, Armstrong CG (1980) Biphasic Creep and Stress Relaxation of Articular Cartilage in Compression: Theory and Experiments. J Biomech Eng 102:73.

65. Murray A, Neilson J (1975) Diagnostic percussion sounds: 1. A qualitative analysis. Med. Biol. Eng.

66. Napadow VJ, Mai V, Bankier A, et al. (2001) Determination of regional pulmonary parenchymal strain during normal respiration using spin inversion tagged magnetization MRI. J Magn Reson Imaging 13:467–74.

67. Nedel LP, Thalmann D Real time muscle deformations using mass-spring systems. Proceedings. Comput. Graph. Int. (Cat. No.98EX149). IEEE Comput. Soc, pp 156–165

68. Niu Y, Shen W, Stuhmiller JH (2007) Finite element models of rib as an inhomogeneous beam structure under high-speed impacts. Med Eng Phys 29:788–98.

69. Ogata K (2004) System dynamics, 4th ed. 4:107.

70. Ozer MB, Acikgoz S, Royston TJ, et al. (2007) Boundary element model for simulating sound propagation and source localization within the lungs. J Acoust Soc Am 122:657–61.

71. Paciej R, Vyshedskiy A, Shane J, Murphy R (2003) Transpulmonary speed of sound input into the supraclavicular space. J Appl Physiol 94:604–11.

72. Pantea MA, Maev RG, Malyarenko E V, Baylor AE (2012) A physical approach to the automated classification of clinical percussion sounds. J Acoust Soc Am 131:608–19.

73. Panzer MB, Myers BS, Capehart BP, Bass CR (2012) Development of a finite element model for blast brain injury and the effects of CSF cavitation. Ann Biomed Eng 40:1530–44.

74. Pasterkamp H, Consunji-Araneta R, Oh Y, Holbrow J (1997) Chest surface mapping of lung sounds during methacholine challenge. Pediatr Pulmonol 23:21–30.

75. Peng Y, Dai Z, Mansy HA, et al. (2014) Sound transmission in the chest under surface excitation: an experimental and computational study with diagnostic applications. Med Biol Eng Comput 52:695–706.

76. Plewes DB, Bishop J, Samani A, Sciarretta J (2000) Visualization and quantification of breast cancer biomechanical properties with magnetic resonance elastography. Phys Med Biol 45:1591–1610.

77. Rice DA (1983) Sound speed in pulmonary parenchyma. J Appl Physiol 54:304–308.

78. Royston TJ, Acikgoz S, Ozer MB, et al. (2008) Advances in Computational Modeling of Sound Propagation in the Lungs and Torso with Diagnostic Applications. Biomed. Appl. Vib. Acoust. Ther. Bioeffect Model. ASME Press, p 32

79. Royston TJ, Zhang X, Mansy HA, Sandler RH (2002) Modeling sound transmission through the pulmonary system and chest with application to diagnosis of a collapsed lung. J Acoust Soc Am 111:1931.

80. Royston TJ, Dai Z, Chaunsali R, et al. (2011) Estimating material viscoelastic properties based on surface wave measurements: a comparison of techniques and modeling assumptions. J Acoust Soc Am 130:4126–38.

81. Royston TJ, Dai Z, Chaunsali R, et al. (2011) Estimating material viscoelastic properties based on surface wave measurements: a comparison of techniques and modeling assumptions. J Acoust Soc Am 130:4126–38.

82. Royston T, Acikgoz S (2008) Advances in Computational Modeling of Sound Propagation in the Lungs and Torso with Diagnostic Applications. …  Appl. …

83. Schmidt S, Cela C, Singh V, Weiland J (2008) Computational modeling of electromagnetic and thermal effects for a dual-unit retinal prosthesis: inductive telemetry, temperature increase, and current densities in the. Artif. Sight

84. Setton LA, Zhu W, Mow VC (1993) The biphasic poroviscoelastic behavior of articular cartilage: Role of the surface zone in governing the compressive behavior. J Biomech 26:581–592.

85. Shah NS, Kruse SA, Lager DJ, et al. (2004) Evaluation of renal parenchymal disease in a rat model with magnetic resonance elastography. Magn Reson Med 52:56–64.

86. Siklosi M, Jensen O, Tew R, Logg A (2008) Multiscale modeling of the acoustic properties of lung parenchyma. ESAIM Proc 78–97.

87. Simon BR, Liable JP, Pflaster D, et al. (1996) A Poroelastic Finite Element Formulation Including Transport and Swelling in Soft Tissue Structures. J Biomech Eng 118:1.

88. Simon BR (1992) Multiphase Poroelastic Finite Element Models for Soft Tissue Structures. Appl Mech Rev 45:191.

89. Sinkus R, Tanter M, Xydeas T, et al. (2005) Viscoelastic shear properties of in vivo breast lesions measured by MR elastography. Magn Reson Imaging 23:159–65.

90. Suh J, DiSilvestro M (1999) Biphasic poroviscoelastic behavior of hydrated biological soft tissue. J.  …

91. Suki B, Barabasi AL, Lutchen KR (1994) Lung tissue viscoelasticity: a mathematical framework and its molecular basis. J Appl Physiol 76:2749–2759.

92. Suki B, Habib RH, Jackson AC (1993) Wave propagation, input impedance, and wall mechanics of the calf trachea from 16 to 1,600 Hz. J Appl Physiol 75:2755–2766.

93. Tawhai MH, Hunter P, Tschirren J, et al. (2004) CT-based geometry analysis and finite element models of the human and ovine bronchial tree. J Appl Physiol 97:2310–21.

94. Tisi GM, Minh VD, Friedman PJ (1975) In vivo dimensional response of airways of different size to transpulmonary pressure. J Appl Physiol 39:23–29.

95. Venkatesh SK, Yin M, Ehman RL (2013) Magnetic resonance elastography of liver: technique, analysis, and clinical applications. J Magn Reson Imaging 37:544–55.

96. Vovk I V., Grinchenko VT, Oleinik VN (1995) Modeling the acoustic properties of the chest and measuring breath sounds. Acoust Phys 41:667–676.

97. Walker HK, Hall WD HJ (1990) The Funduscopic Examination -Clinical Methods: The History, Physical, and Laboratory Examinations:The Funduscopic, 3rd ed. Butterworths

98. Warner L, Yin M (2009) Kidney stiffness measured in an animal model of unilateral renal arterial stenosis using 2D MR Elastography. Proc. …

99. Winter R, Smethurst D (1999) Percussion -- a new way to diagnose a pneumothorax. Br J Anaesth 83:960–961.

100. Wodicka GR, Aguirre A, DeFrain PD, Shannon DC (1992) Phase delay of pulmonary acoustic transmission from trachea to chest wall. IEEE Trans Biomed Eng 39:1053–9.

101. Wodicka GR, Stevens KN, Golub HL, et al. (1989) A model of acoustic transmission in the respiratory system. IEEE Trans Biomed Eng 36:925–34.

102. Wodicka GR, Stevens KN, Golub HL, et al. (1989) A model of acoustic transmission in the respiratory system. IEEE Trans Biomed Eng 36:925–34.

103. Wodicka GR, DeFrain PD, Kraman SS (1994) Bilateral asymmetry of respiratory acoustic transmission. Med Biol Eng Comput 32:489–494.

104. Yang Z, Smolinski P (2006) Dynamic finite element modeling of poroviscoelastic soft tissue. Comput Methods Biomech Biomed Engin 9:7–16.

105. Yasar TK, Royston TJ, Magin RL (2013) Wideband MR elastography for viscoelasticity model identification. Magn Reson Med 70:479–89.

106. Yen RT, Fung YC, Ho HH, Butterman G (1986) Speed of stress wave propagation in lung. J Appl Physiol 61:701–705.

107. Yernault J, Bohadana A (1995) Chest percussion. Eur Respir J 8:1756–1760.

108. Yushkevich PA, Piven J, Hazlett HC, et al. (2006) User-guided 3D active contour segmentation of anatomical structures: significantly improved efficiency and reliability. Neuroimage 31:1116–28.

109. (2003) The National Library of Medicines Visible Human Project. http://www.nlm.nih.gov/research/visible/visible_human.html.

# APPENDICES

**Title:** Sound transmission in the chest under surface excitation: an experimental and computational study with diagnostic applications

**Author:** Ying Peng

**Publication:** Medical and Biological Engineering and Computing

**Publisher:** Springer

**Date:** Jan 1, 2014

Copyright © 2014, International Federation for Medical and Biological Engineering

Logged in as:
Ying Peng
Account #:
3000912113

**LOGOUT**

## Quick Price Estimate

**This reuse request is free of charge although you are required to obtain a license through Rightslink and comply with the license terms and conditions. You will not be charged for this order. To complete this transaction, click the Continue button below.**

**I would like to...** ❓    use in a thesis/dissertation ▼

**Portion** ❓    Full text ▼

**Number of copies** ❓    100

**Are you the author of this Springer article?** ❓    Yes ▼

**You are ...**    a contributor of the new work ▼

**Select your currency**    USD - $ ▼

**Quick Price**    0.00 USD

**No content delivery.** This service provides permission for reuse only. Once licensed, you may use the content according to the terms of your license.

Price quoted is an estimate based on this request for this title only. Final price will depend on the total amount of requested Springer material.

**The material can only be used for the purpose of defending your thesis limited to university-use only. If the thesis is going to be published, permission needs to be re-obtained (selecting "book/textbook" as the type of use).**

**QUICK PRICE**    **CONTINUE**

To request permission for a type of use not listed, please contact Springer Rights & Permissions Team.

To purchase or view a PDF of this article, please close this window and select "add to shopping cart".

Exchange rates under license from XE.com.

F

**Copyright Clearance Center**

**RightsLink®**

Home | Account Info | Help | Live Chat

| | |
|---|---|
| **Title:** | A comprehensive computational model of sound transmission through the porcine lung |
| **Author:** | Zoujun Dai, Ying Peng, Brian M. Henry, et al. |
| **Publication:** | The Journal of the Acoustical Society of America |
| **Volume/Issue** | 136/3 |
| **Publisher:** | AIP Publishing LLC |
| **Date:** | Dec 31, 1969 |
| **Page Count:** | 11 |

Copyright © 2014, Acoustical Society of America

Logged in as:
Ying Peng
Account #:
3000912113

LOGOUT

## Quick Price Estimate

**AIP Publishing LLC grants a license for all orders, including $0 orders. Please select the Continue button and place an order for this reuse.**

**I would like to...** ⓘ    reuse in a thesis/dissertation ▼

**Select your currency**    USD - $ ▼

**Requestor Type** ⓘ    Author (original article) ▼

**Format** ⓘ    Print and electronic ▼

**Portion** ⓘ    Excerpt (> 800 words) ▼

**Will you be translating?** ⓘ    No ▼

**Quick Price**    0.00 USD

QUICK PRICE    CONTINUE

Content Delivery: Once licensed, you may reuse the content only for the reuse purposes specified. No content delivery is offered through this service.

This permission does not apply to images that are not credited to this article. For any images credited to a different source, you will need to obtain permission from the journal or book referenced in the figure or table legend or credit line before making any use of the image(s) or table(s).

For permissions and publications other than those listed, please contact the publisher directly.

## And the statement from transfer copyright form of SPIE

**VITA**

NAME: Ying Peng

EDUCATION: B.S., Mechanical Engineering, Beijing Technology and Business University, Beijing, China, 2006.

M.S., Mechanical Engineering, University of Illinois at Chicago, Chicago, USA, 2009.

Ph.D., Mechanical Engineering, University of Illinois at Chicago, Chicago, USA, 2015.

EXPERIENCE: Research Assistant, Acoustics and Vibration Laboratory, Department of Mechanical & Industrial Engineering, University of Illinois at Chicago, August 2009 - December 2014.

Teaching Assistant, ME 210 Engineering Dynamics, University of Illinois at Chicago, Spring 2010, 2013 and 2014.

Teaching Assistant, ME 312 Dynamic Systems and Control, University of Illinois at Chicago, Fall 2013.

HONORS: Provost's Award for Graduate Research, UIC, 2011.

Graduate College Travel Awards, UIC, 2013, 2014.

PROFESSIONAL MEMBERSHIP: American Society of Mechanical Engineers
Acoustical Society of America

PUBLICATIONS: *Archival Journal*

1. Peng, Y., Dai, Z., Henry, B. M., Mansy, H. A., Sandler, R. H., & Royston, T. J. (2015). Sound Transmission in Porcine Thorax through Airway Insonification, Medical & biological engineering & computing, Accepted.

2. Peng, Y., Dai, Z., Mansy, H. A., Sandler, R. H., Balk, R. A., & Royston, T. J. (2014). Sound transmission in the chest under surface excitation: an experimental and computational study with diagnostic applications. Medical & biological engineering & computing, 52(8), 695-706.

3. Dai, Z, Peng, Y, Mansy, H. A, Sandler, R. H, Royston, T. J., (2014). Experimental and Computational Studies of Sound Transmission in a Branching Airway Network Embedded in a Compliant Viscoelastic Medium, Journal of Sound and Vibration. In press.

4. Dai, Z., Peng, Y., Henry, B. M., Mansy, H. A., Sandler, R. H., & Royston, T. J. (2014). A comprehensive computational model of sound transmission through the porcine lung. The Journal of the Acoustical Society of America, 136(3), 1419-1429.

5. Dai, Z., Peng, Y., Mansy H. A., Sandler R. H., Royston T. J. (2014). Comparison of poroviscoelastic models for sound and vibration in the lungs, Journal of Vibration and Acoustics, in press, doi:10.1115/1.4026436.

6. Dai, Z., Peng, Y., Henry, B. M., Mansy, H. A., Sandler, R. H., & Royston, T. J. (2014). A comprehensive computational model of sound transmission through the porcine lung. The Journal of the Acoustical Society of America, 136(3), 1419-1429.

7. Royston, T. J., Dai, Z., Chaunsali, R., Liu, Y., Peng, Y., & Magin, R. L. (2011). Estimating material viscoelastic properties based on surface wave measurements: A comparison of techniques and modeling assumptions. The Journal of the Acoustical Society of America, 130(6), 4126-4138.

*Conference Papers & Presentations*

1. Peng Y, Dai Z, Henry B, Mansy HA, Royston TJ, A Comprehensive Computational Model of Sound Transmission through the Porcine Lung, 166th Meeting of the Acoustical Society of America, (Dec. 2-6, 2013, San Francisco, CA)

2. Peng Y, Dai Z, Henry B, Mansy HA, Sandler RH, Royston TJ, Modeling and Experimental Validation of Sound Transmission in Human Torso, BMES, (Sep. 25-28, 2013, Seattle, WA)

3. Peng Y, Dai Z, Royston TJ, Mansy HA, Sandler RH, Chest Response to Vibratory Excitation: Advances Beyond Percussion, ASME IMECE, (Nov. 9-15, 2012, Houston, TX).

4. Peng Y, Dai Z, Mansy HA, Royston TJ, Poroviscoelastic Modeling of Mechanical Wave Motion in the Lungs, ASME SBC, (Jun. 20-23, 2012, Fajardo, Puerto Rico).

5. Dai Z, Peng Y, Mansy HA, Royston TJ, Sound Transmission in a Lung Phantom Model, ASME IMECE (Nov. 15-21, 2013, San Diego, CA).

6. Dai Z, Peng Y, Mansy HA, Royston TJ, Sandler RH, Estimation of Local Viscoelasticity of Lungs Based on Surface Waves, ASME IMECE (Nov. 11-17, 2011, Denver, CO).

7. Dai Z, Peng Y, Royston TJ, Array Measurement and Imaging of Sound Transmission through the Lungs, 159th Meeting of the Acoustical Society of America (Apr. 19-23, 2010, Baltimore, MD).

8. Henry B, Dai Z, Peng Y, Mansy HA, Sandler RH, Royston TJ, Investigation of Pulmonary Acoustic Simulation: Comparing Airway Model Generation Techniques, SPIE Medical Imaging, (Feb. 15-20, 2014, San Diego, CA).

9. Royston TJ, Dai Z, Peng Y, Mansy HA, Fractional Poroviscoelastic Modeling of Sound and Vibration in the Lungs, 4th International Conference on Porous Media & Annual Meeting of the International Society for Porous Media, (May 14-16, 2012, West Lafayette, IN).